

Droplets in annular-dispersed gas-liquid pipe-flows

Droplets in annular-dispersed gas-liquid pipe-flows

PROEFSCHRIFT

ter verkrijging van de graad van doctor
aan de Technische Universiteit Delft,
op gezag van de Rector Magnificus prof. dr. ir. J. T. Fokkema,
voorzitter van het College voor Promoties,
in het openbaar te verdedigen op
maandag 14 januari 2008 om 15:00 uur

door

Jozef Marinus Cyril VAN 'T WESTENDE

natuurkundig ingenieur
geboren te Fijnaart en Heijningen

Dit proefschrift is goedgekeurd door de promotoren:

Prof. dr. R.V.A. Oliemans

Prof. dr. R.F. Mudde

Samenstelling promotiecommissie:

Rector Magnificus	voorzitter
Prof. dr. R.V.A. Oliemans,	Technische Universiteit Delft, promotor
Prof. dr. R.F. Mudde,	Technische Universiteit Delft, promotor
Prof. dr. ir. G. Ooms,	Technische Universiteit Delft
Prof. dr. ir. J.D. Jansen,	Technische Universiteit Delft
Prof. B.J. Azzopardi,	University of Nottingham
Prof. M. Sommerfeld,	Martin-Luthre-University Halle-Wittenberg
Dr. L.M. Portela,	Technische Universiteit Delft
Prof. dr. ir. C.R. Kleijn,	Technische Universiteit Delft, reservelid

This project was supported by the Dutch Foundation for Technological Research (STW)

Cover design by J.M.C. van 't Westende & S.M. van 't Westende.

Printed by:

Ponsen & Looijen B.V.

Nudepark 142

6702 DX Wageningen

<http://www.p-l.nl>

ISBN 978-90-6464-208-1

Keywords: Phase Doppler Anemometry, Large Eddy Simulation, air-water.

© 2007 Jozef Marinus Cyril VAN 'T WESTENDE.

All rights reserved. No part of the material protected by this copyright notice may be reproduced or utilized in any form or by any means, electronic or mechanical, including photocopying, recording, or by any information storage and retrieval system without written permission from the publisher.

Voor Sandra

Contents

Summary	9
Samenvatting	11
1 Introduction	13
1.1 Liquid loading	13
1.2 Literature review	17
1.2.1 Experimental - measurements of E and α_{dr}	18
1.2.2 Experimental - measurements of R_{at} and R_{dep}	18
1.2.3 Experimental - measurements of d_{dr} and u_{dr}	19
1.2.4 Numerical - gas phase	21
1.2.5 Numerical - dispersed phase	22
1.3 Scope and outline	23
2 Droplets in annular pipe flow	25
2.1 Introduction	25
2.2 Phenomena in annular dispersed flows	27
2.2.1 Cocurrent to churn-annular flow	27
2.2.2 Onset of liquid loading, Turner criterion	28
2.2.3 Dispersed-phase pressure-gradient	29
2.3 Flow loop	30
2.4 Post-processing of the PDA-data	32
2.5 Measurement results	33
2.5.1 Gas-phase velocity-profiles	35
2.5.2 Drop size distributions	39
2.5.3 Droplet velocity	42
2.5.4 Residence time	47
2.5.5 Dispersed-phase pressure-gradient	48
2.5.6 Flow reversal	50
2.6 Conclusion	51

3	Pressure gradient and deposition of a dispersed phase	53
3.1	Introduction	53
3.2	Simulations	54
3.2.1	Quasi-1D approach	55
3.2.2	3D simulation	58
3.3	Results	63
3.3.1	Quasi-1D approach	63
3.3.2	3D simulation	66
3.4	Conclusion	80
4	Effect of the dispersed phase on the secondary flow	83
4.1	Introduction	83
4.2	Problem formulation	84
4.3	Simulations	85
4.4	Results	88
4.4.1	Mean gas-phase velocity	89
4.4.2	Particle concentration	92
4.4.3	Driving force of the secondary flow	95
4.4.4	Deposition	98
4.5	Conclusion	102
5	The effect of secondary flow on a particle distribution	103
5.1	Introduction	103
5.2	Problem formulation	105
5.3	Simulations	106
5.4	Results	109
5.4.1	Secondary flow	109
5.4.2	Particle-laden flow	111
5.5	Conclusion	123
6	Conclusions and recommendations	125
6.1	Conclusions	125
6.2	Recommendations	127
A	Wall functions	129
B	Injection PDF	133
	Bibliography	135
	Acknowledgement	143
	List of publications	145
	About the author	147

Summary

Annular-dispersed gas-liquid pipe-flows are commonly encountered in many industrial applications, and have already been studied for many decades. However, due to the great complexity of this type of flow, there are still many phenomena that are poorly understood. The aim of this thesis is to shed more light on some of these processes involving the dispersed-phase of an annular-dispersed flow.

One specific topic we investigated is the occurrence of flooding, and the role of the dispersed-phase in this. The flooding phenomenon is related to the liquid-loading phenomenon that is of crucial importance in the exploitation of most gas-wells.

Our approach has been to perform both experimental and computational studies, using some experimental results as an input for the simulations.

With the experimental work the dispersed-phase in the core of an annular-dispersed air-water flow is studied using Phase Doppler Anemometry (PDA): the pipe has a diameter of 5 cm, and a length of about 240 pipe diameters. In a vertical-upward flow the influence of the droplets on the flow reversal phenomenon, which marks the onset to churn-annular flow, is investigated. It is shown that the dispersed-phase is not directly causing the flow reversal, since all detected droplets move cocurrent with the gas-flow. However, by affecting the film thickness distribution, it can influence it indirectly.

The measurements also show that the gravity is negligible with respect to the strong axial acceleration of the individual droplets, making the inclination of the pipe to the horizontal irrelevant with respect to this.

The statistics of the PDA-measurements have been used as an input for our simulations, mimicking the atomisation process of an actual annular-dispersed flow as realistically as possible. The computations are performed with a finite-volume in-house LES-code. Wall-functions are implemented to allow for rough walls, and to make high Reynolds-number computations feasible. The dispersed-phase is treated using point-particles that are individually tracked. Both mono- and poly-dispersions are used in the computations.

The acceleration of a dispersed-phase in a high-velocity gas-flow seems to either act as added wall-roughness, increasing locally the turbulence intensity, or slow-down the mean gas-flow, decreasing locally the turbulence intensity. It is shown that particles in a small intermediate size-range have the largest overall acceleration, and hence are most effective in increasing the total pressure-gradient; this is also observed with the experimental results. The overall acceleration of a particle can be understood by considering the relevant time-scales involved:

the particle relaxation-time, the particle residence-time, and the time-scale of the large-scale turbulence.

In an actual horizontal annular-dispersed pipe-flow, in general, the liquid film at the bottom of the pipe is thicker, and thus the gas-liquid interface will most likely show a circumferential variation in waviness, i.e. a variation of the roughness. Also, the dispersed-phase concentration will be largest in the bottom region of the pipe due to the gravitational settling. Both the variation of wall-roughness and the non-homogeneous distribution of the dispersed-phase are shown to generate a secondary flow: a mean flow in the cross-section of the pipe, usually manifested as multiple counter-rotating cells. This secondary flow is shown to affect the circumferential variation of the deposition of the dispersed-phase, and may increase the concentration of the dispersed-phase in the core of the flow.

Samenvatting

Annulair gedispergeerde gas-vloeistof pijpstromingen komen veelvuldig voor in industriële toepassingen, en zijn gedurende tientallen jaren reeds bestudeerd. Vanwege de grote complexiteit van deze type stroming, zijn er desalnietemin nog veel fenomenen die nauwelijks begrepen zijn. Het doel van deze dissertatie is om een aantal van de processen die betrekking hebben op de gedispergeerde fase van een annulair gedispergeerde stroming beter te belichten. Een specifiek onderwerp dat we hebben onderzocht is het ontstaan van 'flooding', en de rol die de gedispergeerde fase hierin speelt. Het fenomeen 'flooding' is gerelateerd aan het 'liquid-loading' fenomeen, dat van een cruciaal belang is bij de exploitatie van de meeste gas putten. Onze aanpak is geweest om zowel een experimentele als een numerieke studie te verrichten, waarbij enkele experimentele resultaten op hun beurt gebruikt zijn als invoer voor de numerieke berekeningen.

In de experimentele studie is de gedispergeerde fase in de kern van een annulair gedispergeerde lucht-water stroming bestudeerd met behulp van Phase Doppler Anemometry (PDA): de binnen diameter van de pijp is 5 cm, en heeft een lengte van ongeveer 240 buisdiameters. Bij een verticale opwaartse stroming hebben we de invloed van de druppels op het 'flow reversal' fenomeen bestudeerd, dat op de grens naar een churn annulair stroming ligt. We tonen aan dat de gedispergeerde fase de 'flow reversal' niet direct veroorzaakt, aangezien alle gedetecteerde druppels in de richting van de gas-stroming bewegen. Desalnietemin kunnen ze indirect een bijdrage leveren, door de dikte van de vloeistof film te beïnvloeden.

De metingen laten ook zien dat de zwaartekracht verwaarloosbaar is ten opzichte van de sterke axiale versnelling van de individuele druppels, zodat de hellingshoek van de pijp met de horizontaal hier geen invloed op heeft.

De statistieken van de metingen met de PDA zijn gebruikt als invoer voor de numerieke berekeningen om zo het verstuiwingsproces van een annulair gedispergeerde stroming zo realistisch mogelijk na te bootsen. De berekeningen zijn uitgevoerd met een eigen 'finite-volume' LES-code. Wandfuncties zijn geïmplementeerd om wandruwheid toe te staan, en om berekeningen met een hoog Reynolds-getal mogelijk te maken. De druppels zijn als puntdeeltjes beschouwd, en zijn individueel gevolgd. Zowel mono-dispersies als poly-dispersies zijn toegepast in de berekeningen.

De versnelling van een gedispergeerde fase in een snelle gasstroom lijkt zich enerzijds te gedragen als een additionele wandruwheid, die lokaal de turbulentie intensiteit verhoogt. Anderzijds vertraagt de dispersie de gemiddelde gassnelheid, waarbij lokaal de turbulentie intensiteit

verlaagd wordt. We laten zien dat zowel de kleinste deeltjes als de grootste deeltjes niet de grootste gemiddelde versnelling hebben, en als gevolg hiervan het minst effectief zijn in het vergroten van de totale druk gradient. Dit is ook zichtbaar bij de experimentele resultaten. De gemiddelde versnelling van een deeltje kan inzichtelijk gemaakt worden door de relevante tijdschalen te beschouwen: de relaxatie tijd van de verblijftijd van het deeltje, en de tijdschaal van de grootschalige turbulente structuren.

Over het algemeen, is bij een horizontale annulair gedispergeerde buisstroming de vloeistof film aan de onderkant van de buis dikker. Waarschijnlijk daarom, zal het gas-vloeistof oppervlak een variatie in de golven langs de omtrek van de buis vertonen, ofwel een variatie in de ruwheid. Ook de concentratie van de dispersie zal het grootst zijn in de onderste helft van de buis als gevolg van het uitzakken van de druppels door de zwaartekracht. We laten zien dat zowel de variatie in de ruwheid langs de omtrek van de buis als de niet-homogene verdeling van de dispersie een secundaire stroming veroorzaken. Tijdsgemiddeld beschouwd, is een secundaire stroming een stroming in de dwarsdoorsnede van de buis die zich meestal manifesteert als meerdere tegendraaiende cellen. Deze secundaire stroming beïnvloedt de variatie in de depositie van de druppels langs de omtrek van de buis, en kan de concentratie van de dispersie in de kern van stroming vergroten.

1. Introduction

1.1 Liquid loading

An annular-dispersed gas-liquid pipe-flow is a specific flow-phenomenon in the wide field of multiphase flow, that deals with the hydrodynamics of two or more immiscible phases of matter (gas, liquid or solid). Multiphase flows are significant in numerous situations, and occur in nature, and as a result of human interference in nature, i.e. technical applications and their consequences. Examples of multiphase phenomena in nature are, e.g., rain, sand storms, sediment transport in rivers and oceans, and submarine volcanoes. Fuel injection in engines, the bubbles in champagne, the transport and treatment of sewage, and the chemical and physical deposition during micro-chip fabrication, are some illustrations of multiphase phenomena by human involvement.

Gas-liquid pipe-flows are commonly used in industrial applications, e.g., in the exploitation of oil and gas-wells, in evaporators, and in heat exchangers. For given properties of the gas and liquid phase, and that of the pipe, a gas-liquid pipe-flow organises itself into a specific flow-pattern, depending on the orientation of the pipe, and the flow-rates of both the gas and the liquid phase. A flow pattern is the geometric distribution of the two phases in the pipe. Starting with a low upward gas flow-rate in a vertical pipe, and increasing the gas flow-rate gradually, while keeping constant the liquid flow-rate, we encounter the following flow-patterns, see fig. 1.1:

- bubbly flow: gas-bubbles of approximately uniform size move upwards through the continuous liquid phase, driven by buoyancy.
- slug flow: the gas flows mainly as large Taylor-bubbles upward through the continuous liquid phase. Small gas-bubbles are also entrained in the liquid between two Taylor-bubbles.
- churn flow: highly unstable flow of an oscillatory nature, whereby the liquid near the pipe wall continually pulses up and down.
- annular-dispersed flow: the liquid phase flows partly as a thin wavy film along the pipe wall, and partly as droplets in the turbulent gas-core.

For a horizontal pipe, the gravity breaks the axi-symmetry: in general, due to gravitational settling, the heavier phase is more likely to be found in the bottom region of the pipe. For a low gas flow-rate the flow-pattern depends on the liquid flow-rate: starting with a low liquid flow-rate, and increasing the liquid flow-rate gradually, while keeping constant the gas

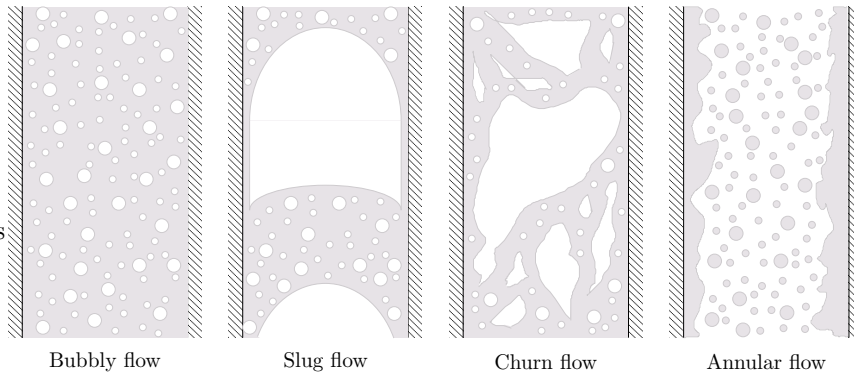


Figure 1.1: Flow patterns for a vertical upward gas-liquid flow.

flow-rate, we observe the following flow-patterns: stratified flow, slug flow, and bubbly flow, see fig. 1.2. For large gas flow rates, the flow pattern is again an annular dispersed flow. With stratified flow, the liquid film is not continuous along the pipe circumference: i.e. the top of the pipe is not covered with a continuous liquid film. As a result of the gravitational settling, for stratified flow and annular dispersed flow, the droplet concentration, and the film thickness is largest in the bottom region of the pipe.

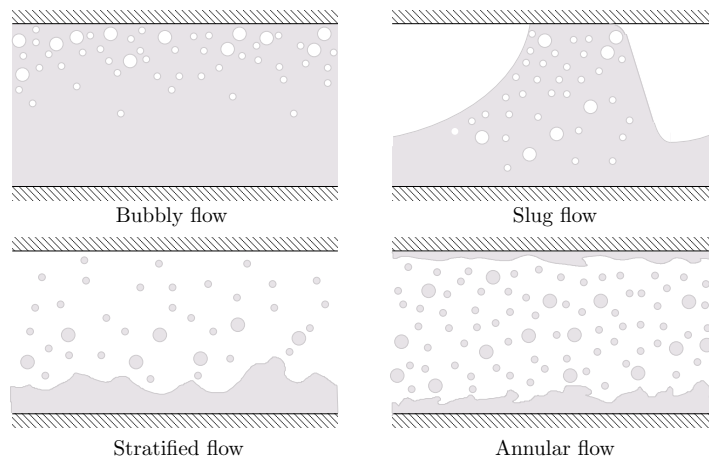


Figure 1.2: Flow patterns for a horizontal gas-liquid flow.

In literature some more flow-patterns are identified, that better describe some specific features of the flow, e.g., stratified smooth flow v.s. stratified wavy flow in a horizontal pipe. In fig. 1.3 we show the flow-pattern map for a vertical upward and a horizontal air-water pipe-flow, with varying gas and liquid flow-rates.

In this thesis we focus on gas-liquid pipe-flows with a large gas flow-rate and a small liquid flow-rate: the field of operation of the gas and liquid superficial velocities is presented by the

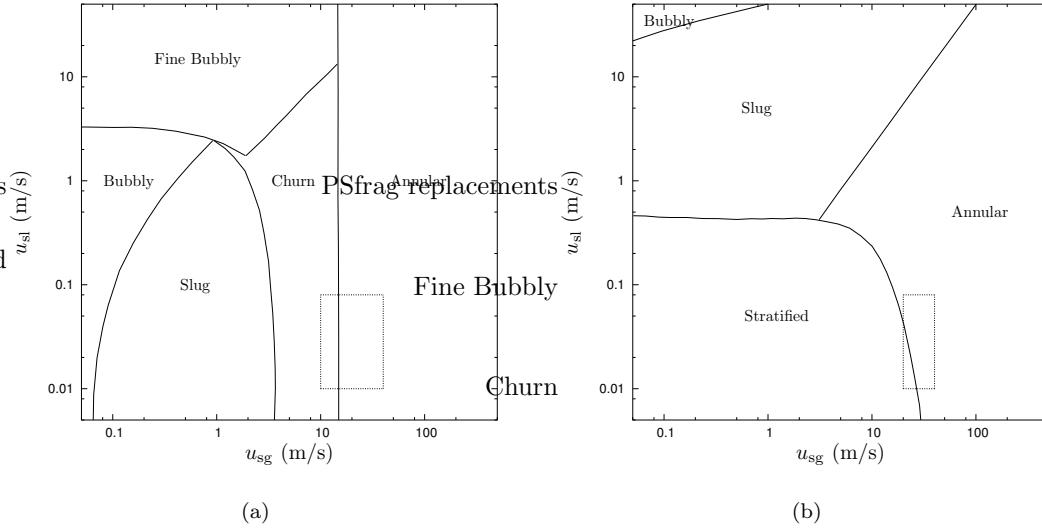


Figure 1.3: Flow pattern map for an air-water pipe flow with a diameter, $D = 0.05$ m, at atmospheric conditions, and ambient temperature, $T_{\text{amb}} = 25$ °C. a) Vertical upward flow, taken from Taitel et al. (1980), and b) horizontal flow, taken from Taitel (1977). The flow-rates we have investigated in this thesis are all situated in the dotted box shown in both graphs.

dotted box in fig. 1.3. Hence the flow-regimes we encounter are annular-dispersed flow, churn flow, and stratified flow. Especially, we are interested in the phenomenon of flooding that occurs at the transition of annular-dispersed flow to churn flow: the gas flow-rate is no longer able to drag the liquid completely upward, and part of the liquid phase drains downward, countercurrent with the gas flow.

This flooding is a key issue in the exploitation of older ‘wet’ gas-wells, producing simultaneously gas and liquid (condensate, oil, and water). For these gas-wells the down-flow of liquid may not be drained sufficiently fast into the reservoir, and liquid accumulates downhole. This can block the inflow of gas from the reservoir into the production tubing, and ceasing the production of gas: a phenomenon referred to as liquid-loading. Its origin is ascribed in the literature to the film-flow or the dispersed droplet-flow:

- In the gas producing industry, the onset of liquid loading is commonly predicted using a correlation developed by Turner et al. (1969). The idea behind this correlation is to estimate the minimum gas velocity that can keep the largest droplet, present in the gas core, pending. When the gas velocity in the production tubing gets below this minimum velocity, liquid loading will occur. It is, thus, implicitly assumed that the dispersed phase is causing liquid loading, although direct evidence for this is not available.
- Zabaras et al. (1986) identified a switching behaviour of the wall-shear near flooding conditions, i.e. the wall-shear is alternately directed upward and downward. Following their idea the onset of liquid loading is coupled to the instability of the liquid film.

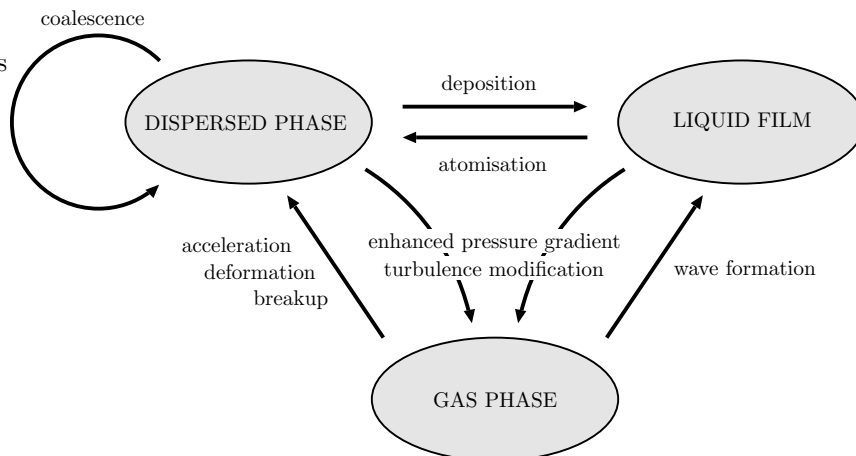


Figure 1.4: Some of the most important, and general accepted interactions between the different phases: gas phase, dispersed phase and liquid film.

The explanations of Turner et al. and Zabaras et al., given above, point to either the dispersed phase (droplets) or the liquid film as the cause for liquid loading. However, the complete picture is more complex, since there exists much interaction between them, and with the gas phase. In fig. 1.4, we show some of the most important, and generally accepted interactions between the gas phase, the dispersed phase and the liquid film, which are described below in some detail:

Atomisation: under the action of the gas flow, droplets are created from the liquid film. Two major atomisation mechanisms have been proposed: bag breakup and ligament breakup. With bag breakup, occurring at lower gas and liquid flow rates, the liquid film is undercut by the gas flow, forming an open ended bubble with a thick filament rim. Both the bubble and the rim break up in droplets. At higher flow rates ligament breakup becomes important: the crests of roll-waves are elongated, and thin ligaments are torn from the film, breaking up in droplets, see, e.g. Azzopardi (1997), and Marmottant and Villermaux (2004). Depositing droplets impinging onto the liquid film can also cause atomisation.

Deposition: droplets hit the wall usually at a different location than where they were atomised, and form a liquid film or merge with it, see e.g. Russell and Lamb (1974). The deposition behaviour of the droplets depends, amongst others, on the level of turbulence intensity, the orientation of the pipe axis with respect to the gravity, and the droplet relaxation-time, see, e.g., Friedlander and Johnstone (1957), Cousins and Hewitt (1968), Fore and Dukler (1995a), Young and Leeming (1997), and Pan and Hanratty (2002).

Deformation and breakup: when the slip velocity of a droplet is sufficiently large, depending on the droplet size, it may deform, or even breakup. Colliding droplets may also breakup into smaller ones, and the interaction with the gas-phase turbulence can also affect breakup, see, e.g., Hinze (1955), and Kocamustafaogullari et al. (1994).

Coalescence: when two droplets hit each other they may merge, forming a single larger droplet. Thoroddsen and Takehara (2000) showed that coalescence is a very fast cascade process, which also seems to play a role in the breakup of ligaments into droplets (atomisation), see Marmottant and Villermaux (2004).

Acceleration: droplets are created with an initially low axial velocity, roughly equal to the wave-velocity, and are strongly accelerated due to drag in the high-velocity gas-stream, see, e.g., Lopes and Dukler (1986)

Enhanced pressure-gradient and turbulence modification: for an annular flow the waves on the liquid film act as wall-roughness, hence it results in a larger value of the pressure-gradient, see, e.g., Darling and McManus (1968). Also the acceleration of the droplets, causes a transfer of momentum from the gas-phase to the dispersed-phase, and thus contributes to the pressure-gradient as well, see, e.g., Lopes and Dukler (1986); an increased pressure-gradient leads to an increased production of turbulent kinetic energy. More details on the modulation of the turbulence by the dispersed phase is given by, e.g., Gore and Crowe (1989), Hetsroni (1989), Elghobashi and Truesdell (1993), Azzopardi (1999), Crowe (2000). Note that the turbulence itself also affects the droplet dispersion, and therefore also the deposition, see, e.g., Csanady (1963), Truesdell and Elghobashi (1994), and Mols (1999).

Wave formation: ripple waves and disturbance waves are travelling on top of a base liquid film. The high gas-shear results in the transition of periodic waves to disturbance waves, which may be rather asymmetric, occur irregularly and carry a significant amount of liquid, see, e.g. Peng et al. (1991), and Belt et al. (2007).

Furthermore, for a horizontal and inclined pipe-flow the gravity causes drainage of the liquid film and settling of the droplets to the bottom of the pipe, i.e. in the bottom region of the pipe the liquid film thickness and the droplet concentration is larger than in the top region of the pipe. As a consequence, the Reynolds-stresses are no longer axi-symmetric distributed, leading to the creation of a secondary flow: a mean flow in the cross-section of the pipe, usually manifested as multiple counter-rotating cells, see, e.g., Darling and McManus (1968). Speziale (1982), Belt et al. (2005), and chapters 2, 4 and 5 of this thesis. Both the gravity and the secondary flow affect the distribution of the liquid film along the pipe wall, and of the droplets in the core of the flow. Therefore it also plays a role in the liquid-loading behaviour of a gas-liquid pipe-flow.

In this thesis we will look more closely to the processes and interactions in which the dispersed phase is involved, related to the liquid loading issue. An accompanying thesis of Belt (2007) focusses more on the interactions with the liquid film.

1.2 Literature review

There has been done a lot of research to the properties of the dispersed-phase in an annular flow, both experimental and numerical. With experimental work the amount of entrainment, E , the dispersed-phase holdup, α_{dr} , the rate of atomisation, R_{at} , the rate of deposition, R_{dep} , the droplet diameter, d_{dr} , and the droplet velocity, u_{dr} , have been measured in order to characterise the dispersed phase; Azzopardi (1997) gives a good overview of the various experimental techniques used.

The numerical studies that are most important for annular flows, are divided here into those focussing on the gas phase, and those focussing on the dispersed phase, although a very strict division can not be made. The ‘gas-phase’ studies comprise turbulence research of single-phase flows, and turbulence modulation by the dispersed-phase. The ‘dispersed-phase’ studies concentrate on, amongst others, the spatial distribution and the deposition behaviour of the dispersed phase. Note that in the numerical studies of droplet-laden turbulent gas-flows, in general, the droplets are represented by particles of given mass and momentum. A nice overview of the limitations of computer simulations concerning single phase flow is given in Jimenez (2003), and that of industrial turbulent dispersed multiphase flows in Portela and Oliemans (2006).

1.2.1 Experimental - measurements of E and α_{dr}

The amount of entrainment is defined as the ratio of the dispersed phase mass flux over the total liquid mass-flux. The dispersed-phase holdup is defined as the dispersed-phase volume-concentration. They are closely related with each other, see, e.g., Schadel et al. (1990)

$$E \approx \alpha_{\text{dr}} S u_{\text{sg}} / u_{\text{sl}} \quad (1.1)$$

where u_{sl} and u_{sg} are the superficial liquid and gas velocities, respectively, and S is the average slip ratio between the droplet velocity and the gas velocity. The slip ratio is needed to couple flux related properties with those based on a fixed volume (e.g., the amount of entrainment with the holdup).

By extracting the liquid film, the mass flux of the film flow can be determined, and thus also indirectly the amount of entrainment. The liquid film can be extracted by using a slit (see, e.g., Hay et al. (1996)), or a porous wall (see, e.g., Lopez de Bertodano et al. (2001)). The dispersed-phase mass-flux can also be measured directly, e.g., using an iso-kinetic probe, see, e.g., Williams et al. (1996), or by using Phase Doppler Anemometry (PDA), see, e.g., Zhang and Ziada (2000) and Albrecht et al. (2003). With PDA the diameter of individual droplets that cross a detection volume is measured, see section 1.2.3, and thus their volume flux can be calculated. However, due to PDA restrictions, reliable mass flux estimates are rather difficult to obtain.

The largest difficulty with which all techniques are dealing is the handling of the interface, i.e. how to discriminate the flux originating from the waves with the flux originating from the dispersed phase.

1.2.2 Experimental - measurements of R_{at} and R_{dep}

The rate of atomisation is defined as the mass of liquid droplets, created from the liquid film per unit of time per unit of area. The rate of deposition is defined as the mass of liquid droplets that deposit onto the liquid interface (or onto the wall) per unit of time per unit of area. They are related to the amount of entrainment via, see, e.g., Pan and Hanratty (2002):

$$\rho_l u_{\text{sl}} \frac{dE}{dz} = \frac{4}{D} (R_{\text{at}} - R_{\text{dep}}) \quad (1.2)$$

Usually the rate of atomisation is estimated indirectly via the rate of deposition, and the amount of entrainment using eq. 1.2. Ueda (1979), and Wilkes et al. (1983) measured R_{dep} in

a developing flow, and Fore and Dukler (1995a) measured R_{dep} in a fully developed situation, i.e. $d/dz = 0$.

The rate of deposition can be determined via uni-directional experiments, in which re-entrainment is prevented, see Azzopardi (1997); this can be achieved by extracting the liquid film, see section 1.2.1. The rate of atomisation can then be estimated by measuring the decrease in droplet mass flux with distance, or the increase in the film mass flux with distance. The latter method was employed by Fore and Dukler (1995a) and Lopez de Bertodano et al. (2001), using a double extraction technique.

The tracer technique allows to determine the rate of deposition, without having to remove the whole liquid film. Quandt (1965) and Schadel et al. (1990) injected a tracer into the film, and measured the tracer concentration at different distances from the injection point. From the diminution of the tracer concentration with increasing distance the rate of deposition can be deduced.

Another completely different approach was taken by Azzopardi and Whalley (1980) and Gibbons et al. (1985): they artificially created a single disturbance wave, and measured the entrained liquid flow rate, when the wave is almost at the measuring station. This flow rate can be converted to the rate of atomisation if the appropriate area is employed.

1.2.3 Experimental - measurements of d_{dr} and u_{dr}

In Azzopardi (1979), Hewitt and Whalley (1980), Tayali and Bates (1990) and Azzopardi (1997) a good overview of experimental techniques used for estimating drop sizes is given. Some techniques also provide an estimate for the droplet velocity, and some may be used for concentration measurements. Azzopardi (1979) divided the techniques into the following categories: (i) photography, (ii) impact method, and (iii) optical methods. They also show some thermal and electrical methods, but these are hardly applied anymore, hence we will not discuss them here.

Photography: one of the first methods employed to measure the size of individual droplets from an instantaneous snapshot of the dispersed phase. The extraction of drop sizes from the images is tedious, and prone to errors. The necessary illumination for a high quality image increases with decreasing drop-size, and with increasing droplet velocity. Photography perpendicularly to the flow direction allows for side and back illumination, but the liquid film needs to be stripped off, see, e.g., Cousins and Hewitt (1968), Pogson et al. (1970), and Hay et al. (1998). With axial photography images can be made with the liquid film still intact, but only side illumination is possible, see, e.g., Whalley et al. (1977), Hewitt and Whalley (1980) and Fore et al. (2002). Using a double exposure technique, an estimate of the droplet velocity can also be made.

Impact method: a sample of droplets is captured onto a sampling surface, possibly coated with a thin viscous liquid-film, by exposing it to the droplet stream, see, e.g., Ueda (1979), Okada et al. (1995), and Hurlburt and Hanratty (2002). An image of the sampling surface is then examined similarly as with photography. At impact of a droplet with the surface the droplets may deform or shatter, making the determination of the original drop size difficult. Small droplets may by-pass the sampling surface by following the gas flow around it. In order to prevent coalescence of droplets at the sampling surface, a short exposure time is needed.

Optical methods: the intensity of scattered light from a droplet moving through a laser beam depends on its size, its refractive index, the illuminating radiation, the wavelength, the polarisation of the light and the angle of detection. In general, the absolute value of the intensity is an unreliable parameter for estimating the drop size, and other techniques have been developed: a diffraction technique, a time-of-residence technique, and a phase doppler technique. For all techniques special care should be taken to obtain optical access to the droplet laden gas-core, e.g., by stripping off the liquid film or by penetrating the liquid film with hollow tubes or solid cylinders.

Diffraction technique: One of the most used methods is the diffraction technique, along the ideas of Swithenbank et al. (1976). Light scattered at small forward angles is dominated by diffraction, and its angular variation is captured by a set of annular detectors. The obtained energy distribution is then compared with an energy distribution, calculated from an assumed size-distribution. By adjusting the parameters describing the size-distribution a best fit between the measured and the calculated energy-distribution is achieved, see, e.g., Azzopardi et al. (1978), Gibbons et al. (1983), Jepson et al. (1989), Ribeiro et al. (1995), Simmons and Hanratty (2001), and Al-Sarkhi and Hanratty (2002).

Time-of-residence technique: A droplet passing through a laser beam, temporarily reduces the transmitted light. When also the velocity of the droplet is known, the chord of the droplet can be deduced from the time-signal of the transmitted light, i.e. the residence time of the droplet in the laser beam. With the chord-distribution the drop-size distribution can be obtained. Using two parallel beams, each with its own detector, Ritter et al. (1974) and Oki et al. (1975) determined the droplet velocity by correlating the time-signals from the two detectors. Alternatively, a fringe pattern in space can be created: alternating regions of high and low light intensity; a droplet passing these fringes will scatter light with alternating intensity of which the frequency depends on the droplet velocity and the fringe spacing. Semiat and Dukler (1981), Lopes and Dukler (1986), and Fore and Dukler (1995b) used a Ronchi diffraction grating to create such a fringe pattern in the cross-section of a single laser beam. Wigley (1977), and Tayali et al. (1990) employed two crossing laser beams, resulting in a fringe pattern, localized in a confined ellipsoidal measurement-volume, i.e. a laser doppler technique.

Phase doppler technique: similar to the laser doppler technique, a fringe pattern in space is created by two crossing laser beams. The scattered light is collected by two detectors placed at different angular positions. With the time signal from a single detector an estimate of the droplet velocity is made, and by cross-correlating the time signals from two detectors the droplet diameter is obtained, see, e.g., Durst and Zare (1975), Teixeira et al. (1988), and Albrecht et al. (2003). Using three detectors, the sizing range of the phase doppler can be extended significantly, and a measure of the sphericity is available.

A few studies have compared several measurement techniques: Zaidi et al. (1998) performed experiments using diffraction and PDA, and Simmons et al. (2000) used diffraction, PDA, and photography.

1.2.4 Numerical - gas phase

The spatial and temporal development of the gas-phase is calculated by solving simultaneously the Navier-Stokes equation and the continuity equation; for incompressible flows they are:

$$\nabla \cdot \vec{u}_g = 0 \quad (1.3)$$

$$\frac{\partial \vec{u}_g}{\partial t} + (\vec{u}_g \cdot \nabla) \vec{u}_g = -\frac{1}{\rho_g} \nabla p + \nu_g \nabla^2 \vec{u}_g \quad (1.4)$$

where \vec{u}_g , ρ_g and ν_g are the gas-phase velocity vector, the gas-phase density and the gas-phase kinematic viscosity, respectively; p is the pressure. Note that many simulations reported in the literature are concerned with a continuous phase in general, and not a gas-phase in specific; however, for our purpose, here we will use gas-phase, when referring to the continuous phase.

The differential equations for the gas-phase, eqs. 1.3 and 1.4, are solved using Direct Numerical Simulations (DNS), Large-Eddy Simulations (LES), or Reynolds-Averaged Navier-Stokes simulations (RANS). With DNS no assumptions are made on the physics, and all scales of the flow are resolved, including the turbulent kinetic energy and dissipation spectral peaks. LES relies on the classical result that the inertial energy cascade is independent of the dissipation mechanism, and the spectral peak of the dissipation is usually modelled as an isotropic stress-tensor, assuming that this does not disturb the large scales. In contrast, RANS only solves the mean flow, and closure-relations like, e.g., the $k - \epsilon$ model, are needed to estimate the Reynolds stresses; it does not provide knowledge on the physics of turbulence, since it uses the results of turbulence theory, see Jimenez (2003).

An extra difficulty for DNS emerges when simulating wall-bounded flows: the integral scale of turbulence, which has to be solved, decreases when approaching the wall. Also, increasing the Reynolds number decreases the integral scale. Since the eddies remain anisotropic as long as their size is larger than some fraction of the integral scale, they also have to be resolved in a LES. As a consequence the grid requirements are quite severe, and only flows with a rather low Reynolds number can be computed.

Furthermore, the modulation of the gas-phase turbulence by the presence of a dispersed-phase is an extreme complex phenomenon. Gore and Crowe (1989), Hetsroni (1989), and Elghobashi (1994) all present a different classification map to determine whether the dispersed-phase attenuates or augmentates the gas-phase turbulence. Ideally, the detailed flow around each individual particle is to be resolved. However, this makes simulating particle-laden flows as those found in industrial situations at present uncomputable, since they involve a very large amount of particles at very large Reynolds numbers. Instead, the total amount of particles used in the simulation may be reduced, e.g., Pan and Banerjee (1997) performed a ‘DNS’ of several particles in a channel flow, and Burton and Eaton (2005) performed a fully resolved DNS of a single particle in a homogeneous isotropic turbulent flow. A more applied method to calculate realistic particle-laden flows, is to relax the requirement of the resolution of the flow around the particles. Usually the particles are treated as point-particles, and their interaction with the gas-phase is performed via some force coupling scheme, see, e.g., Squires and Eaton (1990), Elghobashi and Truesdell (1993), Li et al. (2001), Rani et al. (2004), Portela and Oliemans (2003), and Mito and Hanratty (2006).

1.2.5 Numerical - dispersed phase

In order to calculate the spatial and temporal development of the dispersed-phase, we need to know the interactions between the gas-phase and the particles, and between the particles themselves. With respect to this, models are used which depend strongly on the type and number of particles in the flow. In case of very dilute flows, the influence of the particles on the gas phase and the inter-particle interactions can be neglected: one-way coupling. Increasing the particle concentration, at some point the turbulence modification by the particles needs to be taken into account as well: two-way coupling, see also section 1.2.4. For even larger concentration the inter-particle interactions also become important: four-way coupling. Inter-particle interactions can involve collisions, and modifications of the gas-particle interactions by surrounding particles.

In the simulations of particle-laden flows two approaches can be followed: (i) Eulerian-Eulerian, also known as two-fluid, and (ii) Eulerian-Lagrangian, also known as particle tracking. In the two-fluid approach the particle-phase is treated as a continuous phase by averaging its properties over a computational cell. This approach requires the most levels of modelling, and therefore is least used in scientific research of particle-laden gas flows. Because of the low computational cost, however, this type of simulations are very valuable for the industry.

With particle tracking the gas phase is solved similarly to a single phase turbulent flow, whereas the individual particles are tracked, using a model for the force between the particle and the gas phase; if needed, models for inter-particle collisions and particle-wall collisions are also used. One major difficulty is the large number of particles needed, but this may be overcome by using ‘representative particles’ (e.g. point-particle approach, and parcel-tracking, see Huber and Sommerfeld (1998)), and ‘fictitious collisional particles’, see Sommerfeld (2001). Using RANS, the computational effort for solving the gas phase is minimum, however a model is needed for the complex interactions between the particles and the gas-phase turbulence. Usually, all particle-effects are assumed to be due to the ‘direct interaction’ of the particles with the surrounding fluid, and ‘indirect effects’ are not taken into account. However, Li et al. (2001), and Bijlard et al. (2002) show that small ‘direct interaction’ can lead to a large disruption in the turbulence dynamics. Another advantage of RANS is that wall-roughness can easily be implemented, see Sommerfeld (1992).

With Eulerian-Lagrangian DNS/LES, the level of modelling is kept to a minimum, and thus helps to improve the models that are used for Eulerian-Lagrangian RANS, and Eulerian-Eulerian RANS. Since it involves a very large computational effort to simulate a high Reynolds-number wall-bounded DNS/LES, and/or to track a great number of particles, most of the simulations found in the literature are one-way coupled systems with a low or moderate Reynolds-number.

Among the subjects that are studied are: (i) the preferential concentration of particles, e.g., Squires and Eaton (1991), and Rouson and Eaton (2001), (ii) the deposition of particles at the wall, e.g., McLaughlin (1989), and Marchioli et al. (2003), (iii) the effect of the various forces acting on the dispersed phase (e.g. gravity, drag, lift), see Uijttewaal and Oliemans (1996), and Marchioli et al. (2007), (iv) the effect of interparticle collisions, e.g., Sommerfeld (2001), and Yamamoto et al. (2001), and in case of Eulerian-Lagrangian LES (v) the effect of the subgrid turbulence on the dispersed phase, see Portela and Oliemans (2001).

Although many numerical studies have been done, most of them treat conditions that are rather different from an annular dispersed flow. In most simulations a channel geometry is

studied instead of a pipe geometry, the gas-phase Reynolds number is much smaller than that of an annular flow, and the gas-liquid interfacial roughness is not taken into account. Also, most studies treat only mono-dispersions, and start with an initial spatial distribution in the flow, i.e. the atomisation process is not explicitly described. Furthermore, gravity, and the two-way coupling are often neglected. One of the few studies that explicitly try to approach an annular flow is by Mito and Hanratty (2006).

1.3 Scope and outline

In this thesis we present the results of a study on the dynamics of the dispersed phase of an annular gas-liquid pipe flow; two extremes of the pipe inclination from the horizontal have been studied: a vertical upward flow and a horizontal flow. In our study we have employed both experiments and simulations (Euler-Lagrangian LES).

With the experimental work we have measured drop sizes and drop velocities in the core of the annular flow using PDA, see section 1.2.3. Also the pressure gradient, the amount of entrainment, and, in case of flooding conditions, the amount of down flow have been determined. In chapter 2 the setup is described, and the results of a vertical annular flow are given. In chapter 4 we present the results of a horizontal annular flow. The results of the PDA measurements, i.e. the measured drop size-distributions, have been used as input for some of our simulations which are given in chapters 3 and 4.

With the simulations we have tried to simulate an annular dispersed pipe flow as realistic as possible. We have used an in-house finite-volume LES-code (pipe geometry), in order to simulate the turbulent gas-core of an annular flow. Wall-functions have been implemented, allowing us to prescribe locally the wall-roughness, hence mimicking the rough wavy gas-liquid interface by a rough circular wall. By using wall-functions in combination with a LES-code, we do not resolve the near-wall large-scale turbulent structures, making the grid-requirements less severe. This permits us computing a high Reynolds number flow with moderate computational resources. In chapters 4 and 5 a horizontal annular flow is simulated in which a secondary flow is present; the secondary flow is induced by a variation of the wall-roughness along the pipe circumference, and in chapter 4 it is modified by the particle feedback forcing. Chapter 3 deals with a vertical upward flow. In fig. 1.5 we show schematically the connections between the chapters, and their topic.

Every single droplet is represented by a single particle, that is treated as a point-particle, and which is Lagrangian tracked during the simulation using non-linear drag and gravity only. In chapter 5 we have tracked particles (mono-dispersed) using one-way coupling; the particles are initially homogeneously distributed in the pipe volume. In chapters 3 and 4 we have continuously injected particles (poly-dispersed) from the wall into the turbulent gas-flow; once they hit the wall, they are no longer tracked. Two-way coupling is employed, and the feedback forcing of the particles onto the gas-phase is computed using a point-force method. Results of the concentration-profiles, deposition behaviour, and velocity of the particles are reported and discussed.

In chapter 5, we show how the deposition behaviour of the dispersed-phase in a horizontal turbulent pipe-flow is altered by a secondary flow, generated by a variation in wall-roughness. The results are compared with the model given by Pan and Hanratty (2002).

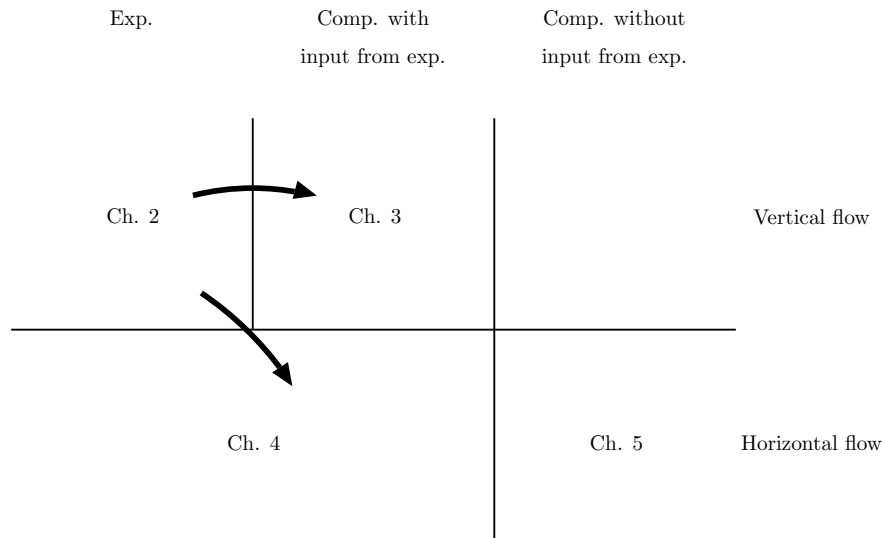


Figure 1.5: Schematic view of connection in between the chapters, and their topic (i.e. vertical or horizontal annular flow, experimental or computational work).

Chapter 3 aims to provide more understanding of the contribution to total pressure-gradient by the dispersed phase. It is shown that particles within a specific ‘intermediate’ size-range accelerate strongest. The results of the simulations are compared with the PDA measurements of a vertical annular-flow.

The modification of the secondary flow by the feedback forcing of the dispersed-phase with increasing mass-loading is studied in chapter 4. We show that the secondary-flow induced by a dispersed-phase is self-enforcing, and compare it with PDA measurements in a horizontal flow.

Conclusions and recommendations are given in chapter 6.

Some of the chapters have already been published in a journal, or are ready to be submitted. As a consequence some parts of the chapters, especially their introduction, may be a bit repetitive.

2. Droplets in annular pipe flow

Decreasing the gas flow-rate in an initially vertical upward annular dispersed pipe-flow, will eventually lead to a down-flow of liquid. The onset of this down-flow has been related in the literature to the presence of the dispersed phase and the instability of the liquid film. Here we investigate how the dispersed-phase may influence the down-flow, performing detailed PDA-measurements in a 5 cm vertical air-water annular-flow. It is shown that the dispersed-phase does not cause the liquid down-flow, but that it delays the onset of liquid down-flow. In cocurrent annular flow the dispersed phase seems to stabilise the film flow, whereas in churn-annular flow the opposite seems to be true.

This chapter has been accepted for publication in *Int. J. Multiphase Flow*, 33, 595-615, 2007.

2.1 Introduction

A plot of measured pressure losses for vertical annular gas/liquid flow from low to high gas velocities displays a minimum at a densimetric gas Froude number of 1 (Wallis (1969)). Operating conditions between the flooding point and the point of minimum pressure gradient are frequently indicated as churn or churn-annular flow. In the production of natural gas from underground gas wells, liquid (water, oil, condensate) is usually produced simultaneously. The flow pattern inside the production tubing is an annular dispersed two-phase flow: the liquid phase flows partly as a wavy film along the pipe circumference, and partly as entrained droplets in the turbulent gas core. At the end of the lifetime of gas wells, the gas production rate decreases strongly. Due to this decrease, the drag force of the gas phase exerted on the liquid phase might not be sufficient anymore to bring all the liquid to the surface, and liquid starts to drain downward (flow reversal). In such a situation, depending on the gas reservoir conditions (Oudemans (1989)), the liquid could accumulate downhole, block the inflow into the production tubing and gas production could cease. This phenomenon is called liquid loading, occurs at a gas rate below the minimum in the pressure gradient curve, and is closely related to flooding. Its origin is ascribed in the literature to the dispersed-phase or the film flow.

- In the gas producing industry, the onset of liquid loading is commonly predicted using a correlation developed by Turner et al. (1969). The idea behind this correlation is to estimate the minimum gas velocity that can keep the largest droplet, present in the gas core, pending. When the gas velocity in the production tubing gets below

Author	Measurement technique	u_{sg} (m/s)	u_{sl} (cm/s)	D (mm)	d_{32} (μm)
Azzopardi et al. (1991)	diffraction	30	4	20	104
Azzopardi and Teixeira (1994)	PDA	20	1.6	32	209
Fore and Dukler (1995b)	laser-grating	20	1.5	51	462
Hay et al. (1998)	Photography	30	1.4	42	138
Zaidi et al. (1998)	PDA	30	3	38	280
	diffraction	30	3	38	180
Simmons and Hanratty (2001)	diffraction	30	2.2	95	116
Al-Sarkhi and Hanratty (2002)	diffraction	30	4	25	103
Hurlburt and Hanratty (2002)	immersion	30	4	95	99
		20	7	95	145
Current study	PDA	12	4	50	255
		21	4	50	161

Table 2.1: Flow conditions and measurement techniques used in published studies on annular dispersed pipe flow (not an exhaustive list). We show here the superficial gas-velocity, u_{sg} , the superficial liquid-velocity, u_{sl} , the pipe diameter, D , and the measured Sauter-mean drop-diameter, d_{32} , reported in those studies.

this minimum velocity, liquid loading will occur. It is, thus, implicitly assumed that the dispersed phase is causing liquid loading, although direct evidence for this is not available.

- Zabarás et al. (1986) identified a switching behaviour of the wall-shear near flooding conditions (i.e. the wall-shear is alternately directed upwardly and down-wards). Following their idea the onset of liquid loading is coupled to the instability of the liquid film. This instability is influenced by the presence of the dispersed phase, decreasing both the film-thickness and the interfacial friction.

From the above it is clear that there is no consensus on the process of liquid loading, and to what extent the dispersion is responsible. To better understand the role of the dispersion in an annular flow close to liquid loading, we need to know the pdf of the drop-diameter, the pdf of the drop-velocity, the pressure-gradient and the amount of entrainment. Moreover, we want to know the spatial distribution of these dispersed-phase properties.

However, most of the data on the properties of the dispersed phase in an annular flow presented in the literature are obtained with methods that can only measure drop-size distributions, (e.g. photography, immersion method, or laser diffraction). Only a few show simultaneous measurements of drop-sizes and droplet-velocities, (e.g. Phase Doppler Anemometry (PDA), or a laser grating technique). Furthermore, the flow-conditions are mostly cocurrent annular flows, whereas, for our purpose, it is essential to have detailed information of drop-sizes, and droplet-velocities simultaneously near the transition from cocurrent to churn-annular flow, see table 2.1.

The objective of this paper is to provide detailed data on the characteristics of the dispersed phase in cocurrent annular flow and churn-annular pipe flow, with the aim to understand to what extent the droplets are contributing to the liquid down-flow transition in the churn-

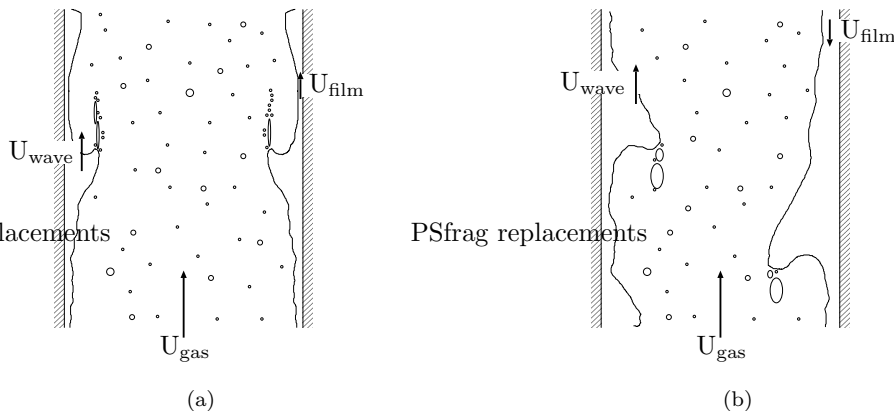


Figure 2.1: Schematic cross section of (a) a cocurrent annular flow and (b) a churn-annular dispersed flow. In churn-annular flow droplets are atomised from upward going flooding waves, the base liquid film drains downward. In cocurrent flow, droplets are formed from disturbance waves; the liquid film is less thick and uni-directional.

annular region. Experiments have been performed using PDA, providing us with both drop size and drop velocity measurements. Simultaneously, we have measured the total pressure-gradient, the amount of liquid down-flow and the amount of entrainment.

In section 2.2.1 we briefly discuss some of the general phenomena observed when the flow pattern changes from a cocurrent annular flow to a churn-annular flow. We show the model of Turner et al. (1969) in section 2.2.2, and the pressure gradient contribution of the dispersed phase in section 2.2.3. In section 2.3 we describe the flow loop, and in section 2.4 the post-processing of the PDA-data. The results of the measurements, both for the gas phase and the dispersed phase, are presented together with their discussion in section 2.5, and concluding remarks are given in section 2.6.

2.2 Phenomena in annular dispersed flows

2.2.1 Cocurrent to churn-annular flow

When a high-speed air-stream flows through a vertical pipe with diameter $D = 5$ cm, e.g. with a superficial gas velocity, $u_{sg} = 40$ m/s, and liquid is flowing simultaneously through the pipe with moderate speed, e.g. a superficial liquid velocity, $u_{sl} = 4$ cm/s, the flow pattern will be a cocurrent annular dispersed flow.

When we decrease the gas velocity, while keeping the liquid volume flux constant, the slip with the gas-liquid interface decreases, leading to a smaller interfacial shear, and hence the total pressure-gradient, ∇p_{tot} , decreases, fig. 2.3. The amount of entrained liquid also decreases as the gas rate declines. Due to the decrease in both interfacial shear and entrainment, the liquid film-thickness increases, and larger roll-waves are present, making the interface more rough (i.e. the interfacial friction factor becomes larger, Lopes and Dukler (1986)).

Upon further decrease of the gas velocity the pressure-gradient and the amount of entrainment reach a minimum. For the air-water system described above, this minimum occurs at $u_{sg} \approx 20$ m/s, corresponding with a densimetric Froude number, $Fr_g = \frac{u_{sg}^2}{gD} \frac{\rho_g}{\rho_l - \rho_g} \approx 1$, where g is the gravitational acceleration, and ρ_g and ρ_l are the density of the gas phase and the liquid phase, respectively.

When decreasing the gas velocity below $Fr_g = 1$, the liquid film thickness and the wave height become much larger. According to Zabaras et al. (1986) the wall-shear is occasionally directed upward, and film-churning occurs. The interfacial shear has to increase to balance the increasing weight of the liquid film, hence the pressure-gradient increases. Note that the amount of entrainment also increases again. A schematic of the flow structure for churn-annular and annular flow, respectively left and right of the pressure gradient minimum, is shown in fig. 2.1.

When in the churn-annular regime the gas velocity is further decreased less and less liquid is dragged up-wards: the smaller interfacial waves are tumbling cocurrently over the base film, which seems to drain downward. Occasionally, large interfacial waves (highly aerated) are propelled fast with the gas flow; possibly these waves correspond to the huge waves reported by Sekoguchi and Takeishi (1989). Here, the onset of liquid down-flow is referred to as the flow-reversal point, and, in general, occurs at a gas velocity below the minimum in the pressure-gradient curve.

Eventually, upon decreasing the gas flow-rate further below the flooding-point, all liquid flows counter-currently with the gas phase.

The gas velocities of the flow-reversal point and the flooding-point can be quite close together, especially for small liquid flow-rates. This indicates that rather subtle changes, can lead to dramatic differences in the flow.

2.2.2 Onset of liquid loading, Turner criterion

The most widely applied method for predicting the flow-reversal point is based on an analysis of droplet transport in a vertical turbulent gas flow by Turner et al. (1969). They related the onset of liquid loading, with the ability of the gas stream to keep the largest droplet pending. To estimate the size of the largest droplet present in the turbulent flow, $d_{dr,max}$, they used a correlation involving a critical Weber number. Droplets with a larger diameter are assumed to shatter due to the droplet-gas interactions.

$$We_{crit} = \frac{\rho_g u_{dr,t,max}^2 d_{dr,max}}{\sigma} = 30 \quad (2.1)$$

σ is here the surface tension and $u_{dr,t,max}$ represents the terminal free-fall velocity for the largest drop, and $u_{sg} = u_{dr,t,max}$ is the predicted flow-reversal point gas-velocity.

They assumed that the largest drop still is spherical, and that it has a drag coefficient, $C_D = 0.44$. This results in a correlation for $u_{dr,t,max}$:

$$u_{dr,t,max} = \left(\frac{90.9g\sigma(\rho_l - \rho_g)}{\rho_g^2} \right)^{0.25} \quad (2.2)$$

This gives for an air-water system a maximum droplet diameter $d_{dr,max} = 8.5$ mm, with a corresponding terminal free-fall velocity, $u_{dr,t,max} = 14.5$ m/s.

Although for an air-water flow in a 50 mm diameter vertical pipe, Turners correlation seems to give a good prediction of the flow-reversal point, it is not likely that drops with such a large diameter will be present. Maximum drop diameters, reported in the literature for air-water systems, are about 2000 μm , depending on flow rates, systems dimensions and measurement technique used, see e.g. Azzopardi and Hewitt (1997). The waves producing the droplets are in general much smaller than the estimate of the maximum drop diameter resulting from eq. 2.1 and eq. 2.2. So, in order to generate drops of the size needed for the Turner criterion coalescence has to be very strong. This is unlikely for the relatively dilute conditions at which gas wells operate.

2.2.3 Dispersed-phase pressure-gradient

When a droplet is created from the gas-liquid interface, its initial velocity is much smaller than the gas velocity. Due to the drag force exerted on the droplet, it will accelerate, increasing its kinetic energy. When the droplet impinges onto the gas-liquid interface, its kinetic energy is converted partly to kinetic energy of the liquid film (pushing the liquid film upward), but mostly to heat (via friction with the wall, according to Lopes and Dukler (1986) and Fore and Dukler (1995a)). The conversion of energy from kinetic to heat makes it no longer available for transporting the liquid phase upward cocurrently with the gas phase, and thus the acceleration of the dispersion can be interpreted as an energy loss, resulting in a dispersed-phase pressure-gradient: the dispersion effectively blocks the gas-flow.

For a constant total pressure-gradient the dispersed-phase pressure-gradient increases for an increasing amount of entrainment. The interfacial shear then has to decrease, which will make the liquid film more unstable. On the other hand, increasing the entrainment also decreases the film flow-rate: the liquid film becomes thinner, making it more stable. The balance of the stabilising and destabilising effects depends on the value of the dispersed-phase pressure-gradient for a given amount of entrainment.

The dispersed-phase pressure-gradient, ∇p_{dr} , can be estimated directly from the PDA measurements (as we will show below), or indirectly using a model derived by Lopes and Dukler (1986). The indirect method of Lopes and Dukler is a more coarse approach, using the end-result of the acceleration process, i.e. the increase in droplet-momentum; ∇p_{dr} is estimated using a mean droplet axial-velocity at the center of the pipe, and an average rate of atomisation.

Model of Lopes and Dukler

Following a momentum balance Lopes and Dukler obtain:

$$\nabla p_{\text{dr}} = \frac{4}{D - 2\delta_f} R_{\text{at}} (u_{z,\text{dep,dr}} - u_{z,\text{at,dr}}) + \alpha_{\text{dr}} \rho_l g \quad (2.3)$$

where δ_f is the film thickness, R_{at} is the rate of atomisation, and $u_{z,\text{dep,dr}}$ and $u_{z,\text{at,dr}}$ are the droplets axial-velocity just before deposition and just after atomisation, respectively. α_{dr} is the holdup of the dispersed phase, and g is the gravitational acceleration.

The rate of atomisation and the holdup are related via:

$$R_{\text{at}} = \frac{\alpha_{\text{dr}} \rho_l (D - 2\delta_f)}{4t_{\text{res,dr}}} \quad (2.4)$$

where $t_{\text{res,dr}}$ is a characteristic residence time of the droplets, and can be estimated with:

$$t_{\text{res,dr}} = D/u_{\text{lat,dr}} \quad (2.5)$$

where $u_{\text{lat,dr}}$ is a characteristic droplet lateral-velocity, i.e. the droplet velocity projected onto the cross-section of the pipe.

Fore and Dukler (1995a) determine R_{at} indirectly by measuring the rate of deposition, R_{dep} , with a double film-extraction technique, and assuming $R_{\text{at}} = R_{\text{dep}}$. $u_{z,\text{dep,dr}}$ is estimated with the arithmetic-mean centerline droplet-velocity, which they measured using a laser-grating technique, and $u_{z,\text{at,dr}}$ is assumed to be equal to the wave velocity.

2.3 Flow loop

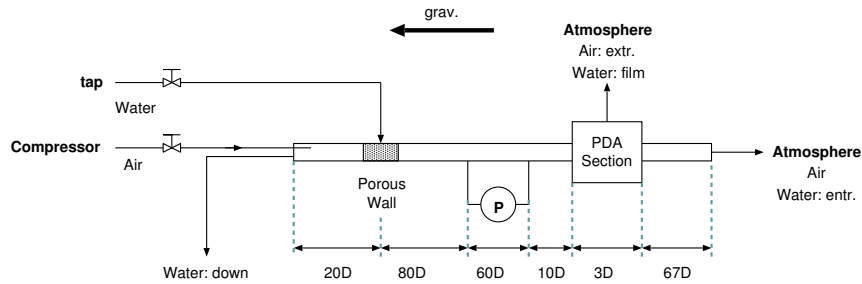


Figure 2.2: Flow loop.

The flow loop consists of a 50 mm acrylic pipe, placed vertical with a total length of 12 m, fig. 2.2. Dry air, supplied by a compressor is blown into the tube at near atmospheric conditions, and at 1 m downstream from the gas inlet a water film is created along the pipe circumference, using a porous wall. Both the air and water flow rates are controlled with rotameters with an accuracy of 2% for the gas flow and 4% for the liquid flow. The superficial air velocity ranges from 10 to 40 m/s, and the superficial water velocity is set at 1, 2, 4 or 8 cm/s.

Pressure drop measurements are performed between 80 and 140 pipe diameters from the liquid inlet using a water manometer with a read-out accuracy of about 10 Pa. For the churn-annular flow conditions, however, the strong pressure fluctuations deteriorate the accuracy down to about 450 Pa. Measuring the pressure gradient in this way, the difference between a single-phase turbulent gas flow and the Blasius curve is below 10%, for $5 \text{ m/s} < u_{\text{sg}} < 50 \text{ m/s}$, see fig. 2.3.

PDA measurements are performed at 7.5 m downstream from the liquid inlet (150 tube diameters). To obtain optical access, the liquid film is extracted in two steps: (i) the base film

	Resolution	Range	Reproducibility
Arrival time	4 μs	0 - ∞^\dagger s	
Transit time	0.4 μs	0 - 100 μs	
Axial velocity	0.06 m/s	-24 - 73 m/s	2 %
Lateral velocity	0.02 m/s	-8 - 24 m/s	2 %
Drop size	1.2 μm	0 - 780 μm	3 %

Table 2.2: Resolution, measuring range and reproducibility for the droplet properties/quantities measured by the PDA. † The measurement stops when the inter-arrival time of two subsequent droplets is larger than 30 s. By repeating a measurement 5 times at equal flow conditions, we have estimated the reproducibility using the standard deviation.

is removed using a porous wall, and *(ii)* the remaining waves are extracted using a slit. With the slit, the pipe diameter is reduced to 40 mm, and therefore only the droplet-laden gas-core flows through the PDA section; the distance between the slit and the measurement area of the PDA is 5 cm, and the total length of the film extraction section and the PDA section is 15 cm. To compensate for the reduced pipe cross-section, we also extract air at the film extraction section and measure its flux, which should be approximately 30% of the total air flux.

The PDA transmitting optics used is a Dantec 60X Fiber Flow transmitting optics system combined with a Dantec 60X41 transmitter. To measure two velocity components of the droplets we use a pair of green laser beams (514.5 nm, 15.5 mW) and a pair of blue laser beams (488 nm, 20.5 mW), provided by a Stabilite 2016 water cooled Ar-ion laser (Spectra-Physics). A frequency-shift of 40 MHz using a Bragg-cell is applied. The receiving optics consist of a Dantec 57X10 receiving optics fitted with four 57X08 photo-multipliers, allowing us to measure two velocity components and make two drop-size estimates. The signal of the photo-multipliers is past through a Dantec 58N10 signal processor, estimating for each droplet measured: the arrival time of the droplet, the transit time of the droplet, the axial-component and the lateral-component of the velocity of the droplet and the drop-size. A scattering angle of 70° with parallel polarisation is selected for the PDA-setup. The focus of the lens for both the transmitting and the receiving optics is 600 mm; beam separation at the transmitting optics is 38 mm.

Our PDA has been calibrated by measuring four different sized glass-microspheres with a narrow size-distribution (Whitehouse Scientific, general purpose microspheres: GP0049, GP0116, GP0275 and GP0550) using *(i)* PDA, *(ii)* laser diffraction (Mastersizer S particle size analyser, Malvern Instruments), and *(iii)* photography (PCO sensicam QE mounted on a Zeiss axiovert 200M optical microscope, approximately 1.6 pixel/ μm). All measurement techniques provide similar results with a variation between them of maximum 10%, see Kemp (2004). Table 2.2 summarises the resolution, range and reproducibility of the measured droplet properties/quantities for a cocurrent annular and churn-annular flow.

At the end of the pipe the liquid phase is collected and measured, and the air is released to the atmosphere; since the liquid film is already extracted stream upward, we can measure the entrainment via the collected water at the end-section. In case of a churn-annular flow, part of the liquid phase flows countercurrent with the gas phase, and is drained and measured at the air-inlet; this drain is closed for the gas-flow using a waterlock.

More details on the flow loop, can be found in Westende et al. (2005).

2.4 Post-processing of the PDA-data

For any property P_{dr} of the dispersed phase, its flux, $\Phi_{P_{\text{dr}}}$, and its concentration, $C_{P_{\text{dr}}}$, can be computed as a summation of the contributions of all individual droplets, see also Albrecht et al. (2003):

$$\Phi_{P_{\text{dr}}} = \sum \frac{P_{\text{dr}}}{A_{\text{det,dr}}T} \quad (2.6)$$

$$C_{P_{\text{dr}}} = \sum \frac{P_{\text{dr}}}{A_{\text{det,dr}}u_{z,\text{dr}}T} \quad (2.7)$$

where $A_{\text{det,dr}}$ is the detection-volume area of a droplet, $u_{z,\text{dr}}$ is the axial component of the droplet-velocity, and T is the total measurement time.

The size of the detection-volume area depends on the drop-size, the droplet direction of movement, and the optical parameters of the PDA. In Westende et al. (2005) it is shown how the detection volume can be computed from the measurements. Since annular flows are strongly uni-directional, we use the axial component of the droplet-velocity, $u_{z,\text{dr}}$, for estimating $C_{P_{\text{dr}}}$.

The droplet volume-flux measured by the PDA should match the entrainment-flux collected at the outlet of the pipe. In order to achieve this, we introduce a correction factor, F_{cor} , and correct all fluxes and concentrations with this factor.

The dispersed-phase holdup, and pressure-gradient can directly be computed from the PDA-measurements as

$$\alpha_{\text{dr}} = \sum \frac{\frac{\pi}{6}d_{\text{dr}}^3}{A_{\text{det,dr}}u_{z,\text{dr}}T} \quad (2.8)$$

$$\nabla p_{\text{dr}} = \sum \frac{F_{\text{D},z,\text{dr}}}{A_{\text{det,dr}}u_{z,\text{dr}}T} \quad (2.9)$$

where d_{dr} is the droplet diameter, and $F_{\text{D},z,\text{dr}} = C_{\text{D}} \frac{1}{2} \rho_{\text{g}} u_{z,\text{s,dr}}^2 \frac{\pi}{4} d_{\text{dr}}^2$ is the drag force acting on a single drop. C_{D} is the drag coefficient, and $u_{z,\text{s,dr}} = u_{z,\text{g}} - u_{z,\text{dr}}$, is the axial component of the droplet slip-velocity, with $u_{z,\text{g}}$ being the gas-phase axial-velocity

The Sauter-mean-diameter is calculated via:

$$d_{32} = \sum \frac{d_{\text{dr}}^3}{A_{\text{det,dr}}u_{z,\text{dr}}T} \bigg/ \sum \frac{d_{\text{dr}}^2}{A_{\text{det,dr}}u_{z,\text{dr}}T} \quad (2.10)$$

A droplet axial-velocity related to the droplet momentum is the mass-weighted droplet axial-velocity (i.e. it is the total momentum divided by the total mass of the dispersed phase):

$$\bar{u}_{z,\text{dr}} = \sum \frac{\rho_1 \frac{\pi}{6} d_{\text{dr}}^3 u_{z,\text{dr}}}{A_{\text{det,dr}}u_{z,\text{dr}}T} \bigg/ \sum \frac{\rho_1 \frac{\pi}{6} d_{\text{dr}}^3}{A_{\text{det,dr}}u_{z,\text{dr}}T} \quad (2.11)$$

Since the axial momentum-concentration (numerator of eq. 2.11) can also be viewed as the mass-flux, $\bar{u}_{z,\text{dr}}$ also links the droplet volume-flux and the droplet holdup.

From eq. 2.8 and eq. 2.9 for the dispersed-phase holdup and pressure-gradient, derived from the centerline PDA-data, we have calculated the residence-time using eq. 2.3 and eq. 2.4.

$$t_{\text{res}} = \bar{u}_{z,\text{dr}} \left(\frac{\nabla p_{\text{dr}}}{\rho_l \alpha_{\text{dr}}} - g \right)^{-1} \quad (2.12)$$

where we have neglected $u_{z,\text{at,dr}}$ in eq. 2.3, and assumed $u_{z,\text{dep,dr}} = \bar{u}_{z,\text{dr}}$ at $y = 0$.

2.5 Measurement results

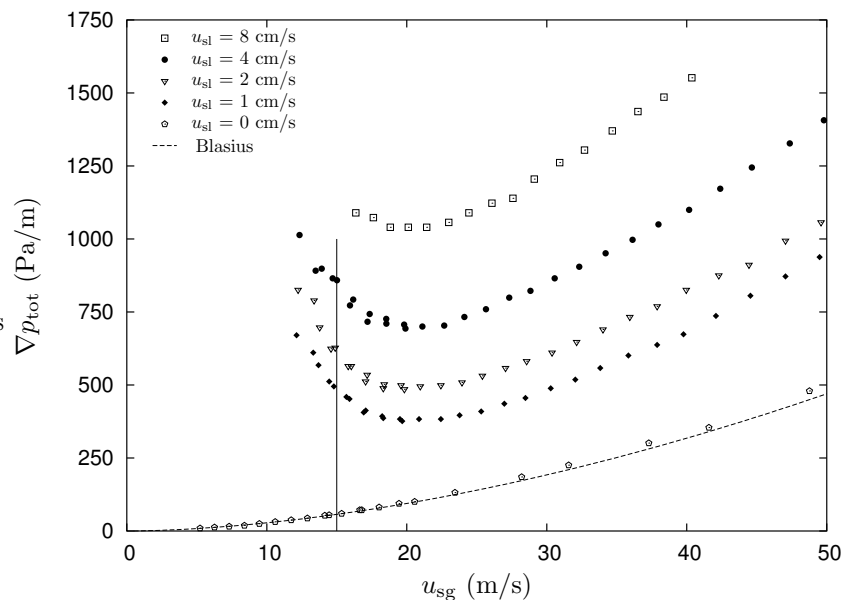


Figure 2.3: Total pressure-gradient in vertical annular flow. At $u_{\text{sg}} \approx 15$ m/s liquid starts to flow counter-current with the gas stream, liquid loading (solid line). We did not measure the pressure-gradient down to the flooding point. For comparison, single phase measurements are shown as well together with the pressure gradient prediction of Blasius.

In fig. 2.3 we show the total pressure-gradient for four different values of u_{sl} as a function of u_{sg} . The measurements of a single-phase gas-flow, and the corresponding prediction using Blasius correlation for the friction factor are plotted here as well. The vertical solid line represents roughly the gas-phase velocity at which flow-reversal starts. With the single-phase flow we observe a 5% overestimation of the Blasius correlation for $u_{\text{sg}} < 25$ m/s, and about 8% for larger gas flow-rates. For the two-phase flows we see that the pressure-gradient is much larger than the single phase, even with small liquid flow-rates. For all liquid flow-rates we observe a minimum in the pressure-gradient at about $u_{\text{sg}} = 20$ m/s, corresponding to $\text{Fr}_{\text{g}} = 1$, see also Zabarás et al. (1986).

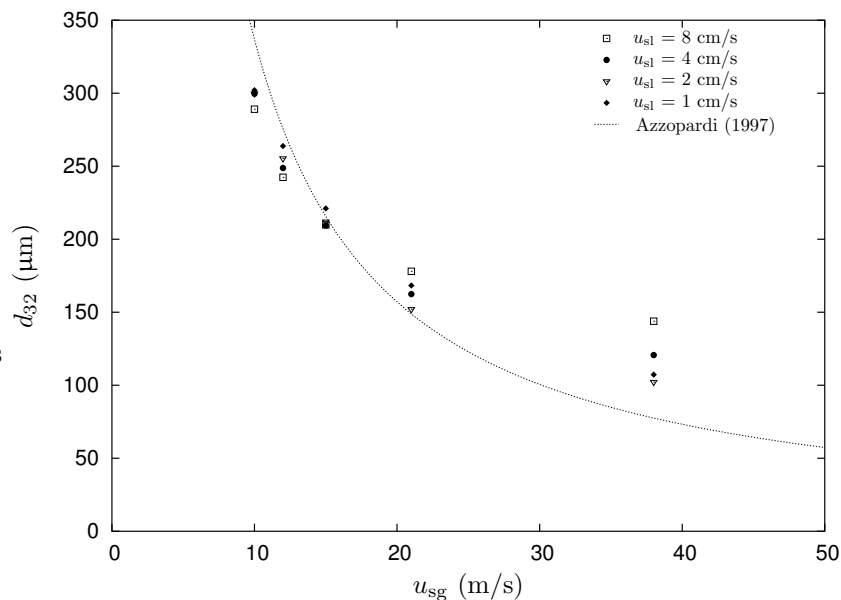


Figure 2.4: Measured Sauter-mean diameter in center of pipe. The solid line represents a correlation of the drop size that is found in Azzopardi (1997), ignoring coalescence.

In fig. 2.4 the measured Sauter-mean droplet-diameter is plotted, together with a correlation given by Azzopardi (1997):

$$\frac{d_{32}}{D} = 1.91 \text{Re}_{\text{sg}}^{0.1} \text{We}_{\text{sg}}^{-0.6} (\rho_{\text{g}}/\rho_{\text{l}})^{0.6} + 0.4E u_{\text{sl}}/u_{\text{sg}} \quad (2.13)$$

where $\text{Re}_{\text{sg}} = \rho_{\text{g}} u_{\text{sg}} D / \mu_{\text{g}}$ is the gas-phase Reynolds number, and $\text{We}_{\text{sg}} = \rho_{\text{g}} u_{\text{sg}}^2 D / \sigma$ is the gas-phase Weber number. μ_{g} is the gas-phase dynamic-viscosity. The second term in the RHS of eq. 2.13 is the contribution from drop coalescence.

For $u_{\text{sg}} > 20$ m/s the correlation underpredicts our measured values for d_{32} . We observe an increase of d_{32} with increasing u_{sl} , probably due to increasing coalescence. Here we note that including the coalescence term with $E = 1$ will result in an increase of d_{32} of about $20 \mu\text{m}$ for $u_{\text{sg}} = 40$ m/s and $u_{\text{sl}} = 8$ cm/s. It is interesting to observe that the correlation of Azzopardi (1997) approximates the drop size fairly well in the churn-annular regime, indicating that there may be similar atomisation mechanisms in both churn-annular and cocurrent annular flow. We see that increasing the liquid flow-rate slightly decreases d_{32} . For all gas flow-rates we see that the measurements with $u_{\text{sl}} = 1$ cm/s behave unexpectedly, i.e. they do not show the smallest value for d_{32} .

In order to study the transition of cocurrent to churn-annular flow, we show some flow-details in the following sections for two gas flow-rates: one just above the minimum in the pressure-gradient curve, $u_{\text{sg}} = 21$ m/s, and the other in between the flooding point and the flow-reversal point, $u_{\text{sg}} = 12$ m/s. In table 2.4 we show some characteristic flow parameters for the flow conditions we have measured. For comparison, also the results measured by Fore and Dukler

Time scale	
$\overline{\mathcal{T}}_{G21L1} = \mathcal{L}/u_{\nabla,G21L1}$	2.5 ms
$\overline{\mathcal{T}}_{G12L4} = \mathcal{L}/u_{\nabla,G12L4}$	1.5 ms
$\tau_{dr,10\mu m}$	0.3 ms
$\tau_{dr,20\mu m}$	1.2 ms
$\tau_{dr,50\mu m}$	7.7 ms
$\tau_{dr,200\mu m}$	124 ms

Table 2.3: Characteristic time-scales in annular flows. The time scale of the large-scale structure, \mathcal{T} , is estimated using the length scale, $\mathcal{L} \approx D/10$, and an effective friction-velocity, u_{∇} , see eq. 2.14.

(1995a,b) for $u_{sg} = 20$ m/s are given. We present here only the details for $u_{s1} = 1, 2$, or 4 cm/s, since these compare best with the results of Fore and Dukler. Most of the data in table 2.4 for the condition G21L2 compare favourably with the interpolated Fore and Dukler conditions FD1 and FD2. The drop size d_{32} is an exception: our measurement of $d_{32} = 157 \mu m$ is much smaller than the value of $485 \mu m$ from the interpolation. As already clear from the data in table 2.1 the laser grating technique used by Fore and Dukler seems to have had a bias to large drop sizes. Such a large drop size is also completely out of line with the literature correlation plotted in fig. 2.4.

For each flow condition, we measured at 19 locations in the cross-section of the pipe, in the range $-0.8R < y < 0.8R$, where y is the Cartesian measurement position and R is the pipe radius; on average 10^5 droplets were measured at each position.

In the following sections we present the results of the measured gas-phase velocity profiles (2.5.1), the drop size distributions (2.5.2), the drop velocity (2.5.3), the residence time of the droplets (2.5.4), and the dispersed phase pressure-gradient (2.5.5). In section 2.5.6 we discuss the consequences of the results for the flow-reversal phenomenon.

2.5.1 Gas-phase velocity-profiles

We have measured the gas-velocity using ‘tracer’-droplets: droplets in the size range: $10 \mu m < d_{dr} < 20 \mu m$. The relaxation-time, τ_{dr} , of the tracer-droplets is smaller than or of the same order of the time-scale of the large-scale turbulence structures, \mathcal{T} , see table 2.3. Therefore, the tracer-droplets are expected to follow the mean gas-velocity, and to provide an estimate of the gas-phase turbulence intensity. Droplets with a drop-size smaller than $10 \mu m$ are scarce (about 200 on a total droplet-population of 10^5), and they have a very small detection-volume (minimum detectable drop size: $d_{min} \approx 5 \mu m$), making velocity-estimation from those drops less accurate. Therefore, the droplets smaller than $10 \mu m$ are not used for estimating the gas-velocity. The drop-size range for the tracer-droplets extends to $20 \mu m$ in order to have enough tracer-droplets to estimate the gas-phase velocity (about 3000 tracer-droplets on a total droplet-population of 10^5). An additional advantage of using droplets as tracers is that they are already present in the flow.

Name	Current study						Fore and Dukler (1995a, b)		
	G12L1	G12L2	G12L4	G21L1	G21L2	G21L4	FD1	FD2	FD3
u_{sg}	12.1	12.1	12.2	21.3	21.4	21.2	20.2	20.2	20.1
u_{sl}	0.97	1.97	3.94	0.94	2.01	4.11	1.5	3	4.5
∇p_{tot}	670	825	1015	385	500	700	476	517	657
u_{∇}	2.6	2.9	3.3	2.0	2.3	2.7	2.2	2.3	2.6
E	0.58	0.46	0.40	0.11	0.32	0.43	0.23	0.30	0.32
$\Phi_{1,down}$	11	3	7	0	0	0			
F_{cor}	1.72	2.03	2.77	0.86	1.10	1.27			
δ_f	1015	1171	1358	335	428	565	454	499	584
d_{32}	265	261	255	172	157	161	462	533	668
$u_{z,dep,dr}$	12.3	13.0	13.5	22.9	24.1	24.7	22.7	23.2	23.5
$u_{z,at,dr}$	0.0	0.3	2.1	1.1	1.4	1.6	1.30	1.45	1.45
$u_{z,s,dr}$	5.3	5.6	5.7	7.3	5.7	4.5			
C	0.19	0.30	0.52	0.08	0.56	1.17			
α_{dr}	5.1	8.0	13.6	0.51	3.0	7.9	2.1	5.6	8.9
t_{res}	0.22	0.20	0.15	0.14	0.17	0.23			
R_{at}	28	49	105	4.6	21	41	12.4	23.5	25.6
$L_{z,dr}/D$	56	50	39	59	75	100			
∇p_{dr}	31	54	98	8	37	76	23	47	54

Table 2.4: Mean parameters measured in the churn-annular flows and the cocurrent annular flows. E is the amount of entrainment, $\Phi_{1,down}$ is the liquid down flow, C is the droplet concentration, and $L_{z,dr}$ is the axial distance covered by the droplets, and is computed as $L_{z,dr} = \bar{u}_{z,dr} t_{res,dr}$. For comparison we also show the measurements of Fore and Dukler (1995a), FD1-FD3. The film-thickness and the wave-velocity, i.e. $u_{z,at,dr}$, are measured with a similar technique as done by Fore and Dukler.

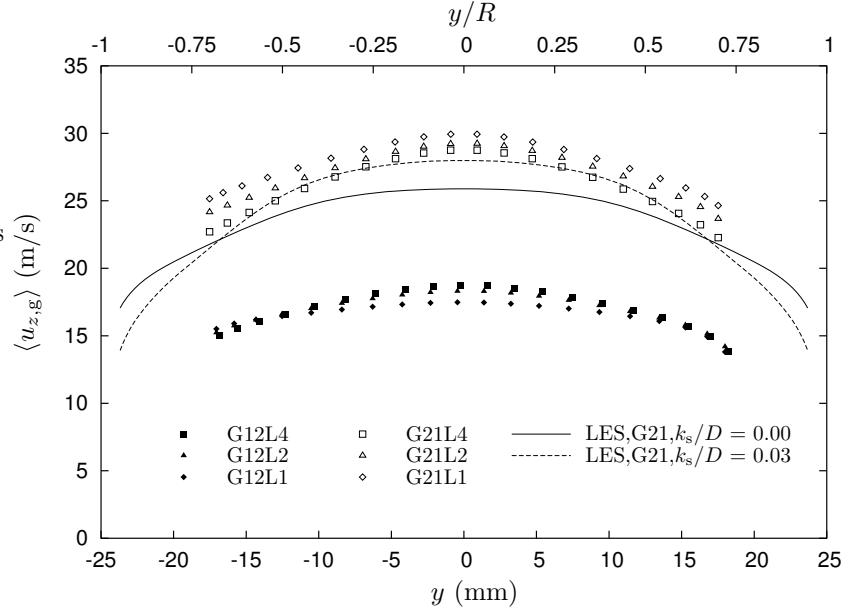


Figure 2.5: Profiles of the mean gas-phase velocity for G12L1 to G21L4, measured using ‘tracer-drops’. The results of a standard LES pipe-flow corresponding to $u_{sg} = 21$ m/s with a smooth wall (solid line), and with a uniform wall-roughness, $k_s/D = 0.03$, (dashed line) are shown.

The mean gas-velocity and the gas-velocity fluctuation are shown in fig. 2.5 and fig. 2.6, respectively. For a radial position $|y| > 0.7R$ the gas velocity decays rapidly to zero, which is an indication that, in this region, the flow is disturbed by the film extraction: a new boundary layer has developed. Therefore, we show only results for $|y| \leq 0.7R$. For comparison the profiles from a standard large eddy simulation (LES) single-phase pipe-flow are plotted as well: we show the LES-results of a pipe-flow for G21 with a smooth wall (solid line), and with a uniform wall-roughness, $k_s/D = 0.03$ (dashed line), see Westende et al. (2004). Using this hydraulic roughness results in a film thickness of $\delta_f \approx \frac{1}{4}k_s = 375 \mu\text{m}$ (Wallis (1969)), which is a reasonable estimate for the film-thickness for G21L1, see table 2.4.

Mean gas-phase velocity

In fig. 2.5 we observe that the mean-velocity profiles of G21 are more core-peaked than the LES with a smooth wall, they are roughly similar to the LES with the uniform wall-roughness. The core-peaking is slightly increasing with increasing u_{s1} . This supports the idea that increasing u_{s1} increases the effective roughness of the interface.

However, the value of the mean gas-velocity measured with the PDA is about 10% larger than the LES with the uniform roughness. Probably this mismatch is caused by the film extraction section: in order to compensate for reducing the pipe-diameter in this section, gas is extracted simultaneously with the liquid film. In case of, e.g., flow condition G21L1 about 17% of the total gas flow is extracted at the extraction section, see table 2.4, whereas about

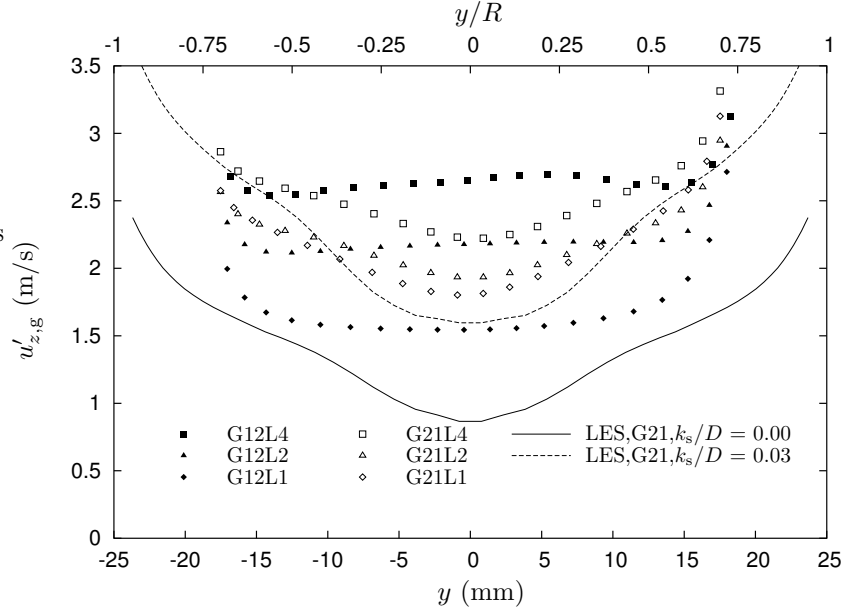


Figure 2.6: Profiles of the gas-phase velocity-fluctuation for G12L1 to G21L4, measured using ‘tracer-drops’. The result of a standard LES pipe-flow with a smooth wall (solid line) or with a uniform wall-roughness, $k_s/D = 0.03$ (dashed line) is shown, corresponding to $u_{sg} = 21$ m/s, Westende et al. (2004).

24% should have been extracted, based on the LES mean velocity-profile with the uniform wall-roughness. This results in a gas-velocity increase of $\left(1 - \frac{1-0.24}{1-0.17}\right) \cdot 100\% \approx 8\%$, which is close to the bulk-velocity deviation observed. The resulting acceleration of the gas-phase is probably strongest at larger radial positions, thus flattening the gas velocity-profile. Since, the time it takes for a droplet to cover the distance between the film extraction and the detection volume is about 2.5 ms (assuming $u_{z,dr} = 20$ m/s), only the tracer-droplets are affected by a possible distortion of the film-extraction ($\tau_{dr,20\mu m} < 2.5$ ms).

The mean-velocity profile for the churn-annular flows is about 35% lower than for the cocurrent annular flows. The quotient, $\langle u_{z,g,G21} \rangle / \langle u_{z,g,G12} \rangle$ is constant in the cross-section of the pipe.

Gas-phase velocity fluctuation

The measured axial-velocity fluctuation of the gas-phase in the cocurrent flow conditions is similar to the LES with uniform roughness: it shows a minimum in the center region, although not as low as in the LES. Compared to the LES the turbulence-intensity seems to be enhanced in the center of the flow, possibly by the dispersed phase. The magnitude of the velocity-fluctuation of the measurements are in reasonable agreement with the LES with uniform roughness. Increasing u_{sl} increases the velocity fluctuations.

The axial-velocity fluctuations in the churn-annular flow show a different behaviour: the fluc-

tuations are nearly constant in the cross-section of the pipe, and are slightly core-peaking for large u_{s1} . Moreover, the magnitude of the velocity fluctuations is of the same order as those for the cocurrent flow, whereas the bulk-velocity of the churn-annular flows is approximately half the value of the cocurrent flows. Also, the magnitude of the velocity fluctuations depends much stronger on u_{s1} , than in the case of a cocurrent annular flow.

For both the churn-annular flow and the cocurrent annular flow the gas-phase velocity fluctuation scale approximately with the friction velocity, u_{∇} , just like in single-phase pipe-flows, see also table 2.4. Here we estimate the effective friction velocity via:

$$u_{\nabla} = \sqrt{\frac{D}{4\rho_g} \nabla p_{\text{tot}}} \quad (2.14)$$

Summarising, it seems that a cocurrent annular flow can be described as a single-phase turbulent pipe-flow with wall-roughness. With increasing u_{s1} the effect of the rough interface becomes stronger. Although we find a constant value for the ratio $\langle u_{z,g,G21} \rangle / \langle u_{z,g,G12} \rangle$, the gas-phase velocity fluctuations of the churn-annular flows behave differently than those of the cocurrent annular flows, and thus we can not describe a churn-annular flow as a single-phase turbulent pipe-flow. The cause of the different behaviour of the churn-annular flow is not yet understood by the authors, but lies probably in the different wave behaviour of the gas-liquid interface.

2.5.2 Drop size distributions

In fig. 2.7 we show the scaled drop-size distributions of the cocurrent annular flows G21L1 and G21L4, and of the churn-annular flow G12L4, at $y = 0$ (solid line; center) and at $y = -0.7R$ (symbols; closest to the receiver, and the smallest path-length of laser light through dispersion).

All distributions show an exponential tail at large drop sizes, and a ‘fall-off’ at small drop sizes, $d_{\text{dr}} \lesssim 35 \mu\text{m}$. In the literature a number of possibilities are proposed to predict the drop size distribution, although most of them lack a sound physical background, e.g. the Rosin-Rammler distribution or the upper-limit log-normal (ULLN) distribution, Mugele and Evans (1951). The ULLN gives in general a better fit to the distribution, Simmons and Hanratty (2001). With respect to this, an interesting study is done by Marmottant and Villermaux (2004), who performed experiments on the creation of droplets from a water jet by an air shear-flow. They state that the drop-size distribution is the result of a multiple breakup-coalescence process of the ligaments directly after their creation, resulting in a gamma-distribution, where the initial size of the ligaments determines the tail of the distribution.

An interesting feature of our measurements is that the drop size distribution seems to be the sum of two distributions, since there are two exponential tails. Especially for the cocurrent flows this effect is most clear (see, e.g., G21L1 for which the tails of the two exponential-distributions are indicated with dotted lines). Assuming that droplet breakup and coalescence are not dominant in the core of the flow (see below), this suggests that two independent atomisation processes are occurring simultaneously. Following the idea of Marmottant, a possible explanation is that two types of liquid lumps are created from the waves at the liquid film, each with its own characteristic size. When both lumps break up into droplets via

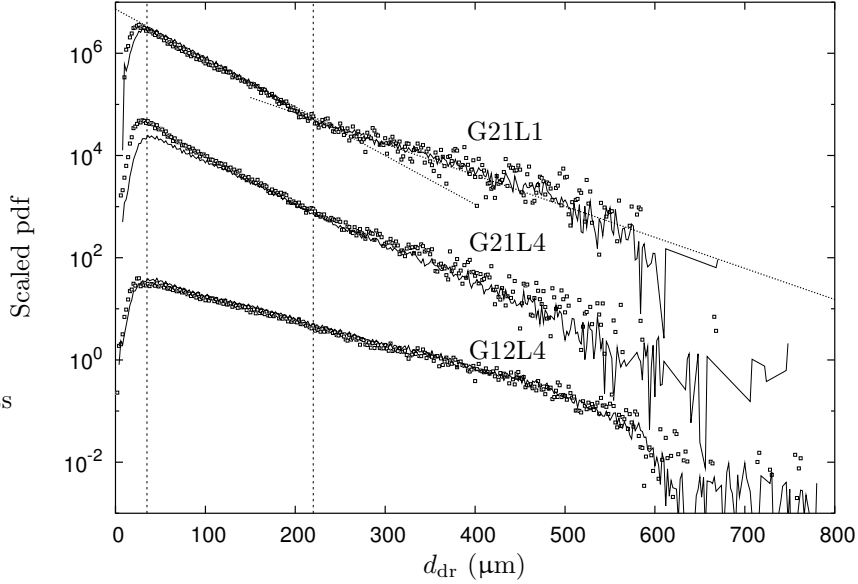


Figure 2.7: Drop-size distribution for flow conditions: G21L1, G21L4 and G12L4. The distributions are scaled to optimise the comparison of their shape between different flow conditions and spatial positions. The distributions are corrected for detection-volume dependency and velocity bias. The solid lines correspond to the measurements at $y = 0$, and the symbols to the measurements at $y = -0.7R$. The dashed lines show the approximate position below which the pdf falls to zero, $d_{\text{dr}} \approx 35 \mu\text{m}$, and the position of the deflection point of the distribution, $d_{\text{dr}} \approx 220 \mu\text{m}$. The dotted lines represent two exponential fits to the tails of the distribution of G21L1.

the same process, this results in two independent, but similar, distributions, both with their specific exponential tail. We can think of, e.g., bag breakup and ligament breakup providing the different liquid lumps.

For the cocurrent annular flows, we observe that, closer to the gas-liquid interface there are more smaller droplets present (compare, e.g., the solid line with the symbols for G21L4 in the region $d_{\text{dr}} < 50 \mu\text{m}$). Comparing the distribution of G21L1 with G21L4, we see that with decreasing u_{sl} this effect disappears. In the churn-annular flows this effect seems absent. Possibly, this is related to the turbophoresis effect, which tends to push the smaller droplets toward the interface. Since the turbophoresis effect scales with the gradient of the turbulence intensity, we speculate that turbophoresis is present in the cocurrent annular flows, increasing with increasing u_{sl} , and that it is absent in the churn-annular flows, see fig. 2.6. However, this can only explain the effects for $d_{\text{dr}} \lesssim 25 \mu\text{m}$, for which the relaxation time is of the same order of magnitude as the time-scale of the large-scale turbulence, see table 2.3.

Breakup and coalescence

For churn-annular flow we observe a cut-off for $d_{\text{dr}} \lesssim 600 \mu\text{m}$ at the pipe centerline, which might be caused by (i) the limited number of droplets in the sample, or (ii) the non-sphericity

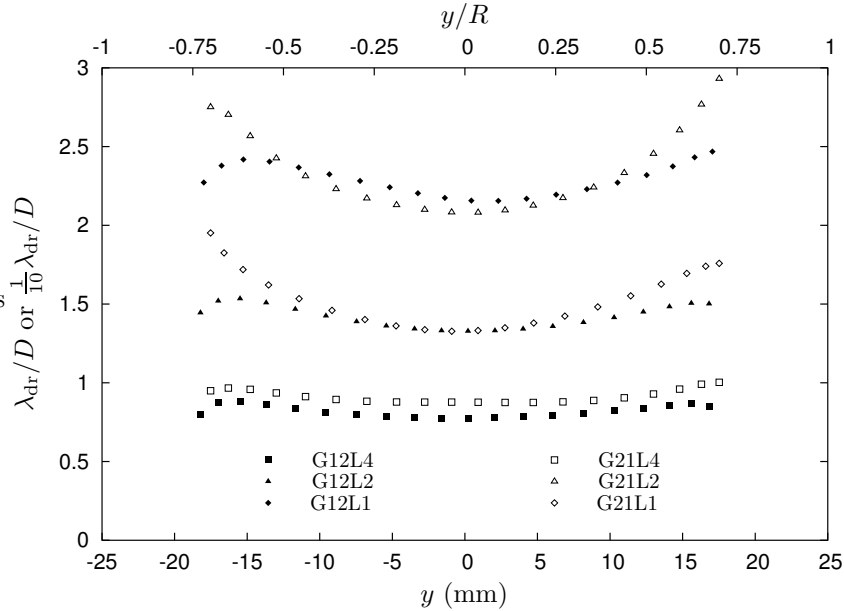


Figure 2.8: Droplet mean free-path-length normalised with the pipe diameter. For visualisation reasons we plotted $0.1\lambda_{\text{dr}}/D$ for G21L1.

of the larger drops. On average, only 0.1% of all droplets in churn-annular flow, is larger than $600\ \mu\text{m}$, making the drop-size distribution very noisy for $d_{\text{dr}} > 600\ \mu\text{m}$, and a possible cut-off difficult to determine. Since the PDA accepts only spherical droplets (sphericity validation is set to 10%), larger drops that are less difficult to deform have a smaller chance to be measured (e.g., Hay et al. (1998) measured a non-spherical droplet with $d_{\text{dr}} = 750\ \mu\text{m}$ using photography). Since we expect deformation of the droplets to occur earlier than breakup, and since we can not detect deformed droplets, it is likely that the cut-off is related to droplet deformation rather than to droplet breakup. Here we note that maximum drop-sizes reported in literature are about 1 mm and larger, which is well out of our measurement range.

Since the droplets are on average smaller in cocurrent annular flow than those in churn-annular flow, and since the turbulence intensity is of the same order, we expect droplet breakup in the core to be of even less importance for the cocurrent annular flows.

To determine whether coalescence is of any importance, in fig. 2.8 we plot the mean free-path-length of the droplets, λ_{dr} , given by:

$$\lambda_{\text{dr}} = \beta_{\lambda}/C_{A_{\text{dr}}} \quad (2.15)$$

where the constant β_{λ} depends on the details of the drop-size distribution, e.g. for an exponential distribution it can be easily shown that $\beta_{\lambda} = 3$.

From fig. 2.8 we observe that the free-path-length of the droplets is of the same order of magnitude as the pipe diameter, except for G21L1: $\lambda_{\text{dr,G21L1}} \approx 15D$. For $u_{\text{sl}} = 4\ \text{cm/s}$, the free-path-length is smaller than the pipe diameter, suggesting that coalescence only starts to influence the dispersion at this liquid flow-rate. As expected, increasing u_{sl} decreases λ_{dr} , due

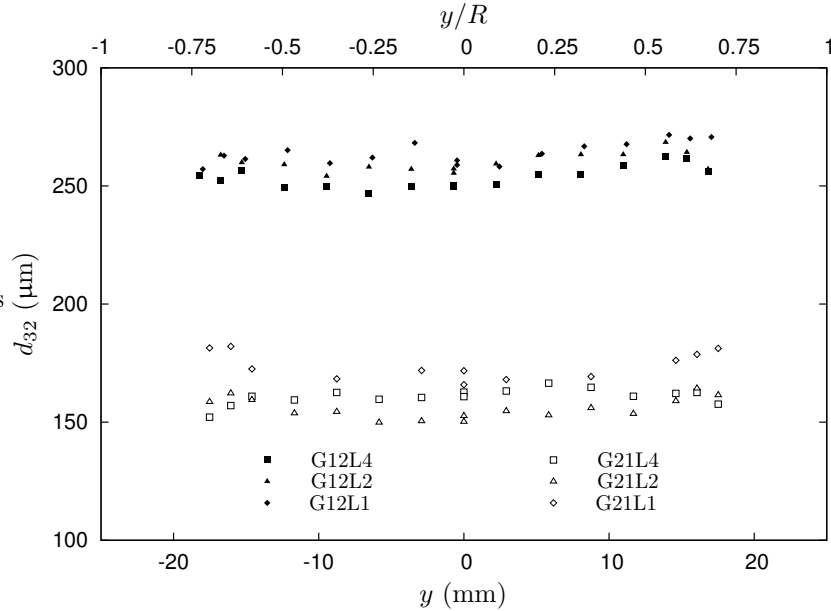


Figure 2.9: Sauter mean diameter in the pipe cross-section.

to the increase in droplet concentration; coalescence may become a more dominant process for $u_{sl} > 4$ cm/s.

From the above it seems that the presented distributions are not affected by breakup or coalescence in the core of the flow. The distribution at a specific location is then a result of the atomisation at the gas-liquid interface and the droplet dispersion. This is also supported by the fact that the tails of the drop size distribution are similar for $y \lesssim 0.4R$ (the droplets in the tails, $d_{dr} \gtrsim 100$ μm , all move ballistically). Note that when the drop size distribution is similar at different locations, then so is the mean drop size, see fig. 2.9.

2.5.3 Droplet velocity

In fig. 2.10 is shown the joint pdf of the droplet diameter and the droplet axial-velocity of G21L2 and G12L2, at $y = 0$ and at $y = -0.7R$, together with the mean axial-velocity of the droplets (solid lines). For G21L2, an estimate of the axial-velocity that a droplet has obtained when it reaches the centerline is plotted as well (dashed lines in the top left graph), with $t_{res} = 0.02$ s, 0.50 s and t_{∞} (terminal velocity); the line with $t_{res} = 0.02$ s and $t_{res} = 0.50$ s match approximately the border of the joint-pdf, suggesting 0.02 s $\lesssim t_{res} \lesssim 0.50$ s for G21L2. The joint pdf of the churn-annular flows and the cocurrent annular flows with different u_{sl} are similar, and therefore not shown here.

Since there exists a spread in the residence time of the droplets, see 2.5.4, and since the droplets are accelerating due to drag from an initially small axial-velocity (approximately the wave-velocity), we expect (i) a spread in the droplet axial-velocity, (ii) the droplet axial-

velocity to be skewed to high velocities, and (iii) lots of droplets to have a slip velocity much larger than the terminal free-fall velocity in a stagnant medium, see fig. 2.10.

Spread in axial-velocity

A measure for the spread in the droplet axial-velocity is the standard deviation, $u'_{z,\text{dr}}$, which is shown in fig. 2.11 for G21L2 and G12L2 in the center of the pipe. In this figure we observe a maximum of $u'_{z,\text{dr}}$ at $d_{\text{dr}} = 0$, and at $d_{\text{dr}} \approx 300 \mu\text{m}$ for G21L2; it is unclear why we do not observe a second maximum at larger drop-sizes for G12L2. A minimum is found for $d_{\text{dr}} \approx 20 \mu\text{m}$. From this we conclude that the spread in droplet axial-velocity, as caused by the spread in t_{res} , depends on the relaxation time of the droplets, and we expect this velocity spread to be maximum for $\tau_{\text{dr}} \approx t_{\text{res,dr}}$, with $t_{\text{res,dr}}$ a characteristic residence time for the droplets (most clear for G21L2).

Besides this, turbulence affects the smallest droplets ($d_{\text{dr}} \lesssim 25 \mu\text{m}$), and results in the increase of $u'_{z,\text{dr}}$ with decreasing d_{dr} in this drop-size range. Azzopardi and Teixeira (1994) also mention the importance of the spread in residence time of the drops to explain the drop-velocity fluctuation. They state that the spread in residence time is caused by the gas turbulence, accelerating and decelerating the smaller drops in the lateral direction. The smaller drops will then have a larger spread in life time, and, according to them, also a larger spread in axial velocities. However, their suggestion for the velocity spread can not explain the maximum in $u'_{z,\text{dr}}$ that is observed. Moreover, for the droplets that feel the gas-phase turbulence (accelerating and decelerating in the lateral direction), the velocity spread in the center of the pipe is most likely linked to the turbulence intensity itself.

The joint pdf at $y = 0.7R$ shows a much larger velocity spread than that in the center of the pipe, especially for G21L2. Since the pdf consists of droplets that are recently created and droplets that are about to deposit, the spread in residence time is expected to be larger, hence the spread in velocity is larger.

Skewed axial-velocity distribution

On average, the strength of the acceleration of the droplets decreases during their lifetime. Consequently, the droplet axial-velocity is skewed toward the larger velocities, i.e. it has a negative skewness. This is also observed in the droplet velocity pdf presented by Fore and Dukler (1995b) and Azzopardi (1999). However, here we note that they show the velocity pdf for the dispersion as a whole, which is more skewed due to the variation in drop sizes. For the flow conditions we have measured the skewness is roughly constant with increasing drop size, and has a value of about -0.2 for G12L2 and -0.8 for G21L2. Both Fore and Dukler (1995b) and Azzopardi (1999) also show the existence of droplets with a very large axial-velocity ($u_{z,\text{dr}} \approx 1.4 u_{\text{sg}}$), which is also the case in our flow conditions for $d_{\text{dr}} < 100 \mu\text{m}$. The size of these overshoots is about twice the gas-phase velocity-fluctuation as given in fig. 2.6, and is probably linked to the most energetic turbulent structures in the flow.

Large axial slip-velocity

From the top left graph of fig. 2.10, we see that most of the droplets have a slip velocity much larger than their terminal slip-velocity in a stagnant medium (solid line with $t_{\text{res}} = t_{\infty}$); they

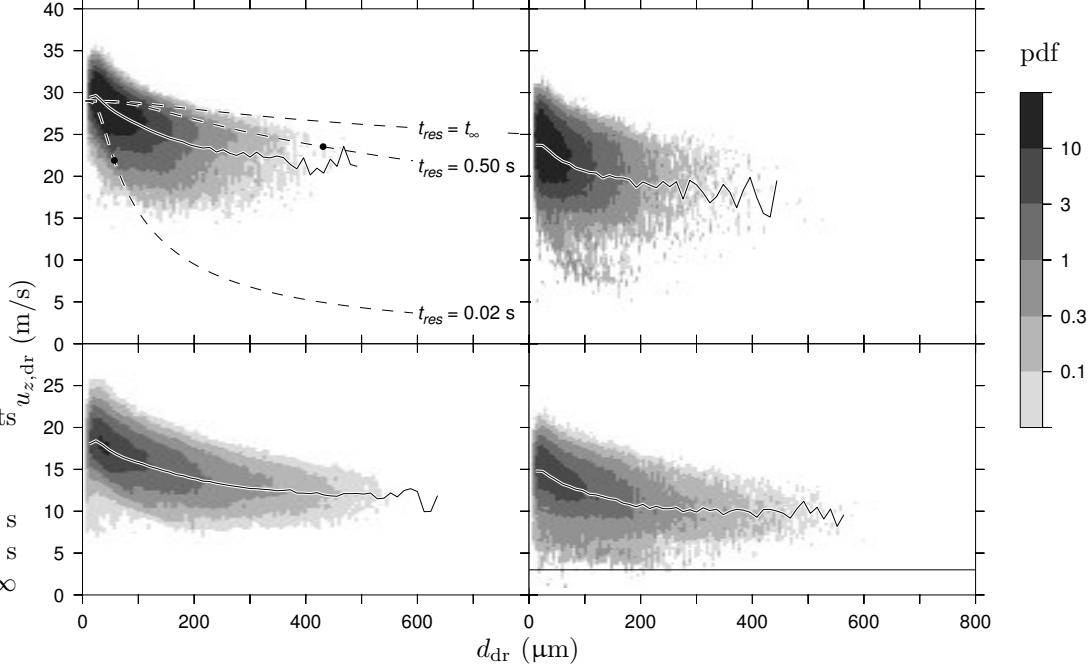


Figure 2.10: Scaled joint PDFs of drop size and axial drop velocity of G21L2 (top) and G12L2 (bottom), at $y = 0$ (left) and $y = -0.7R$ (right), together with the mean axial-velocity of the droplets (solid lines). The dashed lines in the top left graph represents the velocity a droplet has obtained when it reaches the center of the pipe (i.e. when it is entrained for $t = \frac{1}{2}t_{res}$); the droplet is accelerated from stand-still in the mean gas-velocity profile of the LES with uniform roughness, while gravity is opposing the drag force ($C_D = 24/Re_{dr} + 0.44$, where Re_{dr} is the droplet Reynolds-number based on the droplet slip-velocity and drop diameter). The symbols plotted on these lines are for the drop sizes with $\tau_{dr} = t_{res}$. In the bottom right graph is also plotted a solid line corresponding to $u_{z,dr} = 3$ m/s.

are still accelerating, hence their slip velocity depends strongly on both the residence time and the drop size.

In fig. 2.12 we have plotted the mean droplet slip-velocity, defined as: $\langle u_{z,s,dr} \rangle = \langle u_{z,g} \rangle - \bar{u}_{z,dr}$; using this definition the contribution of the larger droplets has a stronger weight. As a consequence, the slip velocity increases toward the center of the pipe, i.e.: the gas-phase velocity increases more strongly toward the center of the pipe than the mass-weighted velocity of the droplets.

For the cocurrent flow conditions we see a strong dependency on u_{sl} , which is absent in the churn-annular flows. Probably, this is a result of the droplet residence-time, which also depends on u_{sl} in the cocurrent-flow, but not in the churn-annular flow, see section 2.5.4. An increase of the residence-time decreases the slip-velocity.

Since the slip-velocity is very large, the presence of the droplets will affect the pressure-gradient (see 2.5.5) and/or the turbulence of the gas-phase, see fig. 2.6. From an order

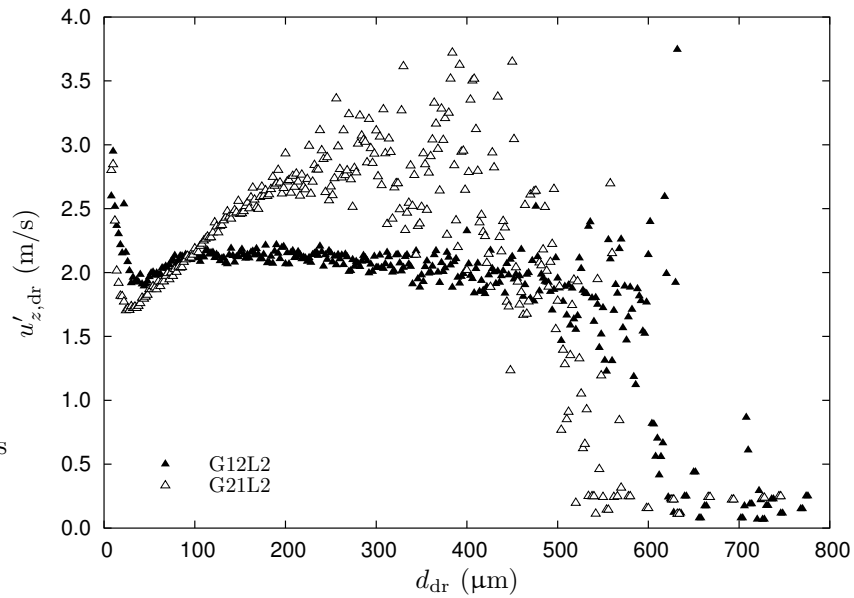


Figure 2.11: Standard deviation of droplet axial-velocity for G12L2 and G21L2 in the center of the pipe.

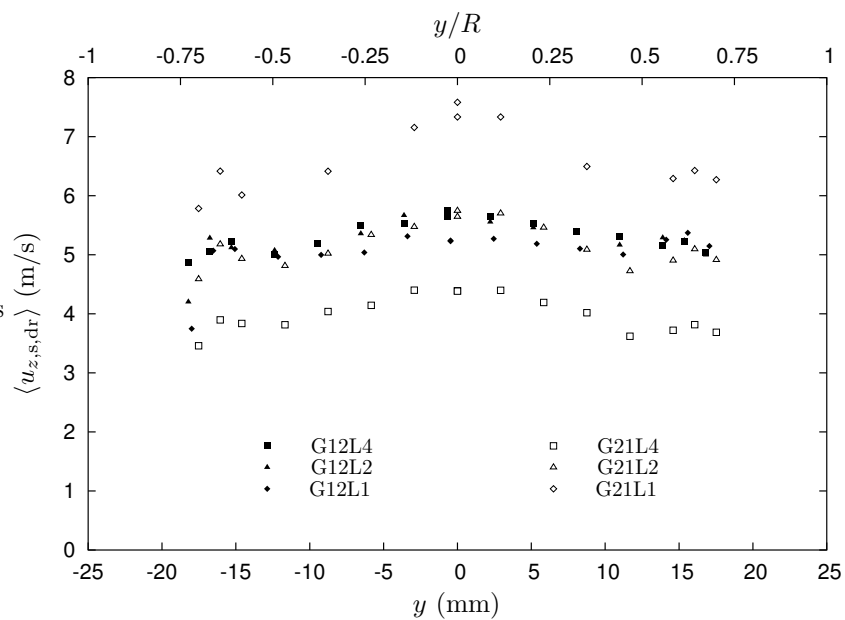


Figure 2.12: Droplet slip velocity in cross-section of the pipe.

of magnitude analysis, Hetsroni (1989) suggested that droplets with $Re_{dr} \gtrsim 400$ tend to enhance turbulence. However, at the center of the pipe, only about 0.1% of the droplets have $Re_{dr} > 400$, whereas about 80% of the droplets have $Re_{dr} < 50$; for the latter group Tsuji et al.(1984) showed that it diminishes turbulence (see Azzopardi (1999)).

Lateral velocity

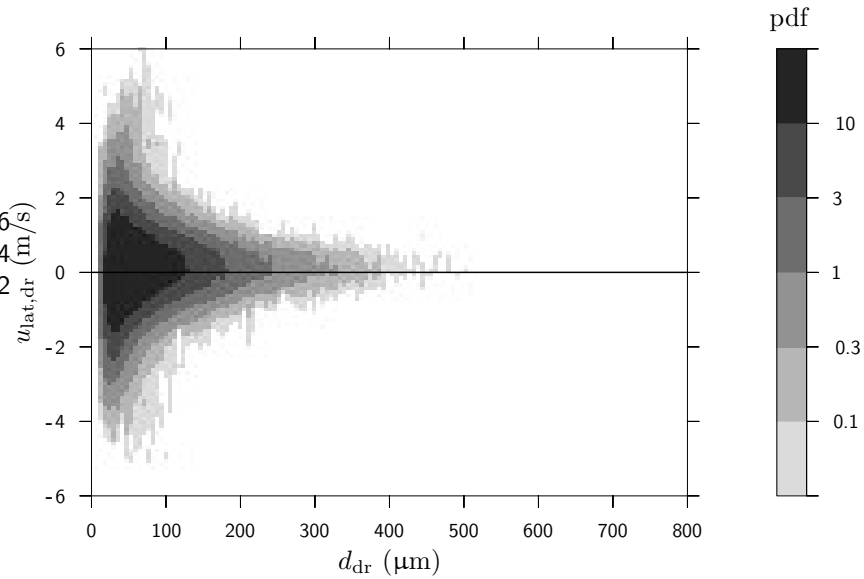


Figure 2.13: Joint pdf of drop-size and droplet lateral-velocity for G21L2 in the center of the pipe.

In fig. 2.13 we show the joint pdf of drop size and droplet lateral-velocity for G21L2 in the center of the pipe. From this it is clear that the maximum lateral velocity decreases with increasing drop size, suggesting that the minimum residence-time increases with increasing drop size ($1/t_{res,min} \propto u_{lat,dr,max}$). Because in fig. 2.10 the dashed line with $t_{res} = 0.50$ s follows roughly the upper boundary, the maximum residence-time is roughly equal for all drop sizes, and thus we expect the mean residence time to increase with increasing drop size, see also fig. 2.15.

In fig. 2.14 we show the mean drop-size for a given value for the droplet axial-velocity and lateral-velocity. Smaller droplets have in general a larger lateral-velocity, see fig. 2.13, thus we see that in the center of the pipe (left graph) the mean drop-size decreases with increasing lateral-velocity. Also, a smaller droplet will accelerate faster, obtaining larger axial-velocities; this is observed in the center of the pipe as well: an increase in axial-velocity decreases the mean drop-size. Furthermore, since a decrease in lateral velocity results in an increase in the residence-time, we see that for a given mean drop-size the axial-velocity increases with decreasing lateral-velocity (i.e. the droplets have accelerated longer).

Closer to the interface at $y = -0.7R$ (right graph), we see that the symmetry is lost: there is a large difference between (i) the ‘young’ droplets that are recently entrained, moving toward the center of the pipe ($u_{lat,dr} > 0$), and (ii) the ‘old’ droplets that already have

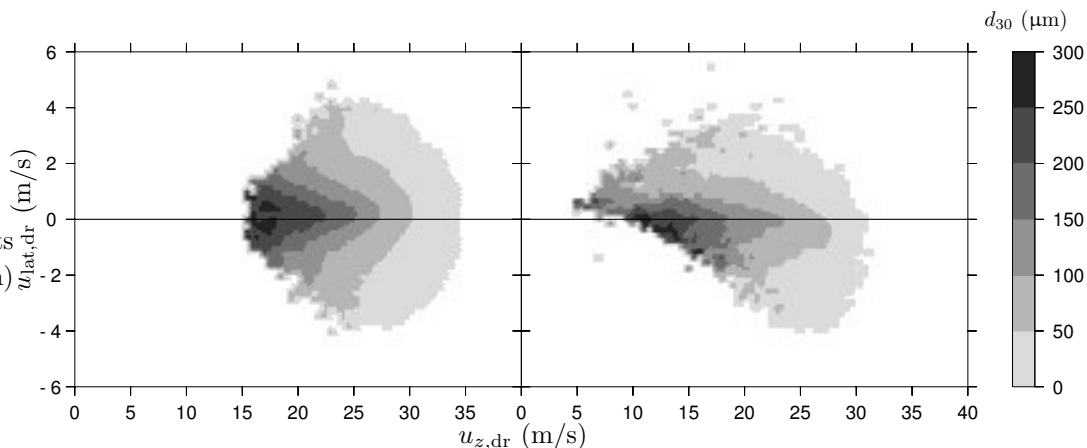


Figure 2.14: Volume-averaged volume-mean-diameter for G21L2 at $y = 0$ (left), and at $y = -0.7R$ (right). Positive values of $u_{\text{lat,dr}}$ at $y = -0.7R$, represent droplets moving toward the center, and negative values of $u_{\text{lat,dr}}$ those moving toward the interface. In the center of the pipe all droplets move toward the interface.

crossed the pipe cross-section and move toward the interface ($u_{\text{lat,dr}} < 0$). The old droplets have accelerated for a much longer time-span, and have therefore in general a larger axial-velocity. The young droplets are accelerating more strongly, hence for a given mean drop-size an increase of the lateral-velocity (i.e. a decrease of the residence-time) results in a strong decrease in the axial-velocity.

2.5.4 Residence time

With the PDA we can not measure the residence-time of an individual droplet directly. However, we need the residence-time to determine R_{at} (eq. 2.4), or to make a prediction of the droplet axial-velocity, both of which are determining ∇p_{dr} .

Assuming that the droplets move ballistically, the droplet lateral-velocity is well correlated with the droplet residence-time, eq. 2.5. Because there exists a large variation in the droplet lateral-velocity (both magnitude and direction), the droplet residence-time is spread as well. With our PDA we can only measure one component of the droplet lateral-velocity, hence we can not use it for computing the residence-time.

Instead, we use eq. 2.3 and eq. 2.4 to calculate the residence-time from the centerline pressure-gradient (eq. 2.9).

In fig. 2.15 we show the results of $\frac{1}{2}t_{\text{res,dr}}$ (i.e. the time in which a droplet can reach the centerline of the pipe), computed with eq. 2.12. Also, we plot the Stokes relaxation time of the droplets (dashed line).

We observe that for $d_{\text{dr}} \lesssim 40 \mu\text{m}$ the residence-time increases with decreasing drop-size, because smaller droplets behave more like tracers. Since the gas-phase radial-velocity is zero at the gas-liquid interface, tracers remain, in principle, forever in the gas-stream. The tracer-droplets we use are not ideal tracers, hence they have a finite residence-time.

For $d_{\text{dr}} \gtrsim 60 \mu\text{m}$ we see that the average residence-time increases with increasing drop-size.

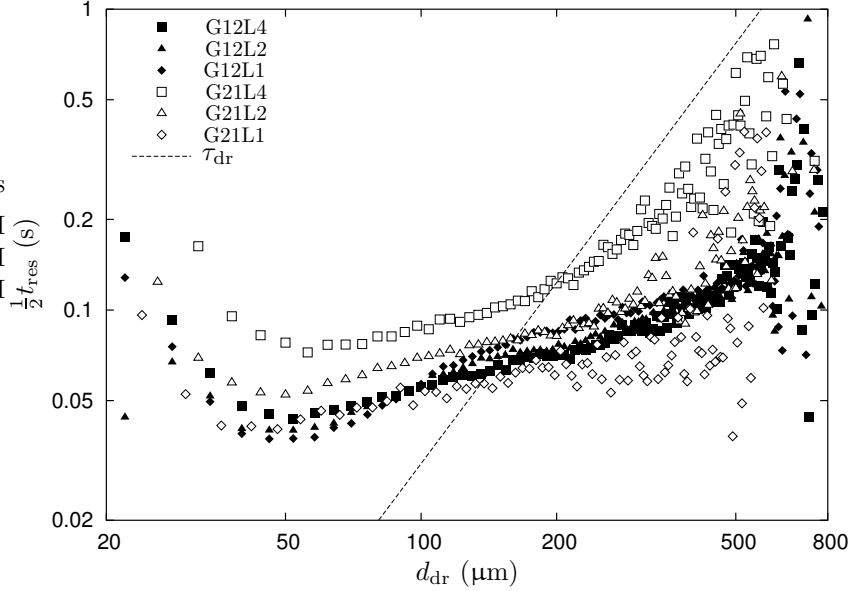


Figure 2.15: The time in which a droplet can reach the centerline of the pipe, $\frac{1}{2}t_{\text{res,dr}}$, is plotted versus the drop-size. For comparison the relaxation time is shown as well (dashed line).

This is because the maximum droplet lateral-velocity decreases with increasing drop-size, see section 2.5.3, resulting in an increase of the minimum residence-time, see eq. 2.5. This is also visible in the top left graph of fig. 2.10: for larger droplets the ‘lower border’ of the joint-pdf does not follow the dashed line with $t_{\text{res}} = 0.02$ s.

According to Lopes and Dukler (1986), and references therein, the droplet lateral-velocity is proportional to the friction velocity. Since the variation in u_{∇} between the measured flow conditions is rather small (about a factor 1.6), this can explain the small variation in the droplet residence-time (about a factor 2). However, since $u_{\nabla,\text{G21L1}} < u_{\nabla,\text{G21L4}}$, we expect $t_{\text{res,G21L1}} > t_{\text{res,G21L4}}$, whereas the opposite is observed. Moreover, we see a variation in u_{∇} for the churn-annular flows with u_{sl} , but the residence-time is more or less equal. The reason for this is not yet clear, but is probably strongly related to the droplet ejection phenomena at the interface, which we were unable to determine.

From fig. 2.15 it is clear that the droplets with $d_{\text{dr}} \gtrsim 100$ μm have an average relaxation-time of the order of or larger than $\frac{1}{2}t_{\text{res,dr}}$. Therefore, these droplets are still accelerating at the center of the pipe, resulting in a large slip-velocity, see section 2.5.3.

2.5.5 Dispersed-phase pressure-gradient

The dispersed-phase pressure-gradient is estimated using eq. 2.9, i.e. directly from the PDA-measurements. However, we can only perform measurements for $|y| < 0.7R$, whereas in the region $0.7R < |y| < R$ the contribution to ∇p_{dr} may be significantly larger: closer to the interface the droplets that move away from the interface accelerate stronger. Here, the overall

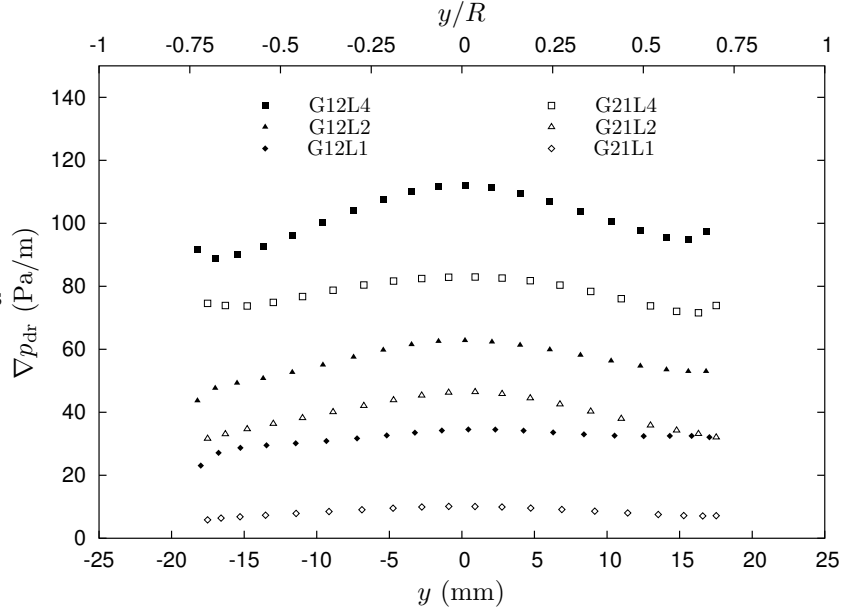


Figure 2.16: Dispersed-phase pressure-gradient calculated with the direct method in the cross-section of the pipe.

pressure-gradient, which is given in table 2.4, is calculated as the average value for $|y| < 0.7R$.

In fig. 2.16 the profile of ∇p_{dr} in the pipe cross-section is plotted, from which we observe that ∇p_{dr} is slightly core-peaking. This is probably caused by the droplet slip-velocity, since the droplet concentration and the drop-size are nearly constant over the cross-section. The product $C u_{z,s,dr}^2 d_{32}^2$ is the most important factor in the dispersed-phase pressure-gradient; for G12L1 and G21L2 this product is almost equal, hence ∇p_{dr} is roughly equal. The differences are mainly due to the different drag-coefficient for the two flow-conditions.

The acceleration of the dispersion is characterised by: $a_{z,dr} \approx \bar{u}_{z,dr}/t_{res} \approx \nabla p_{dr}/(\rho_1 \alpha_{dr})$, and is shown in fig. 2.17, using ∇p_{dr} at the center of the pipe. From fig. 2.17 it is clear that (i) the acceleration of the droplets is much more important than their weight, $a_{z,dr} \gg g$, (ii) droplets with a diameter $d_{dr} \approx 50 \mu\text{m}$ accelerate strongest, resulting in the largest pressure-gradient per unit of holdup, and (iii) a smaller residence-time results in a larger mean acceleration, see also fig. 2.15.

When we compare a churn-annular flow and a cocurrent annular flow with an equal holdup, and an equal acceleration, e.g. G12L2 and G21L4, we observe that ∇p_{dr} is larger for the cocurrent flow than for the churn-annular flow. Because the droplets in G21L4 are on average smaller than in G12L2, they accelerate stronger. Therefore, per unit of holdup, the dispersion of G21L4 can subtract energy more efficiently from the system than the dispersion of G12L2, resulting in a larger ∇p_{dr} .

Since the residence-time of tracer-droplets is relatively large, see fig. 2.15, their mean acceleration is small (i.e. their contribution to the pressure-gradient ideally is zero).

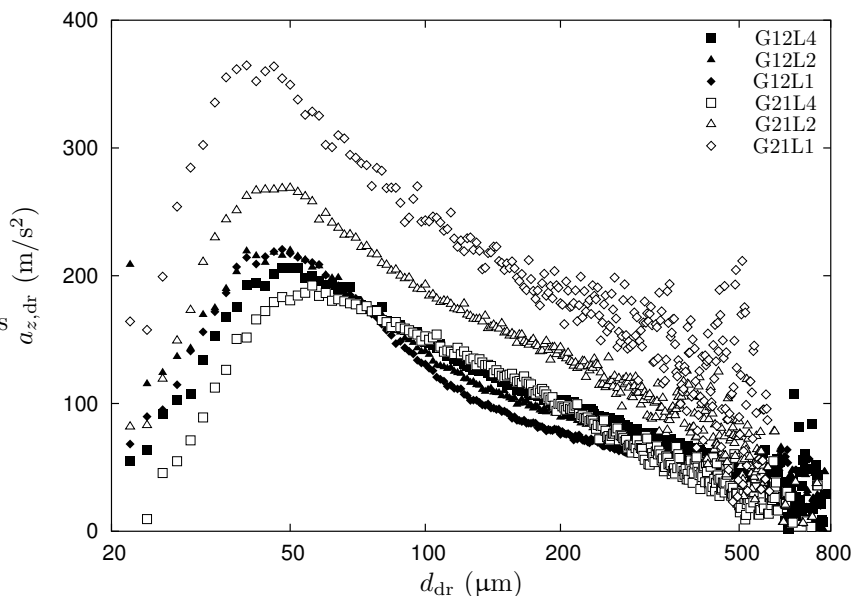


Figure 2.17: Acceleration of droplets.

2.5.6 Flow reversal

In fig. 2.10 we observe that for G12L2 at $y = -0.7R$ almost all droplets move with an axial-velocity $u_{z,dr} \gtrsim 3$ m/s. When droplets would flow counter-current in the churn-annular flow, causing liquid down-flow as proposed by Turner et al. (1969), we can not measure them directly: due to the film extraction droplets are not created downstream of the PDA-detection volume. However, if Turners idea is true, we expect to find a large amount of droplets that move with an axial-velocity close to zero, and that these droplets are very large. Since only 0.4% of the dispersed-phase holdup is by droplets with an axial-velocity close to zero ($u_{z,dr} < 3$ m/s), and since their mean volume-diameter is about $200 \mu\text{m}$, the idea that the droplets directly cause liquid loading is unlikely. Note that the maximum detected diameter of these slowest droplets is only about $350 \mu\text{m}$, which is much smaller than 8.5 mm which is the droplet diameter that is supposed to cause down flow. Moreover, since it is expected that droplets are created with a maximum initial drop-diameter of the order of the film-thickness, coalescence should be very important in order to obtain such large drop sizes. This is not supported by fig. 2.8, showing the free-path-length of the droplets.

The droplets may still affect the flow reversal, since they are expected to decrease the gas-phase velocity near the gas-liquid interface, and hence the interfacial shear. A decrease in the interfacial shear may lead to an instability of the liquid film.

For G21L4 an amount of 43% of the liquid flow rate is entrained, contributing about 10% of the total pressure-gradient. If we would have no entrainment, with equal gas and liquid flow rates, this would result in an increase of both the liquid film-thickness and the interfacial

shear of about 20% (assuming a parabolic velocity profile in the liquid film, with no slip and zero shear at the pipe wall). Hence the total pressure gradient would be about 8% larger without entrainment. This suggests that for a given total pressure-gradient and liquid flow-rate in a cocurrent annular flow, the gas flow-rate is larger with entrainment than without it. The liquid down-flow as caused by an instability of the liquid film will be delayed with increasing entrainment, since for a cocurrent annular flow the liquid film-thickness decreases with increasing entrainment.

However, once the film becomes unstable and film-churning is occurring we speculate that locally the transport of liquid in the film stalls, and liquid will accumulate, making the film-thickness very large and independent of the amount of entrainment. In such a case, the only effect of the dispersed-phase will be a decrease in the interfacial shear, increasing the liquid down flow.

2.6 Conclusion

In this paper we have investigated six vertical upward annular air-water pipe-flows in a 50 mm diameter pipe: three in the churn-annular regime with $u_{sg} = 12$ m/s, and three in the cocurrent annular regime with $u_{sg} = 21$ m/s. For both flow regimes the liquid flow-rates are set at $u_{sl} = 1, 2$ or 4 cm/s. We have used a PDA to measure the pdf of both drop-size and droplet-velocity at 15 locations in the pipe-cross-section. The total pressure-gradient, the amount of entrainment and the liquid down-flow are measured simultaneously. With the PDA-measurements we can make an estimate of the gas-phase mean velocity and velocity fluctuations and of the dispersed-phase drop-size, drop-velocity, concentration and pressure-gradient.

The gas-phase of a cocurrent annular flow, seems to behave similarly to a single-phase pipe-flow with a uniform wall-roughness. In contrast, the churn-annular flows show a rather uniform gas-phase velocity-fluctuation profile, the reason for this is not yet understood. For all flow conditions the gas-phase velocity-fluctuations scale roughly with the friction velocity. For both the churn-annular flows and the cocurrent annular flows the drop-size distribution has an exponential decreasing tail, and a fall-off at the smallest drop-sizes. Breakup and coalescence seem not to be dominant processes in the core of the flow for the flow conditions we measured, and the drop-size distributions are determined by the atomisation process. When breakup and coalescence is not occurring in the core of an annular flow, the mean droplet size is not expected to vary. Comparing with Fore and Dukler (1995a), we find a good agreement on the average dispersed-phase properties (R_{at} , δ_f , ∇p_{dr} and ∇p_{tot}) in the cocurrent annular flow for the smaller liquid flow-rates, $u_{sl} < 3$ cm/s. Using their model we have estimated the droplet residence-time from the PDA-data, which is an important parameter in predicting the dispersed-phase pressure-gradient.

Since the mean residence-time of the droplets is of the order of or smaller than the relaxation time for the droplets with $d_{dr} \gtrsim 100$ μm , these droplets are constantly accelerating, and their acceleration is much stronger than the gravitational acceleration. A continuous acceleration in combination with a spread in the residence time results in the large spread of the droplet axial velocities. For the majority of the droplet-population, the slip-velocity is much larger than the terminal free-fall velocity in a stagnant medium. The dispersed-phase pressure-gradient is maximum about 10% of the total pressure-gradient for the flow conditions we have measured.

We have not observed any droplet flowing counter-currently with the gas-flow, making the physical background of the Turner criterion for liquid loading implausible.

The presence of entrained liquid decreases the total pressure-gradient and the interfacial shear. Since an increase in entrainment decreases the liquid film-thickness in a cocurrent flow, the liquid film will be more stable. In a churn-annular flow the entrainment may not influence the liquid film-thickness, and the reduced interfacial shear increases the down-flow.

3. Pressure gradient and deposition of a dispersed phase

The origin and the dependencies of the pressure-gradient due to particles that are injected with an initially small axial-velocity into a turbulent pipe flow is investigated by means of a quasi-1D simulation and a 3D-LES. It is shown that the dissipation of energy during the acceleration of the particles is the main contributor to the pressure-gradient. The dependence of the pressure-gradient on the size of the particles can be understood by considering the time scales related to the particle inertia, the dimensions of the pipe and the large-scale turbulence.

This chapter is to be submitted for publication in AIChE J.

3.1 Introduction

In the exploitation of gas-wells liquid (water, oils, condensates) is usually produced simultaneously. The flow pattern inside the production tubing is an annular dispersed two-phase flow, the liquid phase flows partly as a wavy film along the pipe circumference, and partly as entrained droplets in the turbulent gas core. The dispersed droplet phase plays an important role in such flows concerning issues like deposition at and creation of the liquid film, erosion/corrosion in bends and pressure-gradient effects.

Lopes and Dukler (1986) showed the dispersed-phase pressure-gradient to be up to 20% of the total pressure-gradient, due to the acceleration of the droplets that move initially with a relatively low axial velocity. For such flow conditions the mass loading can amount up to about 0.6, and in order to simulate these flows, we need to solve a high Reynolds-number flow, where the feedback force of the dispersion onto the continuous phase (two-way coupling) is of crucial importance. Moreover, we need a method to mimic the atomisation and deposition processes at the gas-liquid interface.

However, most of the numerical studies in the literature of dispersed flows deal with dilute flows, in which the feedback force of the dispersion is negligible (one-way coupling). There are only a few studies that include the feedback force, and in general these are for low Reynolds number flows. Pan and Banerjee (1996), Li et al. (2001), and Mito and Hanratty (2006) performed direct numerical simulations (DNS) of a channel flow with a Reynolds number based on the friction velocity and the channel half-width, Re_τ , in the range of 125-150, while Rani et al. (2004) used a DNS in a pipe flow with $Re_\tau = 180$, based on the pipe radius. Using a large eddy simulation (LES), Yamamoto et al. (2001) and Segura (2004) have simulated a

channel flow with $Re_r = 645$.

Moreover, in general, the interaction of the dispersed phase with the wall is treated using elastic or slightly inelastic bouncing, assuming local equilibrium between atomisation and deposition, and a small nett transfer of axial momentum to the wall by the dispersion. As a consequence, the effect of the dispersion on the pressure gradient is rather limited. To our knowledge, only Mito and Hanratty (2006) performed a simulation in which they explicitly prescribed the atomisation in combination with perfectly absorbing walls. However, they injected the particles in the flow with an initial axial-velocity equal to the bulk velocity, making the influence on the pressure gradient by the dispersion small as well.

Therefore, we study in this paper the phenomenon of a dispersion injected with an initially small axial velocity into a high Reynolds-number upward flow, which helps us to understand the origin and the dependencies of the dispersed-phase pressure-gradient.

We will show that the size of the vorticity layer plays an important role in understanding the dispersed-phase pressure-gradient. In the vorticity layer near the wall the gas-phase axial-velocity increases from zero at the wall to roughly the centerline velocity. After injection, the particles will accelerate in the vorticity layer, and, if they are very inert, also in the core of the flow. Prior to deposition, the particles will decelerate in the vorticity layer, but only if their inertia is small enough. The acceleration and deceleration in the vorticity layer are opposing mechanisms, and result in a non-monotonic behaviour of the dispersed-phase pressure-gradient with respect to the inertia of the particles. This non-monotonic behaviour can be understood by considering the time scales, coupled to the size of the vorticity layer, the dimensions of the pipe (both in combination with an appropriate velocity), and the inertia of the particles.

We have performed two types of simulations:

- a quasi-1D simulation, in which the gas-flow is described by a piecewise linear velocity profile. In this simplified representation of a turbulent flow particles are injected, and from their trajectories we can deduce their impact on the pressure-gradient. In this way we can better focus on the relevant time scales involved.
- a full 3D LES, that allows us to introduce a turbulent flow, that is affected by the dispersion. We have explicitly described the atomisation process by controlling the injection of each individual particle, and combined this with perfectly absorbing walls.

In section 3.2 we present the details of the simulations, and in section 3.3 we show and discuss their results. Concluding remarks are given in section 3.4.

3.2 Simulations

For both the quasi-1D simulation and the 3D LES, we have simulated an air-water vertical-upward annular-dispersed pipe-flow with a superficial gas-velocity, $u_{sg} \approx 20$ m/s, and pipe diameter, $D = 0.05$ m, see also fig. 3.1. The gas phase is described by its density, $\rho_g = 1.2$ kg/m³, and its dynamic viscosity, $\mu_g = 1.8 \cdot 10^{-5}$ kg/ms, hence the superficial gas Reynolds-number is $Re_{sg} \approx 67,000$. The droplets are represented by spherical particles with a density of $\rho_p = 1000$ kg/m³, and they are driven by drag and gravity only. To focus on the effect of the particle acceleration, we deliberately kept the situation as simple as possible, leaving

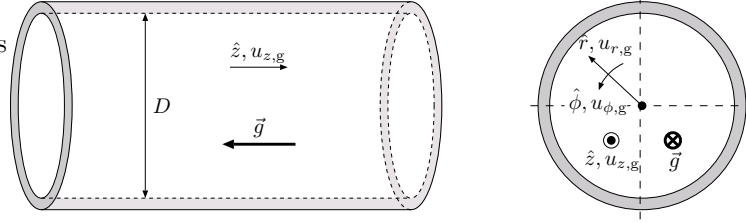


Figure 3.1: Computational domain, together with position and velocity coordinates. The gravity is directed downwards.

out all other forces acting on the particles, as well as inter-particle collisions. The drag was computed using a drag-coefficient:

$$C_D = \frac{24\mu_g}{\rho_g |\vec{u}_g - \vec{u}_p| d_p} + 0.44 \quad (3.1)$$

which gives a good approximation of the standard drag curve, according to Govan (1989). \vec{u}_g and \vec{u}_p are the gas-phase and the dispersed-phase velocity-vectors, respectively. The direction of the gravitational acceleration, \vec{g} , is opposite to the mean gas-flow for all simulations, with $|\vec{g}| = 9.8 \text{ m/s}^2$.

3.2.1 Quasi-1D approach

The quasi-1D simulations are kept as simple as possible in order to better understand the origin of the relevant time-scales. We have prescribed a gas-phase flow field in which particles are injected. The local gas-phase axial-velocity, $u_{z,g}$, is given by:

$$u_{z,g} = \begin{cases} u_{z,g,c} & r < \frac{1}{2}D - \delta_\omega \\ u_{z,g,c} (\frac{1}{2}D - r) / \delta_\omega & r > \frac{1}{2}D - \delta_\omega \end{cases} \quad (3.2)$$

$$u_{z,g,c} = \langle u_{z,g} \rangle + 4.07u_\tau = \langle u_{z,g} \rangle \left(1 + 4.07\sqrt{f/2} \right) \quad (3.3)$$

where r is the radial position in the pipe, and δ_ω is the vorticity thickness of the flow. The radial-velocity, $u_{r,g}$, the tangential velocity, $u_{\phi,g}$, and all velocity fluctuations are set to zero. $u_{z,g,c}$ is the centerline axial-velocity of a turbulent flow, and f is the fanning friction-factor, see also Schlichting (1979). $u_\tau = \sqrt{\langle \tau_{rz,w} \rangle / \rho_g}$ is the friction velocity, and $\langle \tau_{rz,w} \rangle$ is the average wall-shear. We have used the Churchill-relation to calculate the friction factor, see Churchill (1977).

$$\frac{f}{2} = \sqrt[12]{\left(\frac{8}{\text{Re}_{\text{sg}}}\right)^{12} + \left(\left[2.457 \ln\left(\left(\frac{7}{\text{Re}_{\text{sg}}}\right)^{0.9} + 0.27\frac{k_s}{D}\right)\right]^{16} + \left(\frac{37530}{\text{Re}_{\text{sg}}}\right)^{16}\right)^{-\frac{3}{2}}} \quad (3.4)$$

$$\text{Re}_{\text{sg}} = \frac{\rho_g \langle u_{z,g} \rangle D}{\mu_g} \quad (3.5)$$

where k_s is the hydraulic wall-roughness.

We have set the vorticity thickness equal to the displacement thickness, i.e.:

$$\delta_\omega = D \left(1 - \sqrt{\langle u_{z,g} \rangle / u_{z,g,c}} \right) \quad (3.6)$$

In fig. 3.2 we have plotted the vorticity thickness normalised with the pipe diameter for varying k_s , and in fig. 3.3 for varying u_{sg} .

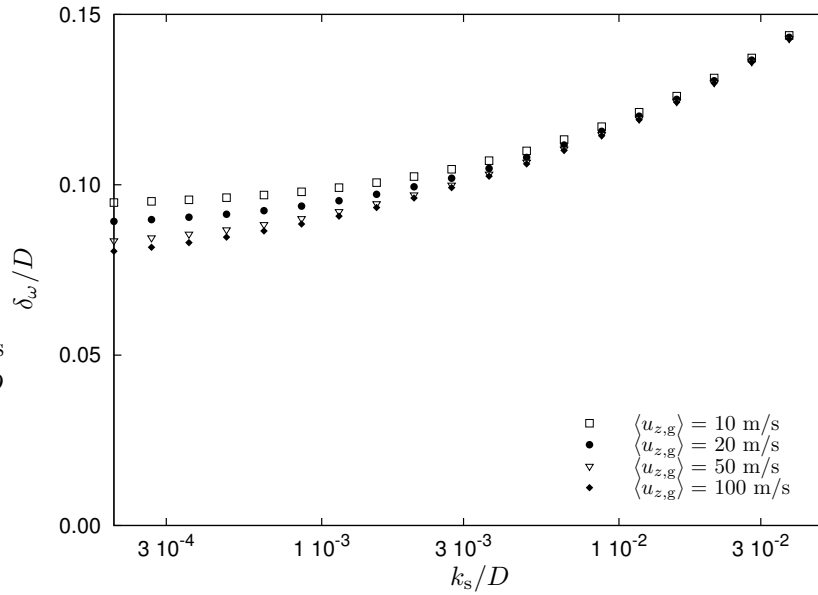


Figure 3.2: Vorticity thickness normalised with the pipe diameter with varying hydraulic roughness. For the symbols we have used the Churchill relation to compute the friction factor.

We inject particles with a given drop-size, d_p , in the 1D flow-field described above at $r = \frac{1}{2}D$ and $z = 0$, perpendicular to the pipe wall with a negative radial-velocity, $u_{r,p}$, and a zero tangential and axial velocity. The radial velocity is only introduced to make the particles see a varying flow-field, and is kept constant for a single particle-trajectory. We have not used the radial velocity for computing the drag coefficient, see eq. 3.1, nor for calculating the particle momentum or kinetic energy. The particle trajectories are calculated numerically with a second-order Adams-Bashforth method, using a time-step, $\Delta t = \min(10^{-5} \tau_p, 10^{-6} t_{res})$. The time scales that are relevant for the particle motion are: (i) the relaxation time of the particle, τ_p , (ii) the residence-time of the particles, t_{res} , and (iii) the vorticity time, t_ω .

$$\tau_p = \frac{\rho_p d_p^2}{18\mu_g} \quad (3.7)$$

$$t_{res} = D/|u_{r,p}| \quad (3.8)$$

$$t_\omega = \delta_\omega/|u_{r,p}| \quad (3.9)$$

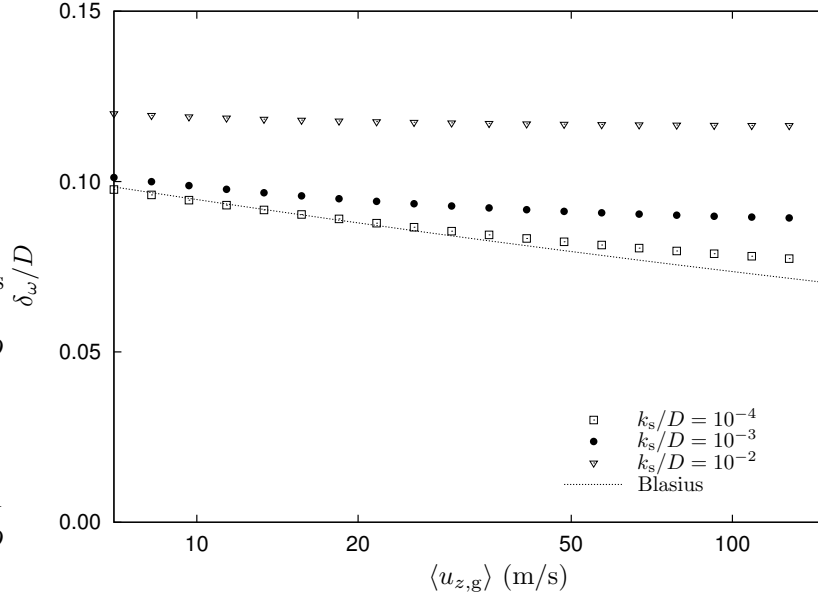


Figure 3.3: Vorticity thickness normalised with the pipe diameter with varying mean gas-phase axial-velocity. For the symbols we have used the Churchill relation to compute the friction factor, and for the dotted line we have used the Blasius correlation to calculate the friction factor, representing a smooth wall, see eqs. 3.6-3.3.

The total dispersed-phase pressure-gradient, $\frac{d}{dz}p_{p,tot}$, is calculated via a momentum-balance over the dispersed phase assuming a fully developed situation, see Lopes and Dukler (1986) and Westende et al. (2007b):

$$-\frac{d}{dz}p_{p,tot} = \frac{4}{D_h}R_{at,m}(u_{z,p,dep} - u_{z,p,at}) + \rho_p\alpha_p g \quad (3.10)$$

$$R_{at,m} = \frac{\rho_p\alpha_p D_h}{4t_{res}} \quad (3.11)$$

where α_p is the dispersed-phase holdup, and $R_{at,m}$ is the mass atomisation-rate. D_h is the hydraulic diameter, g is the gravitational acceleration, and $u_{z,p,dep}$ and $u_{z,p,at}$ are the particle axial deposition-velocity and axial atomisation-velocity, respectively.

The total pressure-gradient can be divided into several contributions, corresponding to the change in kinetic energy, $\frac{d}{dz}p_{p,kin}$, the change in gravitational energy, $\frac{d}{dz}p_{p,grav}$, and the dissipation of energy, $\frac{d}{dz}p_{p,diss}$. Using an energy balance over a single particle trajectory, we

define the pressure-gradient contributions with:

$$-\frac{d}{dz}p_{p,\text{kin}} = -\frac{d}{dz}p_{p,\text{tot}} \frac{\Delta E_{p,\text{kin}}}{\Delta E_g} \quad (3.12)$$

$$-\frac{d}{dz}p_{p,\text{grav}} = -\frac{d}{dz}p_{p,\text{tot}} \frac{\Delta E_{p,\text{grav}}}{\Delta E_g} \quad (3.13)$$

$$-\frac{d}{dz}p_{p,\text{diss}} = -\frac{d}{dz}p_{p,\text{tot}} \frac{E_{p,\text{diss}}}{\Delta E_g} \quad (3.14)$$

$$\Delta E_g = \Delta E_{p,\text{kin}} + \Delta E_{p,\text{grav}} + E_{p,\text{diss}} \quad (3.15)$$

where $\Delta E_{p,\text{kin}}$, and $\Delta E_{p,\text{grav}}$ are the change in particle kinetic and gravitational energy over a single trajectory, respectively. $E_{p,\text{diss}}$ is the dissipation of energy for a single trajectory, and ΔE_g is the change in gas-phase energy due to the acceleration/deceleration during a single particle trajectory.

Since we take the initial velocity, and the initial axial position of the particles as zero, we have:

$$\Delta u_{z,p} = u_{z,p,\text{dep}} \quad (3.16)$$

$$\Delta E_{p,\text{kin}} = E_{p,\text{kin,dep}} \quad (3.17)$$

$$\Delta E_{p,\text{grav}} = E_{p,\text{grav,dep}} \quad (3.18)$$

where $E_{p,\text{kin,dep}}$ and $E_{p,\text{grav,dep}}$ are the kinetic energy and the gravitational energy of the particle at the moment of deposition, respectively.

3.2.2 3D simulation

Gas phase

In the 3D-simulation we use an Eulerian-Lagrangian LES with the standard point-particle approach, see, e.g., Yamamoto et al. (2001), and Portela and Oliemans (2003).

For the continuous phase, the gas velocity, \vec{u}_g , is simulated using LES. The filtered continuity and Navier-Stokes equations, that are solved for the gas-phase, are,

$$\vec{\nabla} \cdot \vec{u}_g = 0 \quad (3.19)$$

$$\frac{\partial \vec{u}_g}{\partial t} + (\vec{u}_g \cdot \nabla) \vec{u}_g = -\frac{1}{\rho_g} \vec{\nabla} p + \nu_g \nabla^2 \vec{u}_g + \vec{\nabla} \cdot \vec{T}_s + \frac{1}{\rho_g} C_p \vec{F}_{D,p \rightarrow g} \quad (3.20)$$

with ν_g being the kinematic viscosity of the gas-phase. The influence of the subgrid motion on the resolved gas-velocity is represented by the extra stress-tensor, \vec{T}_s , and, in case of two-way coupling, the influence of the dispersed-phase on the gas-phase by $\frac{1}{\rho_g} C_p \vec{F}_{D,p \rightarrow g}$. C_p is the particle concentration and $\vec{F}_{D,p \rightarrow g}$ is the feedback force of the drag that acts on an individual particle.

The in-house code that is used for the calculations solves eqs. 3.19 and 3.20 using a finite-volume single-phase solver with a predictor-corrector method. In the predictor part, a leap-frog method, explicit in the radial and axial directions and implicit in the tangential direction,

is used for progress in time. In the corrector step, the continuity equation is enforced using the Poisson equation for incompressible flows. The time-step is determined with the Courant criterion. The stress-tensor, $\vec{\vec{T}}_s$, is computed using the standard Smagorinski model, with the Smagorinski constant $C_s = 0.1$. Van Driest wall-damping is also applied, with $c_A = 25\nu_g/u_\tau$. The particle feedback force is computed directly from the particle-tracking, see section 3.2.2. A staggered-grid in cylindrical coordinates is used and periodic boundary conditions are applied in the axial direction. In fig. 3.1, the computational domain with the corresponding position and velocity coordinates for the axial, tangential, and radial directions is drawn. For all the simulations, the gridpoints are uniformly distributed in the tangential and axial directions, with $N_\phi = N_z = 192$. The length of the computational domain in the axial direction is $L_z = 5D$. In the radial direction the grid is stretched, using a hyperbolic-tangent function,

$$r_i = \frac{\tanh(c_{r1}i/c_{r2})}{2 \tanh(c_{r1})} D \quad 0 < i < N_r \quad (3.21)$$

using the following constants: $N_r = 32$, $c_{r1} = 2.45$ and $c_{r2} = 40$. This grid has a wall-nearest grid-point at a distance from the wall, $y_{N_r} \approx D/68$, a grid-spacing near the wall, $\Delta y_w \approx D/350$, and a grid-spacing in the center $\Delta y_c \approx D/32$. Note that because we are using wall-functions, the first grid-point near the wall is located in the logarithmic layer, and is at a larger distance from the wall than the near-wall grid spacing.

In order to account for wall-roughness, imitating the rough wavy gas-liquid interface, we

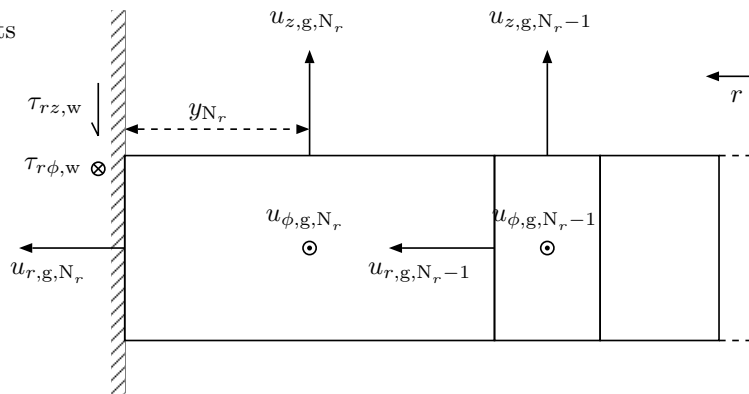


Figure 3.4: Wall-shear for wall-nearest grid-cell

have implemented a modified version of the Schumann wall-function for the near-wall region, $0 < y/D < 0.015$, see, e.g., Piomelli et al. (1989), and Westende et al. (2007a). The boundary

conditions for the grid-cells near the wall (see fig. 3.4) are:

$$u_{r,g,N_r} = 0 \quad (3.22)$$

$$\tau_{r\phi,w} = -\rho_g \nu_g \frac{u_{\phi,g,N_r}}{y_{N_r}} \quad (3.23)$$

$$\tau_{rz,w} = f \frac{1}{2} \rho_g \langle u_{z,g} \rangle^2 \frac{u_{z,g,N_r}}{\langle u_{z,g,N_r} \rangle_z} \quad (3.24)$$

where u_{r,g,N_r} , u_{ϕ,g,N_r} and u_{z,g,N_r} represent the instantaneous radial, tangential and axial velocity at the wall-nearest grid point, respectively. The two components of the wall-shear are given by $\tau_{r\phi,w}$ and $\tau_{rz,w}$, and y_{N_r} is the ‘distance to the wall’ for the wall-nearest grid-point. $\langle u_{z,g,N_r} \rangle_z$ is u_{z,g,N_r} averaged in the axial direction; the quotient $u_{z,g,N_r} / \langle u_{z,g,N_r} \rangle_z$ is used to give $\tau_{rz,w}$ a fluctuating behaviour, and has a mean value of 1. The friction factor is evaluated with eq. 3.4.

More details about the single-phase solver can be found in Eggels (1994).

Dispersed phase

The particles are treated as point-particles and are tracked individually using a non-linear drag (eq. 3.1) and gravity.

Similarly to the continuous-phase, periodic boundary conditions are also applied for the particles: when a particle leaves the domain at $z = 0$ or $z = L_z$, it is re-introduced with the same velocity at the opposite side. The particles progress in time is done with a second-order Adams-Bashforth method. According to Portela and Oliemans (2002), in our case the subgrid motion does not affect significantly the particle motion, since the time scales of the subgrid motion are much smaller than the particle relaxation-time and the subgrid velocity fluctuations are much smaller than the grid-scale velocity fluctuations. Therefore, the influence of the subgrid-scales on the particle motion is neglected. Further details on the particle-tracking can be found in Portela and Oliemans (2003).

When a particle hits the wall it is removed from the flow, hence mimicking the deposition process. At the same moment, a new particle is injected into the flow according to an injection-pdf using a Monte-Carlo technique. In this way we maintain an equal number of particles inside the pipe. The injection-pdf regulates the atomisation, and results from a fit to experimental data of a vertical upward air-water annular-dispersed pipe-flow, see appendix B:

$$\text{PDF} = \text{PDF}_d \text{PDF}_u \quad (3.25)$$

$$\text{PDF}_d = \begin{cases} 0.02443 \exp(-C_d d_p) & 10 \mu\text{m} < d_p < 700 \mu\text{m} \\ 0 & \text{else} \end{cases} \quad (3.26)$$

$$\text{PDF}_u = \begin{cases} 1.064 \exp(-C_u u_{\text{lat},p}^{1.2}) & 0 < u_{\text{lat},p} < 5 \text{ m/s} \\ 0 & \text{else} \end{cases} \quad (3.27)$$

$$C_d = 0.02 \mu\text{m}^{-1} \quad C_u = 1 (\text{m/s})^{-1.2}$$

where $u_{\text{lat},p}$ is the in-plane velocity of the particles, i.e. the projection of the particle velocity vector onto the pipe cross-section. The particles are injected randomly along the pipe wall,

with a random in-plane direction, ensuring an initially negative radial-velocity. The initial axial-velocity is always set to $\frac{1}{10} \langle u_{z,g} \rangle$. Using eq. 3.26 we have: $C_d^{-1} = 0.833 d_{10,\text{inj}} = 0.640 d_{20,\text{inj}} = 0.515 d_{30,\text{inj}} = 0.333 d_{32,\text{inj}} = 0.272 d_{v\mu,\text{inj}}$, where $d_{10,\text{inj}}$, $d_{20,\text{inj}}$, $d_{30,\text{inj}}$, $d_{32,\text{inj}}$, and $d_{v\mu,\text{inj}}$ are the arithmetic-mean, the surface-mean, the volume-mean, the Sauter-mean and the volume-median particle diameter of the injected particles. The average injection-velocity is 0.8 m/s.

Here we note that, according to Lopes and Dukler (1986), in an annular flow the injection velocity can be estimated by the friction-velocity. Thus, using fig. 3.2 or fig. 3.3, and eq. 3.9, the vorticity time can be estimated by the time-scale of the large-scale turbulence, $\mathcal{T} = \mathcal{L}/u_\tau$, because $\mathcal{L} \approx \delta_\omega \approx \frac{1}{10}D$. Hence we have $\mathcal{T} \approx t_\omega \approx \frac{1}{10}t_{\text{res}}$.

Feed back forcing

Two-way coupling is implemented using the drag-force ‘density’ as a local change in the pressure-gradient, i.e. we have used a point-force method, see e.g. Li et al. (2001). We have increased the total pressure-gradient with respect to an unladen case by an amount equal to the average drag-force ‘density’, in order to maintain roughly the same bulk velocity. From a momentum balance over the gas phase, excluding the dispersed phase, we can write the total pressure-gradient as:

$$-\frac{d}{dz}p_{\text{tot}} = 4\tau_{rz,w}/D_h + C_p \left(\vec{F}_{D,g \rightarrow p} \cdot \hat{z} \right) \quad (3.28)$$

where \hat{z} is the axial unit-vector, and $\vec{F}_{D,g \rightarrow p} = -\vec{F}_{D,p \rightarrow g}$ is the drag force acting on an individual particle. The last term on the right hand side of eq. 3.28 can easily be rewritten in the form of eq. 3.10.

According to Belt et al. (2005) the effect of the feedback force of the particles is either (i) a roughness effect or (ii) a blockage effect. When the particles are close to the wall, they act as an added wall-roughness, adjusting the viscous stresses. The total shear at the wall, $\tau_{rz,\text{tot}}$, then consists of a wall-friction contribution, $\tau_{rz,w}$, and a particle-friction contribution, $\tau_{rz,p}$. On the other hand, the particles that are far from the wall block the flow, and decrease the mean velocity and the Reynolds stresses.

In view of the above we identify two contributions to the pressure-gradient: a friction contribution, ∇p_τ , and a blockage contribution, ∇p_b :

$$-\frac{d}{dz}p_{\text{tot}} = 4\rho_g u_\tau^2 / D = -\frac{d}{dz}p_\tau - \frac{d}{dz}p_b \quad (3.29)$$

$$-\frac{d}{dz}p_\tau = 4\rho_g u_{\tau,\text{eff}}^2 / D = 4\tau_{rz,w} / D + \sum_i (1 - H_{y_\tau}) F_{z,D,g \rightarrow p,i} \Big/ \frac{\pi}{4} D^2 L_z \quad (3.30)$$

$$-\frac{d}{dz}p_b = \rho_p \alpha_{p,\text{sc}} a_{\text{eff}} = \sum_i H_{y_\tau} F_{z,D,g \rightarrow p,i} \Big/ \frac{\pi}{4} D^2 L_z \quad (3.31)$$

$$\alpha_{p,\text{sc}} = \sum_i H_{y_\tau} \frac{\pi}{6} d_{p,i}^3 \Big/ \frac{\pi}{4} D^2 L_z \quad (3.32)$$

$$H_{y_\tau} = \begin{cases} 0 & y < y_\tau \\ 1 & y \geq y_\tau \end{cases} \quad (3.33)$$

where u_{∇} is the pressure-gradient velocity, lumping the effects of friction, and blockage together, and $u_{\tau,\text{eff}}$ is the effective friction-velocity, and includes the prescribed wall-friction, $\tau_{rz,w}$, and the particle friction (last term of eq. 3.30). $F_{z,D,g\rightarrow p,i}$ is the axial component of the drag force acting on particle i , and $d_{p,i}$ is the diameter of particle i . $\alpha_{p,sc}$ is the ‘superficial’ core-holdup of the particles, and a_{eff} is the effective acceleration felt by the particles in the core, which includes gravity plus the acceleration of the particles in the core. $H_{y_{\tau}}$ is the Heaviside step-function characterised by the length scale y_{τ} , and determines whether a particle is close to the wall ($y < y_{\tau}$), or that it is in the core of the flow ($y > y_{\tau}$); i.e. it determines whether a particle acts as roughness or as blockage. From the above it seems that y_{τ} is related to the size of the region where the viscous stresses are important, i.e. where the gradient of the mean flow is largest. This suggests that y_{τ} scales with the vorticity thickness, δ_{ω} .

Throughout this paper, the superscript + is used when a quantity is normalised with ρ_g , ν_g , and $u_{\tau,\text{eff}}$. Conventionally, u_{τ} is used for the normalisation. However, for our simulations it is not straightforward that u_{τ} , which is related to the prescribed wall friction, is a better choice for the normalisation than, e.g., u_{∇} ; with two-way coupling, in general, they differ. Instead, we have chosen to normalise with $u_{\tau,\text{eff}}$, since then we recover the log-law in the mean gas-phase axial-velocity, see also section 3.3.2.

Deposition

The number deposition-rate, $R_{\text{dep},N}$, can be described in terms of the free-flight model: every particle is moving toward the wall with a constant deposition-velocity, which is equal to the radial-velocity at the position where the particles start their free-flight to the wall, i.e. at a distance to the wall, y_{ff} . The deposition-velocity is thus characterised by the free-flight radial-velocity of the particles, $u_{r,p,\text{ff}}$. At $y = y_{\text{ff}}$ we have a distribution of radial velocities, and thus the number deposition rate is given by:

$$R_{\text{dep},N} = \int_0^{\infty} C u_{r,p,\text{ff}} du_{r,p,\text{ff}} \quad (3.34)$$

where C is the concentration of particles at $y = y_{\text{ff}}$ with a deposition-velocity between $u_{r,p,\text{ff}}$ and $u_{r,p,\text{ff}} + du_{r,p,\text{ff}}$. Only particles with $u_{r,p,\text{ff}} > 0$ are able to deposit.

The number deposition-rate can be estimated using the number deposition-constant $k_{\text{dep},N}$, and the total particle-concentration at $y = y_{\text{ff}}$, the free-flight concentration, C_{ff} :

$$R_{\text{dep},N} = k_{\text{dep},N} C_{\text{ff}} \quad (3.35)$$

$$C_{\text{ff}} = \int_{-\infty}^{\infty} C du_{r,p,\text{ff}} \quad (3.36)$$

In the literature some models are given relating k_{dep} with the turbulence intensity of the continuous phase, and with the Stokes-number of the particle, St_p , see, e.g., Westende et al. (2007a):

$$k_{\text{dep}} = \frac{1}{2} \sqrt{\frac{2}{\pi}} \sqrt{\langle (u'_{r,p})^2 \rangle} \quad (3.37)$$

$$\langle (u'_{r,p})^2 \rangle = \frac{1}{1 + 0.7\text{St}_p} \langle (u'_{r,g})^2 \rangle \quad (3.38)$$

It is thus assumed that the particles are in approximate equilibrium with the turbulence of the continuous phase, and that their radial-velocity is Gaussian distributed. However, the deposition velocity for large particles ($St_p \gg 1$) is expected to depend more on their injection-velocity, which may not depend on the turbulence of the continuous phase. Also, in case of horizontal flows, the gravity becomes an important parameter for the deposition of the large particles, see, e.g. Pan and Hanratty (2002), and Westende et al. (2007a).

Besides $k_{dep,N}$, we can also introduce the mass deposition constant, $k_{dep,m}$, which relates the mass deposition rate, $R_{dep,m}$, with the dispersed-phase density at $y = y_{ff}$, the free-flight density, ρ_{ff} :

$$R_{dep,m} = k_{dep,m} \rho_{ff} \quad (3.39)$$

$$R_{dep,m} = \rho_p \frac{\pi}{6} d_{30,dep}^3 R_{dep,N} \quad (3.40)$$

$$\rho_{ff} = \rho_p \frac{\pi}{6} d_{30,ff}^3 C_{ff} \quad (3.41)$$

where $d_{30,dep}$ and $d_{30,ff}$ are the volume-mean particle diameter of the depositing particles, and the particles at $y = y_{ff}$, respectively.

For a mono-dispersion we have $d_{30,dep} = d_{30,ff} = d_p$, and thus $k_{dep,m} = k_{dep,N}$. In case of a poly-dispersion this may not be true, since the deposition velocity may depend on the particle size. If we assume for now that only turbulence affects the deposition of particles, then the deposition constant for a given particle size-class decreases with increasing particle size, see eq. 3.37 and eq. 3.38. As a consequence, the small particles will deposit relatively more, hence $d_{30,dep} < d_{30,ff}$, and $k_{dep,N} > k_{dep,m}$. This shows that for a poly-dispersion it is important to distinguish between $k_{dep,N}$ and $k_{dep,m}$. Also it is not straightforward how to estimate a drop size that is representative for $k_{dep,N}$ or for $k_{dep,m}$ for a poly-dispersion, using eq. 3.37 and eq. 3.38.

3.3 Results

3.3.1 Quasi-1D approach

In fig. 3.5 we show the axial-velocity profile of the gas-phase and of the dispersed-phase for four different drop-sizes. The dispersed-phase velocity profile is computed by averaging two particle trajectories, starting at opposite positions.

We observe that the 10 μm particles follow the gas-phase velocity fairly well, and may be treated as tracers. On the other hand, the larger particles, $d_p \geq 100 \mu\text{m}$, have a slip-velocity in the center of the pipe that is much larger than the terminal slip-velocity in a stagnant medium. Close to the wall all particles are leading the gas-phase.

In fig. 3.6 we show the total pressure-gradient with varying d_p , together with its contributions, $\frac{d}{dz} p_{p,kin}$, $\frac{d}{dz} p_{p,grav}$, and $\frac{d}{dz} p_{p,diss}$ for a gas-phase velocity-profile equal to that in fig. 3.5. The dotted line corresponds to the total pressure-gradient when we use the centerline particle axial-velocity to estimate the change in particle momentum, i.e. if we take $u_{z,p,dep} = u_{z,p,c}$ as is suggested by Fore and Dukler (1995a). For all results that we show on the dispersed-phase pressure-gradient with the quasi-1D simulations we have used $R_{at,m} = 0.05 \text{ kg/m}^2\text{s}$, which gives a mass loading of 0.33 for a residence time of $t_{res} = 100 \text{ ms}$.

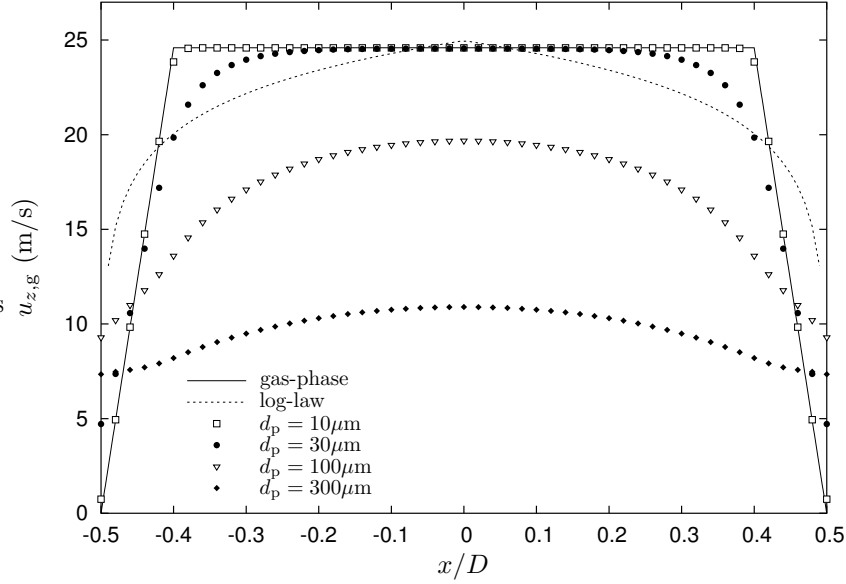


Figure 3.5: Axial-velocity profile for gas-phase and dispersed-phase with $d_p = 10 \mu\text{m}$, $30 \mu\text{m}$, $100 \mu\text{m}$ or $300 \mu\text{m}$; $\langle u_{z,g} \rangle = 20 \text{ m/s}$, $\delta_\omega/D = 0.1$, $t_\omega = 5 \text{ ms}$ and $t_{\text{res}} = 50 \text{ ms}$. The dotted line represents the log-law for a turbulent flow with an equal bulk velocity and a hydraulic roughness of $k_s/D \approx 4.6 \cdot 10^{-3}$.

As has been mentioned by Lopes and Dukler (1986), and Westende et al. (2007b), the gravitational contribution to the total pressure-gradient is small. From fig. 3.6 we observe that $\frac{d}{dz} p_{p,\text{grav}} \lesssim 0.05 \frac{d}{dz} p_{p,\text{tot}}$ for $d_p > 20 \mu\text{m}$. The value for both $\frac{d}{dz} p_{p,\text{kin}}$ and $\frac{d}{dz} p_{p,\text{diss}}$ is governed by the three relevant time-scales of the system: (i) the relaxation time of the particle, τ_p , (ii) the residence-time of the particles, t_{res} , and (iii) the vorticity time, t_ω .

Small particles

For $\tau_p \lesssim t_\omega$, the particles accelerate and decelerate fast enough to follow the gas-phase; in our case the acceleration happens only in the vorticity layer. When the particles decelerate in the vorticity layer at the end of their trajectory, they perceive a deceleration of the gas-phase axial-velocity, which has a magnitude of $a_{z,g} = -u_{z,g,c}/t_\omega$. Assuming Stokes drag, it can be easily shown that due to this ‘deceleration’, the slip-velocity of the particles reaches an asymptote $u_{z,p,s} = (a_{z,g} - g)\tau_p$, which is also the axial-velocity with which the particles deposit. Hence $\frac{d}{dz} p_{p,\text{tot}} \propto d_p^2$: a smaller droplet results in a smaller pressure-gradient, and behaves more tracer-like, as expected. In this region we have $\frac{d}{dz} p_{p,\text{kin}} \ll \frac{d}{dz} p_{p,\text{diss}}$, hence the total pressure-gradient is dominated by the dissipation of energy.

In fig. 3.7 we show $\frac{d}{dz} p_{p,\text{tot}}$, and in fig. 3.8 $\frac{d}{dz} p_{p,\text{diss}}$ with varying d_p , for different t_{res} , but with an equal vorticity time of $t_\omega = 2 \text{ ms}$. We observe a clear decrease in $\frac{d}{dz} p_{p,\text{diss}}$ for $d_p \lesssim 30 \mu\text{m}$ ($\tau_p \lesssim 2.5 \text{ ms}$), which is in essence equal for all curves, since t_ω is equal. For small d_p

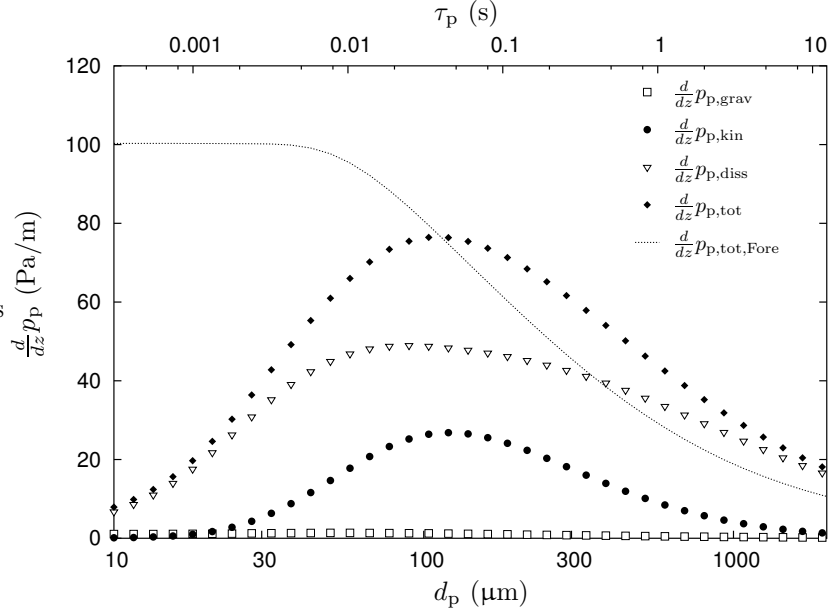


Figure 3.6: Dispersed-phase pressure-gradient, and its contributions by the change in particle kinetic and potential energy, and by the dissipation. The dotted line represents eq. 3.10 together with the assumption of Fore and Dukler (1995a) for $u_{z,p,dep} \cdot t_{res} = 50$ ms, and $t_\omega = 5$ ms.

we see a slight increase of $\frac{d}{dz}p_{p,tot}$ with increasing t_{res} , because the mass-loading increases, and thus also $\frac{d}{dz}p_{p,grav}$.

For the small particles, the method of Fore and Dukler (1995a) to calculate $\frac{d}{dz}p_{p,tot}$ does not work, since the particles are decelerating strongly in the vorticity layer prior to deposition, and thus their deposition velocity differs much from their centerline velocity.

Large particles

For $\tau_p \gg t_{res}$, the particles have an approximate constant acceleration during entrainment. Assuming Newtonian drag with a drag coefficient $C_D = 0.44$, we have: $u_{z,p,dep} \propto t_{res}/d_p$, and thus $\frac{d}{dz}p_{p,tot} \propto \alpha_p/d_p$. In this regime, a larger droplet results in a smaller pressure-gradient, for a given mass loading. Also here we have: $\frac{d}{dz}p_{p,kin} \ll \frac{d}{dz}p_{p,diss}$, so the pressure-gradient again is mainly caused by the dissipation.

In fig. 3.9 we show $\frac{d}{dz}p_{p,tot}$, and in fig. 3.10 $\frac{d}{dz}p_{p,diss}$ with varying d_p , for different t_ω , but with an equal residence-time of $t_{res} = 25$ ms. For $d_p \gtrsim 100$ μm ($\tau_p \gtrsim 30$ ms) $\frac{d}{dz}p_{p,diss}$ decreases roughly equally for all curves, since t_{res} is equal. Hence, we see a similar decrease in $\frac{d}{dz}p_{p,tot}$. For the large particles, the method of Fore and Dukler (1995a) to calculate $\frac{d}{dz}p_{p,tot}$ does not work, since the particles are accelerating throughout their entire trajectory, making their deposition velocity different from their centerline velocity. However, the mismatch is not as severe as with the small particles.

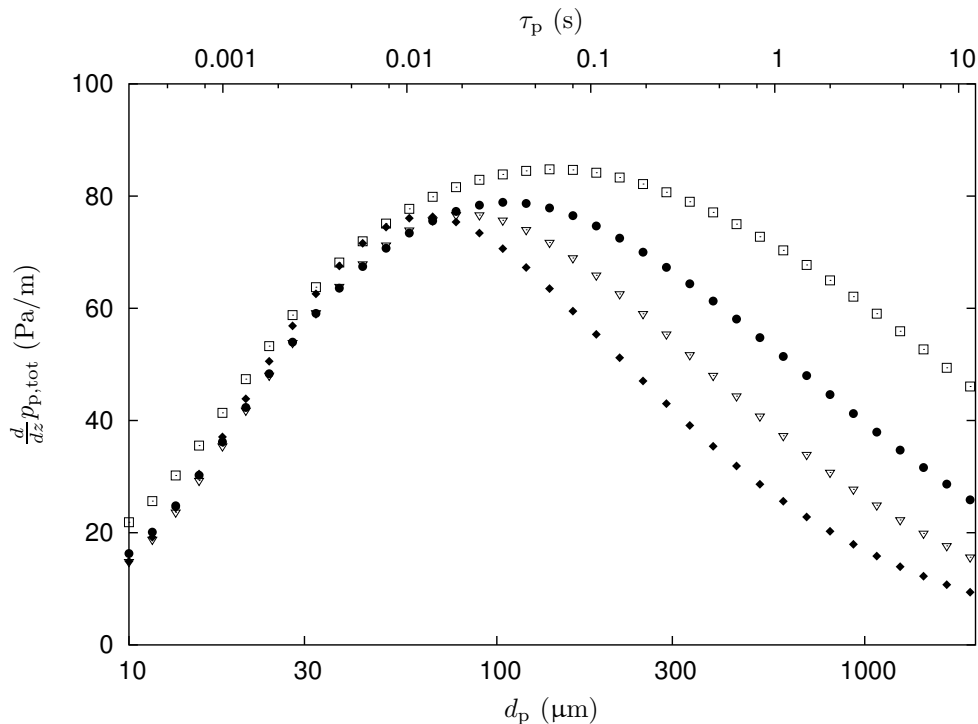


Figure 3.7: Total dispersed-phase pressure-gradient; $t_\omega = 2$ ms.

Intermediate particles

From the above we conclude that there is an intermediate particle size range with, $t_\omega < \tau_p \lesssim 10 t_{\text{res}}$, for which the total pressure-gradient for a given rate of atomisation is maximum. The relaxation time of the particles is small enough to ensure a significant increase in their momentum, whereas it is large enough to prevent the particles to lose their momentum again prior to deposition.

In fig. 3.6 we see that in this range $\frac{d}{dz} p_{p,\text{kin}}$ and $\frac{d}{dz} p_{p,\text{diss}}$ are of the same order of magnitude, and that the method of Fore and Dukler (1995a) to calculate $\frac{d}{dz} p_{p,\text{tot}}$ seems to work reasonable for this region. The dissipation contribution of the pressure gradient shows a plateau at the intermediate particle size-range, which broadens when t_ω and t_{res} differ more.

3.3.2 3D simulation

Every 3D simulation is started with an initially homogeneously distributed poly-dispersion. The poly-dispersion consists of $N_p = 800,000$ particles, and the size of each particle is determined using a Monte-Carlo technique and the injection-pdf, eq. 3.25. After 300,000 time steps ($t^+ > 10^5$) the flow was fully developed, and statistics were obtained from 50 uncorrelated fields. We have simulated four cases:

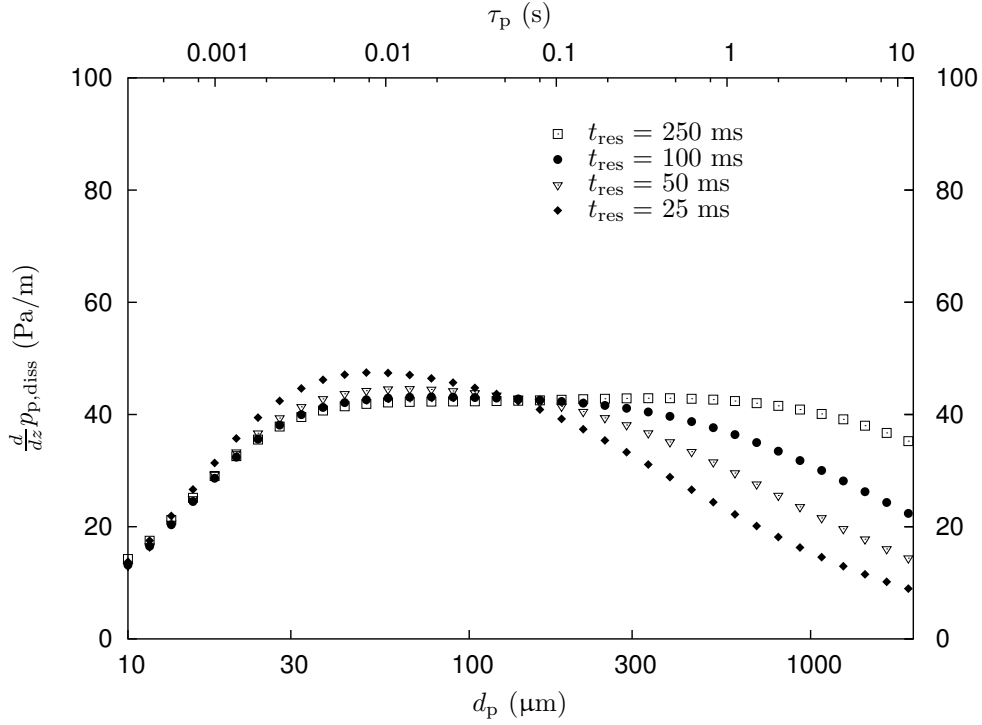


Figure 3.8: Dissipative contribution to the total dispersed-phase pressure-gradient; $t_\omega = 2$ ms.

- S1: unladen flow, $k_s/D = 0$
- S2: laden flow, two-way coupling, $k_s/D = 0$
- R1: laden flow, one-way coupling, $k_s/D = 0.01$
- R2: laden flow, two-way coupling, $k_s/D = 0.01$

In table 3.1 we show some general results of the simulations, results of the roughness-effect and the blockage effect of the particles, and some results concerning the deposition behaviour of the particles.

Gas-phase velocity

In fig. 3.11 we have plotted the mean gas-phase axial-velocity, $\langle u_{z,g} \rangle^+$, and in fig. 3.12 the gas-phase axial-velocity fluctuation, $u'_{z,g}{}^+$, for simulations S1, S2, R1 and R2. For comparison we also included the results of the experiments of a single phase pipe flow with a smooth wall of Laufer (1954) ($Re_{sg} = 38,800$), Perry and Joubert (1963) ($Re_{sg} = 75,000$), and Zagarola and Smits (1998) ($Re_{sg} = 56,700$).

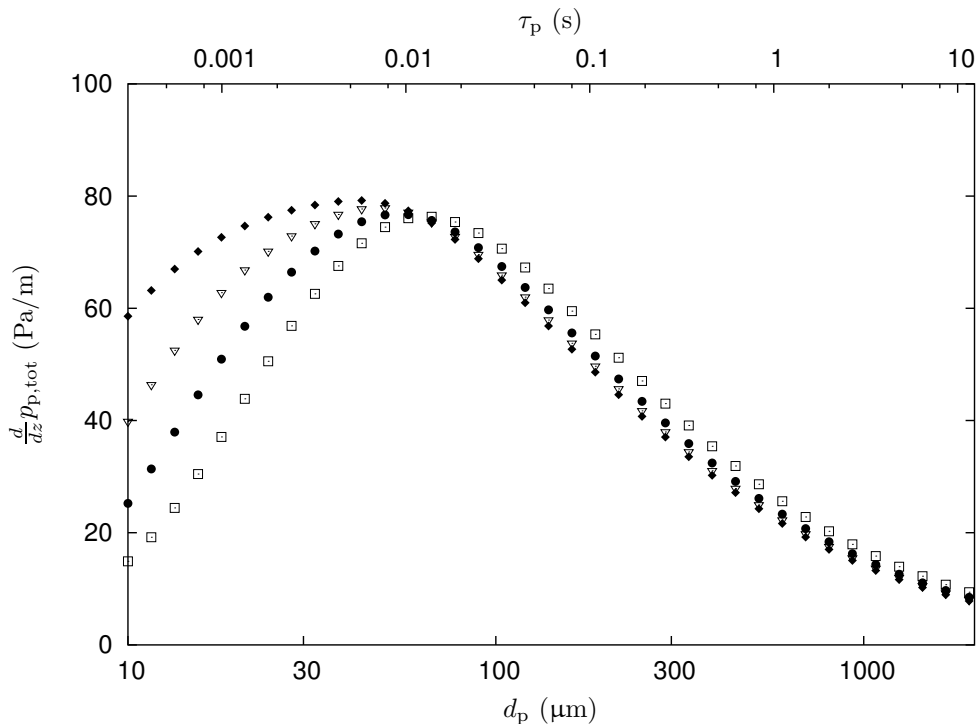


Figure 3.9: Total dispersed-phase pressure-gradient; $t_{\text{res}} = 25$ ms.

The effective friction-velocity results from fitting the log-law (eq. 3.42) to the mean axial-velocity profile:

$$\text{Log-law: } \langle u_{z,g} \rangle = u_{\tau,\text{eff}} \left[\frac{1}{\kappa} \ln(y^+) + 8.5 - \frac{1}{\kappa} \ln(k_{s,\text{eff}}^+) \right] \quad (3.42)$$

where κ is the von Karman constant, and $k_{s,\text{eff}}$ is the effective hydraulic roughness. Because we can compute the friction-velocity a priori in case of one-way coupling, we have estimated κ from simulations S1 and R1, and used this value for S2 and R2, respectively: $\kappa_{\text{S1}} = 0.42$ and $\kappa_{\text{R1}} = 0.435$.

For S1 k_s is of the order of the thickness of the viscous sublayer, which is considered to be similar to a smooth wall, see Jimenez (2004). We also observe a reasonable agreement between S1 and the experiments of Laufer, Perry and Zagarola, both for the mean and the fluctuation of the axial velocity. For R1 we see that the wall-roughness following from the fit of the log-law also matches the prescribed hydraulic wall-roughness. Using $k_{s,\text{eff}}$ with the Churchill relation, and the bulk velocity, we retrieve fairly well the effective friction-velocity for all simulations. Therefore, we have confidence that the wall-functions work satisfactorily. The results of the fit are shown in table 3.1. Note that the presence of the dispersed phase increases the total friction, and thus the $k_{s,\text{eff}}$.

The axial velocity at the wall-nearest grid-point decreases slightly (about 10%) with two-way coupling, and therefore the friction with the wall should decrease slightly as well (drag

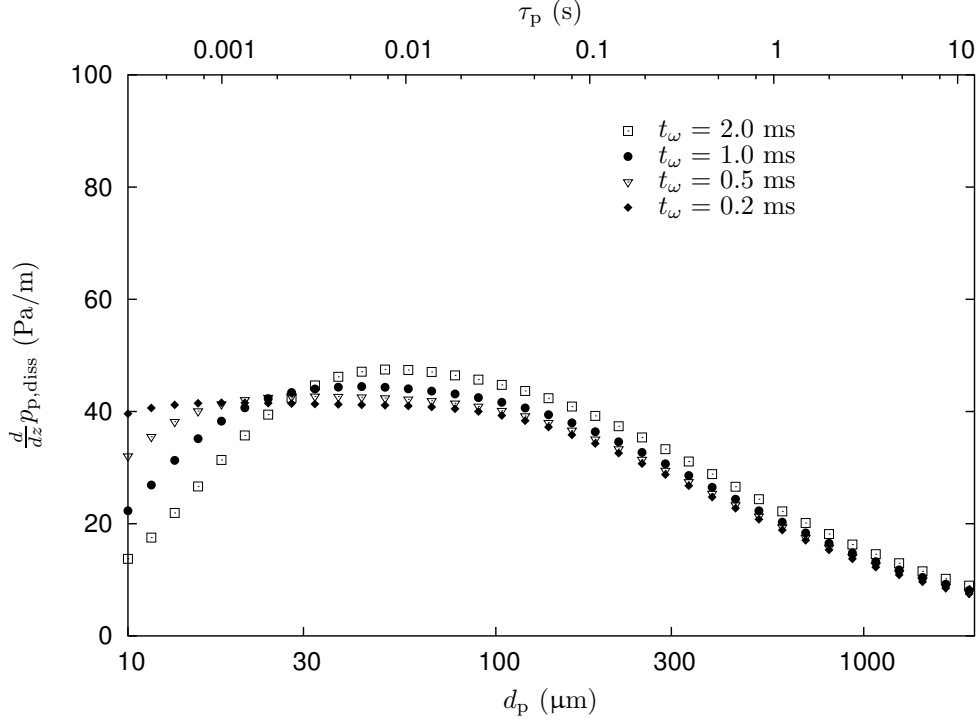


Figure 3.10: Dissipative contribution to the total dispersed-phase pressure-gradient; $t_{\text{res}} = 25$ ms.

reduction). However, the friction with the wall is prescribed in our simulations using a friction factor for unladen flows, and remains roughly constant just like the bulk velocity. As a consequence, our results have to be interpreted as if they were performed with a slightly larger wall-roughness. To our knowledge, at present there does not exist a correlation for the friction factor in a particle-laden flow, and thus we can not estimate the ‘true’ roughness of our simulations, but because the decrease of the near-wall velocity is small, so will be the ‘true’ friction with the wall. Efforts should be made to see how a particle-laden flow with two-way coupling changes the friction factor, when there is a significant particle-friction.

We see that the gas-phase velocity-fluctuation profiles in fig. 3.12 are roughly similar for all simulations, and that they match the measurements of Laufer (1954), and Perry and Joubert (1963) fairly well. In contrast to this, both the normalised radial-velocity fluctuation, $u'_{r,g}+$, and the tangential-velocity fluctuation, $u'_{\phi,g}+$ (not shown here), are about 25% smaller in the two-way coupling cases than in the one-way coupled cases, see also table 3.1. This is consistent with previous results from e.g. Li et al. (2001) and Mito and Hanratty (2006).

Using the effective friction-velocity, we can calculate ∇p_τ , and thus determine y_τ such that eq. 3.30 holds. With y_τ known, we have estimated $\alpha_{p,sc}$ with eq. 3.32, and a_{eff} using the mean particle-volume-weighted velocity, $\langle u_{z,p} \rangle$, and the mean residence time, t_{res} , in the center of the pipe and at $y = y_\tau$, i.e. $a_{\text{eff}} = \frac{\langle u_{z,p,w} \rangle - \langle u_{z,p,y_\tau} \rangle}{t_{\text{res},w} - t_{\text{res},y_\tau}}$. Using eq. 3.31 we have calculated the particle-blockage contribution to the pressure gradient, and the results are given in table 3.1.

	S1	S2	R1	R2
u_{sg} (m/s)	20	20	19	19
Re_{sg}	66700	66700	63000	63000
δ_ω/D	0.09	0.12	0.13	0.14
$\Phi_{z,p,m}$ (kg/m ² s)	0	22.7	21.0	20.6
α_p (10 ⁻⁴ m ³ /m ³)	0	13.8	14.1	13.2
d_{30} (μm)		117.7	118.4	115.9
∇p_{tot} (Pa/m)	94	220	158	285
u_∇ (m/s)	0.99	1.51	1.28	1.72
$u'_{r,g,max}$ (m/s)	1.01	0.89	1.31	1.15
$u_{\tau,eff}$ (m/s)	0.99	1.15	1.28	1.43
k_s/D	0.0004	0.0030	0.0098	0.0188
k_s^+	1.2	11.6	41.9	89.5
∇p_τ (Pa/m)	94	127	158	196
y_τ/D		0.072		0.117
a_{eff} (m/s ²)		84		113
$\alpha_{p,sc}$ (10 ⁻⁴ m ³ /m ³)		10.2		8.0
∇p_b (Pa/m)		86		91
$R_{dep,N}$ (10 ⁹ 1/m ² s)		0.227	0.336	0.259
C_{ff} (10 ⁹ 1/m ³)		1.579	1.619	1.547
$k_{dep,N}$ (m/s)		0.144	0.207	0.167
$R_{dep,m}$ (kg/m ² s)		0.108	0.164	0.122
ρ_{ff} (kg/m ³)		1.31	1.33	1.23
$k_{dep,m}$ (m/s)		0.082	0.123	0.099
$d_{30,dep}$ (μm)		96.8	97.7	96.4
$d_{30,ff}$ (μm)		116.5	116.3	115.0
$\langle t_{res} \rangle$ (ms)		152	107	135

Table 3.1: General results for simulations S1, S2, R1 and R2. $\Phi_{z,p,m}$ is the dispersed-phase axial mass-flux, and d_{30} is the overall volume-mean diameter of the particles. $u'_{r,g,max}$ is the maximum value of the gas-phase radial-velocity fluctuation. The mean residence time, $\langle t_{res} \rangle$ is estimated with eq. 3.11, and $R_{at,m} = R_{dep,m}$.

The sum of ∇p_τ and ∇p_b matches ∇p_{tot} within about 3%.

Since the dispersed phase contributes to the pressure gradient via both the roughness effect, and the blockage effect of the particles, we have $u_\tau < u_{\tau,eff} < u_\nabla$. Note that u_τ is determined with the prescribed wall-roughness, see section 3.2.2.

Since the effects of the dispersion are similar for simulations S2, R1 and R2, in the following we only show the detailed results of S2.

Dispersed-phase velocity

In fig. 3.13 we have plotted the mean dispersed-phase axial-velocity profile, and in fig. 3.14 the axial-velocity fluctuation, both for simulation S2. The solid lines represent the results of the gas phase and the symbols those of the dispersed phase; three particle size-classes are shown:

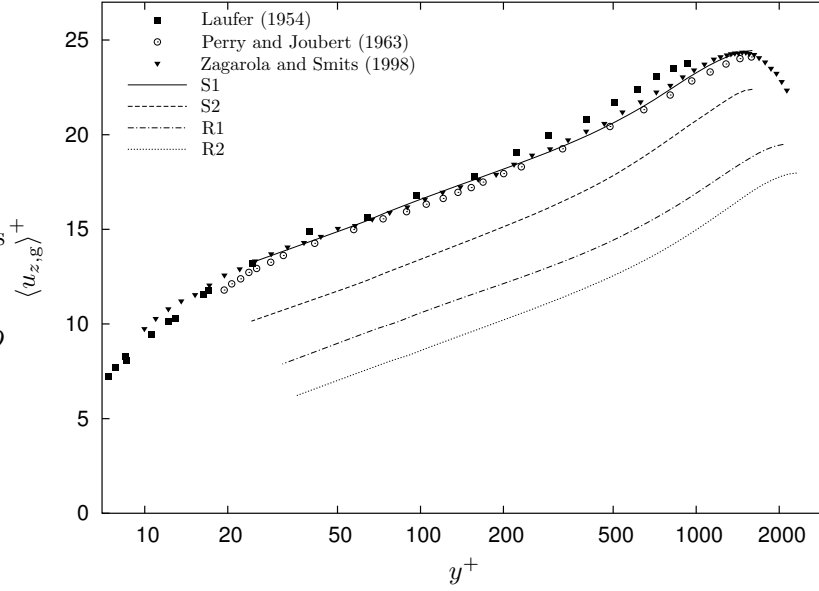


Figure 3.11: Mean axial-velocity profile in wall-units of the simulations S1, S2, R1 and R2, and of the experiments of Laufer, Perry and Joubert, and Zagarola and Smits.

(i) small particles: $10 \mu\text{m} < d_p < 20 \mu\text{m}$, $0.07 \lesssim \text{St}_p \lesssim 0.28$, (ii) intermediate particles: $50 \mu\text{m} < d_p < 100 \mu\text{m}$, $1.8 \lesssim \text{St}_p \lesssim 7.1$, and (iii) large particles: $200 \mu\text{m} < d_p < 500 \mu\text{m}$, $28 \lesssim \text{St}_p \lesssim 177$. Here the Stokes numbers, St_p , are based on the Stokes relaxation-time and the time scale of the large-scale turbulence, \mathcal{T} . Since the average injection velocity is of the order of the friction velocity, we have $\mathcal{T} \approx t_\omega \approx \frac{1}{10} t_{\text{res}}$, and hence St_p can be used to classify whether a particle is small, intermediate or large, see also section 3.3.1. For the intermediate particles the Stokes number is in the range: $1 \lesssim \text{St}_p \lesssim 10$.

For the small, the intermediate and the large particles we find an average centerline slip-velocity of 0.06 m/s, 1.2 m/s and 5 m/s, respectively. For $y/D \gtrsim 0.15$ ($y^+ \gtrsim 580$) the slip velocity is roughly constant in the pipe cross-section. When we calculate the free-fall velocity, taking into account the drops-size-pdf at injection (i.e. eq. 3.25), we find for the small and the intermediate particles a value that is about 8 times smaller, and for the large particles a value that is about 2.5 times smaller.

It is interesting to observe an approximate log-law behaviour for the particles, similar to the gas-phase: increasing the particle size decreases the slope of the mean axial-velocity profile. This seems as if the effective friction-velocity of the particles decreases with increasing particle size, and it is linked to the interaction between the gas-phase turbulence and the particles, which becomes weaker with increasing particle Stokes number. Since, for the small particles, the slip-velocity is much smaller than the gas-phase velocity fluctuations, and because their Stokes number is much smaller than 1, it follows that their dynamical behaviour is dominated by the interactions with the gas-phase turbulence. With a similar reasoning we conclude that the large particles are driven by the interactions with the gas-phase mean flow, and the

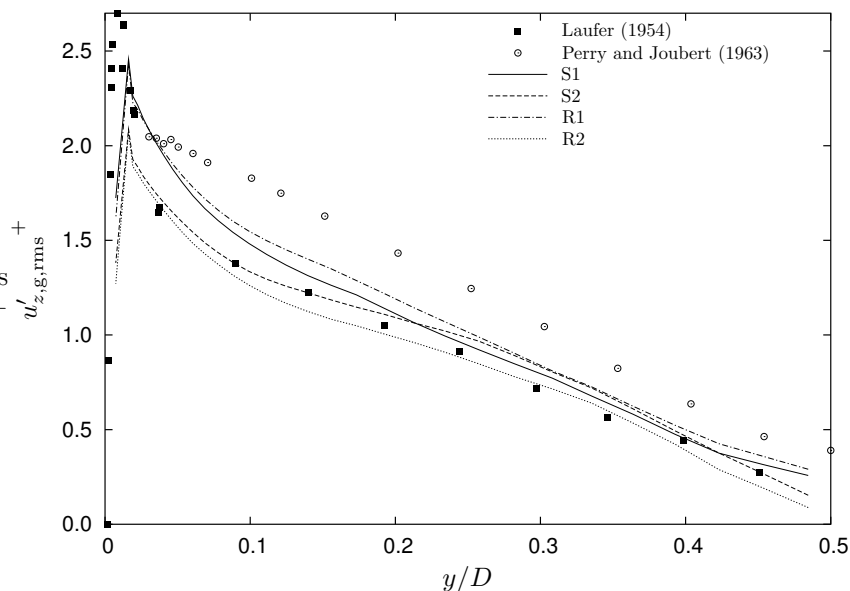


Figure 3.12: Axial-velocity fluctuation in wall-units of the simulations S1, S2, R1 and R2, and of the experiments of Laufer, and Perry and Joubert.

intermediate particles by both the mean flow and the turbulence. For the small particles we also observe that the axial velocity-fluctuations are close to that of the gas-phase, making them suitable tracers for estimating the axial-velocity, which was also assumed by Westende et al. (2007b). For the large particles the axial-velocity fluctuation is much larger; they are not expected to be related to the interactions with the turbulence, but with the spread in lifetime (due to the spread in the injection-velocity) in combination with a strong acceleration, as is also pointed out by Westende et al. (2007b). The axial-velocity fluctuations of the intermediate particles are very large near the wall, but in the center of the pipe they approach the value of the gas-phase.

The radial and the tangential velocity-fluctuations of the particles, which are not shown here, are smaller than that of the gas-phase for all particle size-classes, especially near the wall. The radial and tangential velocity-fluctuations are about 25% smaller for the small particles, and about 65% smaller for the intermediate and large particles.

Concentration and deposition

In fig. 3.15 the particle-concentration profile for the small, the intermediate, and the large particles are shown. For the small particles the near-wall concentration is only about a factor of 10 larger than the concentration in the center of the pipe, which is caused by the implementation of the absorbing walls. When reflective walls would have been implemented, the near-wall concentration would be much larger, e.g. Boelens and Portela (2006) found for particles with $\tau_p^+ = 100$ that this factor is about 10^4 with reflective walls, whereas they found

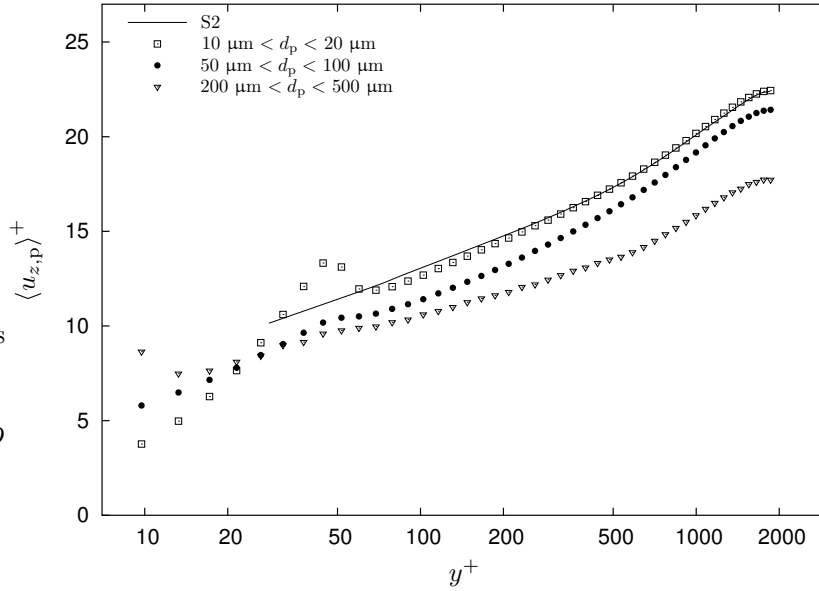


Figure 3.13: Mean dispersed-phase axial-velocity of simulation S2 for three particle size-classes. The solid line represent the result of the gas-phase.

it to be about 1 with absorbing walls. For the intermediate particles, the near-wall concentration is about 3 times larger than the centerline concentration, and for the large particles they are almost equal.

The overall concentration of the small particles is smaller than would be expected from the pdf at injection, eq. 3.25. As a consequence the concentration of the large particles is relatively large, e.g. for $200 \mu\text{m} < d_p < 500 \mu\text{m}$ the average concentration is about twice as large as expected. Most likely, this is caused by the turbophoresis effect, pushing the small particles towards the wall, where they deposit and are replaced by ‘new’ particles according to the injection-pdf, hence they are, on average, larger. This can be seen more clearly in fig. 3.16, where we show the pdf of several regions in the pipe. For $r/D < 0.4$ the pdf are similar, but in the near-wall region we see a relative increase of the small, and the intermediate particles. This was also found in measurements by Westende et al. (2007b), although the details of their pdf at small drop-sizes differ from the results of our LES, hence there is still a need to better model the injection-pdf.

For $d_p > 200 \mu\text{m}$, the pdf is equal throughout the whole pipe cross-section, and matches the injection-pdf, which is expected when particles traverse the pipe ballistically.

In table 3.1 we show the results on the number deposition-rate and the mass deposition-rate. The free-flight concentration and the free-flight density is computed by averaging in a region $0.035 < y/D < 0.065$, i.e. similarly as Westende et al. (2007a) computed their free-flight concentration. From table 3.1, comparing the results of R1 and R2, we observe that $k_{\text{dep},N}$ decreases with 19% when two-way coupling is implemented. This is mainly caused by

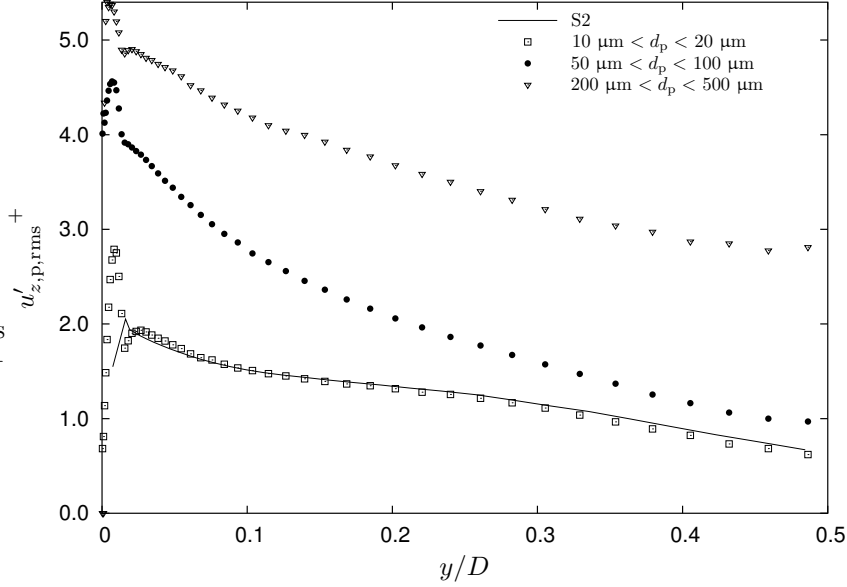


Figure 3.14: Dispersed-phase axial-velocity fluctuation of simulation S2 for three particle size-classes. The solid line represent the result of the gas-phase.

the decrease of $u'_{r,g}$, for which a decrease of about 12% is seen for $u'_{r,g,max}$. Possibly, the simultaneous increase of $u_{\tau,eff}$ will result in a decrease of the time scales of the turbulence, and thus an increase of St_p . Both a decrease of $u'_{r,g}$ and an increase of St_p result in a decrease of $k_{dep,N}$, see eq. 3.37 and eq. 3.38. Mito and Hanratty (2006) also observed a decrease in particle deposition constant, although the effect of the feedback is stronger in their simulations, e.g. they find a decrease in $k_{dep,N}$ of 50% at a dispersed phase holdup $\alpha_p = 5 \cdot 10^{-4}$, whereas we find a decrease of about 25% at a dispersed phase holdup $\alpha_p = 13 \cdot 10^{-4}$ (i.e. comparing $k_{dep,N}$ of simulation R1 and R2). Note that Mito and Hanratty used a mono-dispersion, and thus $k_{dep,N} = k_{dep,m}$.

We also observe that $k_{dep,m}$ is about 40% smaller than $k_{dep,N}$, because the smaller particles have a larger deposition constant, and thus $d_{30,dep} < d_{30,ff}$. In fig. 3.17 we show the deposition constant as a function of the particle size, together with the model given by eq. 3.37 and eq. 3.38; we have used $u'_{r,g,max}$ as an estimate for $u'_{r,g,rms}$, and $\mathcal{T} = 0.046D/u_{\tau,eff}$ to calculate $St_p = \tau_p/\mathcal{T}$, see also Lee et al. (1989). In fig. 3.18 the stopping distance of the particles normalised with the pipe diameter is shown; the stopping distance is computed by the product of the deposition constant and the particle relaxation-time.

When the stopping distance is larger than the pipe radius (dashed line in fig. 3.18) the free-flight model does not hold anymore, because the particles do not reach an approximate equilibrium with the turbulence of the gas-phase. For these large particles the deposition is mainly determined by their injection velocity. In our simulations the injection velocity is equally distributed for all particle sizes, and thus the deposition constant is approximately equal for the particles with $d_p \gtrsim 300 \mu\text{m}$.

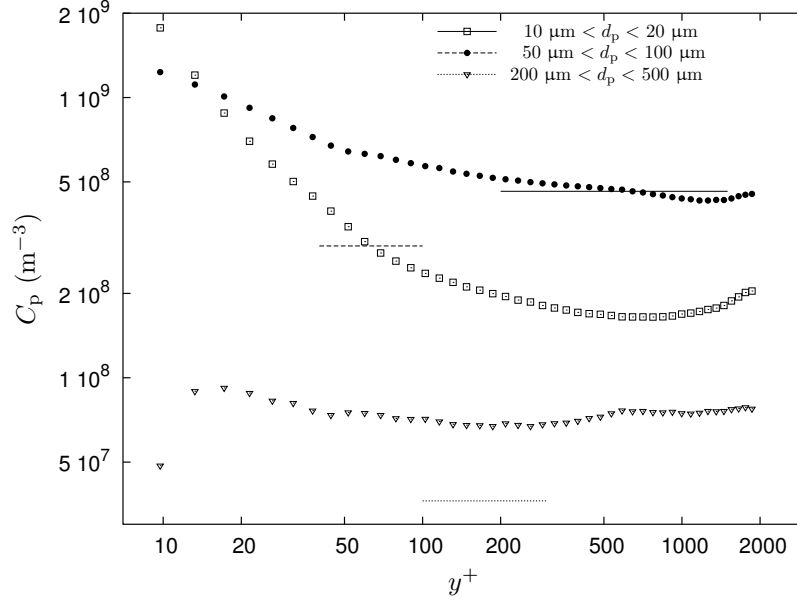


Figure 3.15: Concentration profile of the small, the intermediate, and the large particles. The horizontal lines represent the concentration that is expected from the injection-pdf; small particles: solid line, intermediate particles: dashed line, and large particles: dotted line.

Also, the deposition of very small particles is unlike a free-flight, since their stopping distance is smaller than the viscous layer, and they will ‘feel’ the turbulence of the gas-phase close to the wall. The smaller the particles are, the more they behave as tracers, which can not deposit because of the impermeability of the wall for the gas-phase, hence their deposition constant is smaller. Note that in our case we are using wall-functions, hence we do not resolve the turbulence close to the wall; we use the distance to the wall of the wall-nearest grid-point as a lower limit of the stopping distance, instead, corresponding to $d_p \lesssim 40 \mu\text{m}$.

Therefore, there exists an upper and a lower limit on the stopping distance (i.e. on the particle size) for the validity of the free-flight model, see also Lee et al. (1989). When the particle-size distribution consists of many particles that are outside these limits, the free-flight model can not be used to predict the overall deposition. We see that for $40 \mu\text{m} \lesssim d_p \lesssim 300 \mu\text{m}$ the free-flight model (eq. 3.37, solid line in fig. 3.17) predicts the deposition constant rather well. From our results it seems that the arithmetic-mean diameter of a poly-dispersion should be used to estimate $k_{\text{dep},N}$, and the volume-mean diameter to estimate $k_{\text{dep},m}$.

Dispersed-phase residence time

In fig. 3.19 we have plotted the residence time of the particles in the flow, calculated either directly from the depositing particles, $t_{\text{res},\text{dir}}$, or indirectly, $t_{\text{res},\text{indir}}$, using eqs. 3.10 and 3.11:

$$t_{\text{res},\text{indir}} = \rho_p \alpha_p u_{z,p,\text{dep}} / \frac{d}{dz} \rho_{p,\text{tot}} \quad (3.43)$$

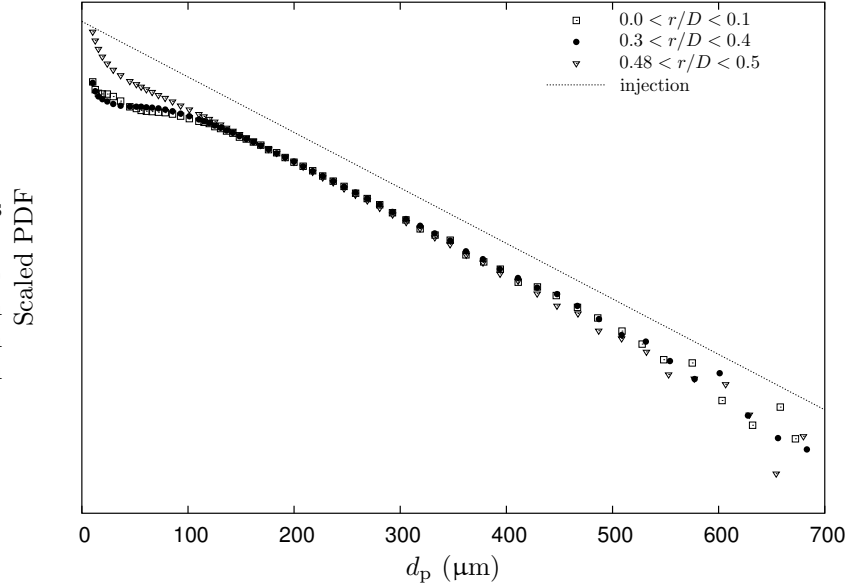


Figure 3.16: Pdf of particle in the center region, $r/D < 0.1$, the ‘log-law’ region, $0.3 < r/D < 0.4$, and the near-wall region, $0.48 < r/D < 0.5$.

where we have neglected gravity, and assumed $u_{z,p,at} \ll u_{z,p,dep}$. Also the results of the experiments performed by Westende et al. (2007b) are shown in fig. 3.19. They used eq. 3.43 to calculate the residence time from centerline data only. For computing the dispersed-phase pressure-gradient they summed the pressure-gradient contributions of all individual measured droplets, and thus they needed the centerline gas-velocity, which they estimated using ‘tracer’-droplets: droplets in the size range of $10 \mu\text{m}$ to $20 \mu\text{m}$.

From fig. 3.19 we observe that for $d_p \gtrsim 15 \mu\text{m}$ $t_{res,indir}$ agrees fairly well with $t_{res,dir}$. However, for $d_p \lesssim 15 \mu\text{m}$, the estimation with the indirect method, eq. 3.43, results in too large values. For these small particles the pressure-gradient contribution is essentially zero, since they behave approximately like tracers, and because of this, the indirect method for determining the residence time, becomes unreliable for very small particles. Also the assumption that $u_{z,p,at}$ can be neglected does not hold anymore, and for $d_p \lesssim 15 \mu\text{m}$ the deposition velocity is even smaller than the injection velocity.

The average residence time shown in fig. 3.19 seems to be rather large, however, since we have used eq. 3.11, $\langle t_{res} \rangle$ is essentially a mass-weighted average residence-time. The peak of the volume-distribution of the particles is for $d_p \approx 200 \mu\text{m}$ (see also fig. 3.20), hence we expect $\langle t_{res} \rangle \approx t_{res,dir,d_p=200\mu\text{m}}$.

The measurements of Westende et al. show qualitatively the same behaviour as the results of our LES with a minimum residence time for the intermediate particles. Their estimate of the residence time increases very strongly for $d_p \lesssim 40 \mu\text{m}$, since they have used the ‘tracer’-droplets for estimating the centerline gas-velocity. Therefore these droplets themselves have a zero slip-velocity, i.e. a zero pressure-gradient, resulting in a too large value of their residence

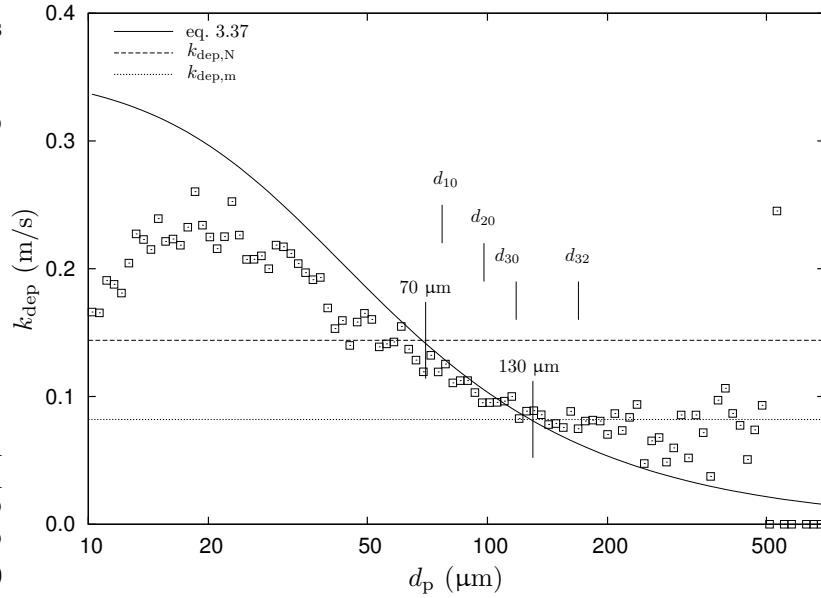


Figure 3.17: Deposition constant as a function of the particle size of simulation S2 (symbols). The solid line represents the model given by eq. 3.37 and eq. 3.38, and the dashed and the dotted line stand for $k_{\text{dep},N}$ and $k_{\text{dep},m}$, respectively. The mean-diameters: d_{10} , d_{20} , d_{30} , and d_{32} , of the whole dispersed-phase are indicated as well.

time.

Also, because they based their residence time estimation purely on centerline data, i.e. they assumed $u_{z,p,\text{dep}} \approx \langle u_{z,p,c} \rangle$, the deposition velocity and thus the residence time is overestimated. Using the injection-pdf, eq. 3.25, the injection velocity is probably underestimated, when compared with a real annular flow, see also appendix B; as a consequence, the residence times will be larger. This latter effect reduces somewhat the deviation between the experiments of Westende et al. (2007b) and the results of our LES.

Here we note that, the minimum of the residence-time for the particles with $20 \mu\text{m} < d_p < 50 \mu\text{m}$, is linked to the deviation of the pdf from the injection-pdf at these particle sizes, see fig. 3.16. The turbophoresis effect probably is responsible for an enhanced transport of these particles to the wall, where they deposit.

Dispersed-phase pressure-gradient

In fig. 3.21 the total average acceleration together with its contributions by the dissipation, and the change in kinetic and gravitational energy are shown. Also the result from the experiment of Westende et al. (2007b) is plotted in this graph. We observe that qualitatively the results from the LES agree with the experiments of Westende et al., showing a maximum acceleration of the intermediate particles. Particles with a relaxation time smaller than the time scale of the large-scale turbulence behave like tracers, and they deposit with a small

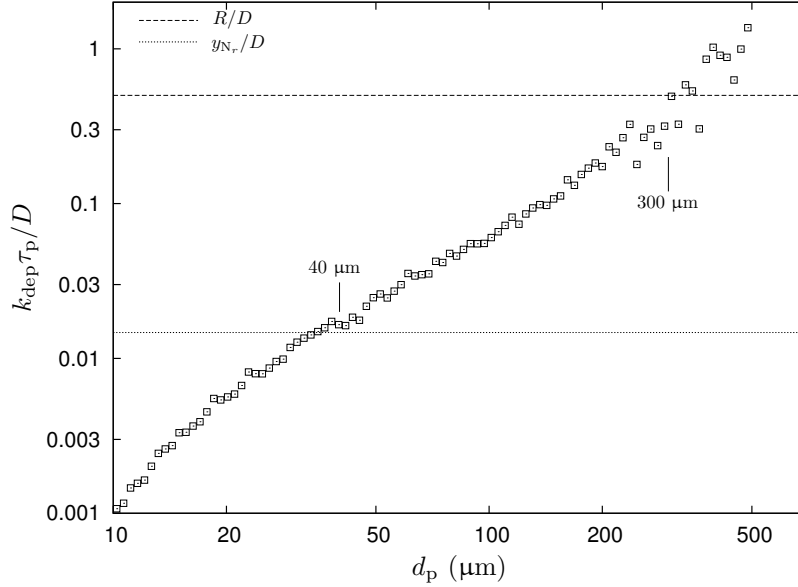


Figure 3.18: Stopping distance of the particles normalised with the pipe diameter (symbols). The dashed, and the dotted line represent the pipe-radius, and the distance to the wall of the wall-nearest grid-point, respectively.

velocity, making their overall acceleration small. Particles with a relaxation time much larger than the residence time accelerate slow, because of their inertia.

Here we also note that, since there is a spectrum of time-scales for the turbulence and the residence time, we do not find a plateau for the intermediate-sized particles, as we have found in the quasi-1D simulation. Also, since the residence time seems to increase with increasing particle size for d_p , the range of intermediate particles is extended in the LES. For the results of the annular flow the residence time is more constant with droplet size than in the simulations, making the distinction between the intermediate and the large particles more ‘sharp’, and hence the slope of the acceleration curve more steep. Again, since in the measurements the centerline velocity is used instead of the deposition velocity for estimating the overall acceleration, the acceleration is much larger than for the LES.

Since the acceleration does not change strongly for $d_p \gtrsim 40 \mu\text{m}$, the most important parameter for determining the pressure-gradient is α_p . This is also the reason why the pdf of the holdup and that of the pressure-gradient are approximately equal, see fig. 3.20. As a first guess we can take $a_p \approx \langle u_{z,g} \rangle / t_{\text{res}}$, and we have:

$$\frac{d}{dz} p_{p,\text{tot}} \propto \alpha_p a_p \propto R_{\text{at,m}} \langle u_{z,g} \rangle \quad (3.44)$$

Also the LES result on the dispersed-phase pressure-gradient show that the gravitational contribution to the total pressure-gradient is negligible. This suggests that for the dynamics of the particles, once they are injected, the orientation of the flow is irrelevant. Note that

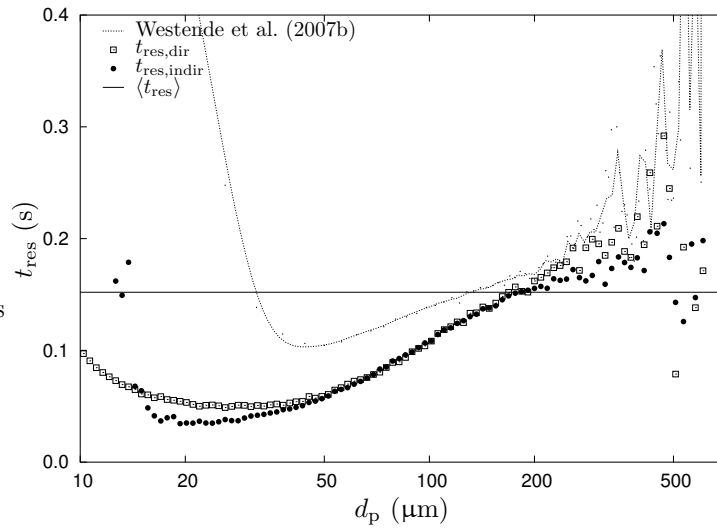


Figure 3.19: Residence time of particles, calculated directly, $t_{res,dir}$, or indirectly, $t_{res,indir}$. For comparison the results of Westende et al. (2007b) (G21L2) are shown as well: the dotted line shows the trend of the data-points (small solid symbols). The solid line is the average residence time estimated with eq. 3.11.

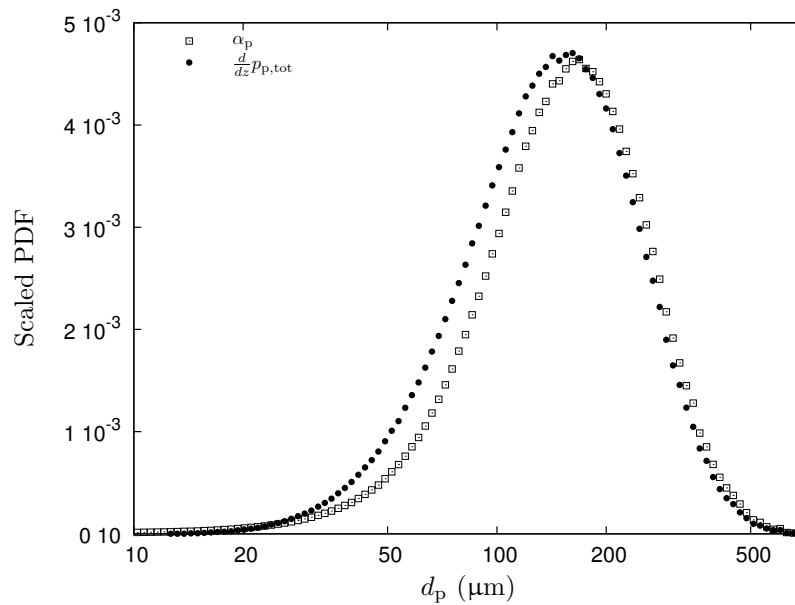


Figure 3.20: Pdf of α_p and of $\frac{d}{dz} p_{p,tot}$ contribution.

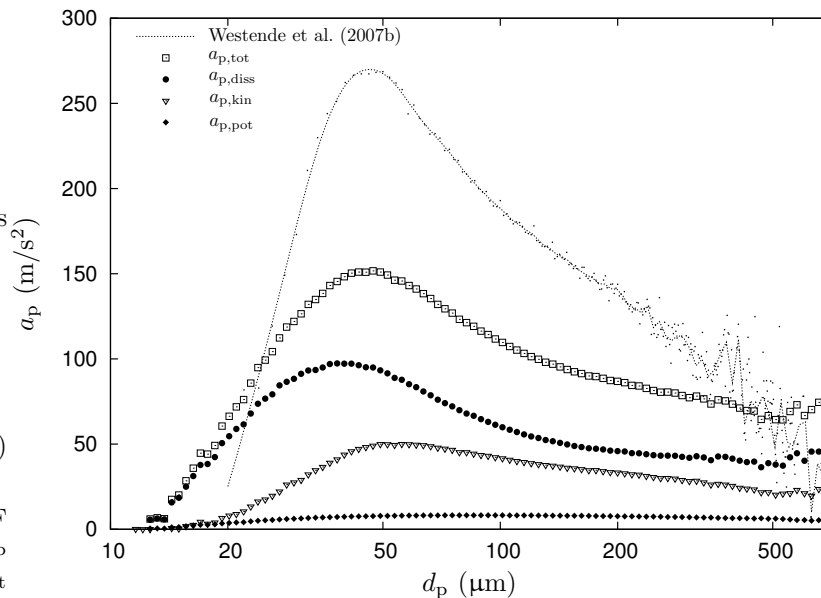


Figure 3.21: Effective acceleration of particles, $a_p = u_{z,p,dep}/t_{res}$, entrained in the gas-flow, together with their contribution by the dissipation, change in kinetic energy, and change in potential energy. The results of Westende et al. (2007b) (G21L2) are shown for comparison.

this only holds, when the particles are injected with a low velocity, i.e. when they accelerate strongly. The contribution by the dissipation and the change in kinetic energy are of the same order, for the intermediate and the large particles, but for the small particles the dissipation contribution determines the total pressure-gradient.

3.4 Conclusion

We have performed two types of simulations, representing an upward air flow of about 20 m/s in a pipe with $D = 5$ cm. One of them, a quasi-1D approach, has a prescribed mean flow, and the other is a 3D-LES including two-way coupling, such that the dispersion can affect the dynamics of the gas-phase. Wall-functions are applied in the 3D-LES to resolve high Reynolds number flows, with the additional option to implement wall-roughness.

From the quasi-1D simulation the important time-scales are deduced: the vorticity time, the residence time of the particles and their relaxation time. The value of the vorticity time with respect to the particle relaxation time determines when a particle can be considered small, and, similarly, the value of the residence time of the particles determines when a particle should be considered large. Both small and large particles have only a mild effect on the pressure-gradient for a given value of the atomisation mass-flux. The intermediate-sized particles are most effective in extracting energy from the system: they are small enough to accelerate vigorously, but inert enough not to lose their momentum prior to deposition. The

most important contribution to the dispersed-phase pressure-gradient is due to the dissipation of energy. Only for the intermediate particles the contribution related to the change of kinetic energy becomes of the order of the dissipative contribution. For particles that are injected with an initially small axial-velocity, the contribution to the pressure-gradient due to the change in gravitational energy is negligible.

The 3D LES shows that a particle-laden flow, when compared to an unladen flow, should be modeled by an increase in the the total shear, combined with an extra mean pressure-gradient due to the blockage effect of the particles in the core of the flow. Although the total friction increases, the wall friction may decrease with constant bulk-velocity. Particles with a relaxation time that is about equal to the time scale of the large-scale turbulence are most effective in extracting energy from the continuous phase, and have the strongest acceleration. The magnitude of the acceleration and of the holdup of the particles are the key parameters in determining the dispersed-phase pressure-gradient.

4. Effect of the dispersed phase on the secondary flow

4.1 Introduction

In the exploitation of gas-wells, liquid (water, oils, condensates) is usually produced simultaneously. The flow pattern inside the production tubing is an annular dispersed two-phase flow: the liquid phase flows partly as a wavy film along the pipe circumference, and partly as entrained droplets in the turbulent gas core.

Until the 1970s most wells were vertical, but modern technologies allowed for strongly deviated wells, resulting in an inclined annular dispersed flow. When deviating a vertical annular dispersed pipe flow, its axi-symmetry is lost: the liquid film at the bottom becomes thicker, and also the droplet concentration is highest in the bottom region. As a consequence, the liquid film at the bottom of the pipe is more rough than at the top of the pipe, and this variation of roughness results in the presence of a secondary flow: a mean flow in the cross-section of the pipe, usually manifested as multiple counter-rotating vortical cells.

Darling and McManus (1968) performed single phase experiments in a pipe with varying wall-roughness, mimicking the variation of the film-thickness in a horizontal annular flow. They measured the secondary flow, which consisted of two counter-rotating cells moving downward through the center and upward along the pipe wall. Later research, by e.g. Dykhno et al. (1994), and Flores et al. (1995), showed the existence of a secondary flow in a horizontal annular flow, deduced from the axial-velocity profiles. However, Dykhno et al. also found the secondary flow to change direction with increasing liquid flow rate. According to them this is caused by the effect of enhanced droplet entrainment and corner effects of the liquid film. In order to explore further the change of secondary flow by an asymmetric droplet distribution, Belt et al. (2004) performed simulations of a single-phase flow with beads at fixed positions in the lower part of the pipe cross-section, thus creating a 'droplet'-driven secondary-flow. Their simulations were qualitatively confirmed by Daalmans (2005), who conducted experiments on a comparable system. Both works show a secondary flow with a direction opposite to that found by Darling and McManus, indicating that the droplet entrainment in annular flow could change the direction of the secondary flow as suggested by Dykhno et al. (1994). However, the beads are fixed, which is not realistic for an actual annular flow in which the droplets move freely around, and in which the feedback force is related to the acceleration

of the droplets. Also, the Reynolds number in the simulations of Belt et al. (2004) is rather small for an annular flow.

In order, to better understand how the dispersed phase of an actual annular flow can alter the secondary flow, we present here results of large eddy simulations (LES) that are more realistic for an annular flow, and compare these with the experiments of Dykhno et al. (1994), and with experiments performed in a horizontal air-water annular flow using Phase Doppler Anemometry (PDA). Results of the gas-phase mean axial-velocity, its in-plane velocity, and of the dispersed-phase concentration and its deposition are shown and discussed. We find that our results support the suggestion of Dykhno et al. (1994) and the analysis of Belt et al. (2004), that the feedback force of the droplets can change the secondary flow pattern.

In section 4.2, we formulate the problem and detail the major mechanisms involved. The models used in the numerical simulation of the particle-laden turbulent pipe flow are described in section 4.3. The results of the simulations, and of the experiments are shown in section 4.4, and concluding remarks are given in section 4.5.

4.2 Problem formulation

A horizontal annular flow is simulated by means of a high Reynolds-number LES in a cylindrical geometry. Instead of simulating the liquid film, in this paper we consider a simplified situation: the gas-liquid interface is represented by a circular wall with a varying roughness, see fig. 4.1. The variation of wall-roughness induces a secondary flow pattern as shown in chapter 3.

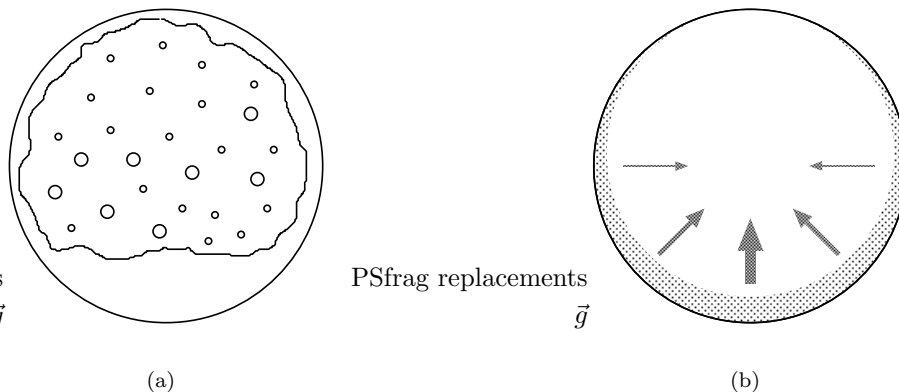


Figure 4.1: a) Schematic representation of the cross-section of a horizontal annular-dispersed flow. b) In the idealised situation the wall-roughness and the rate of atomisation decrease monotonically along the pipe circumference from the bottom wall to the top wall of the pipe. The value of the hydraulic wall-roughness is represented by the width of the textured band, and the strength of the atomisation rate is depicted by the linewidth of the arrows.

The droplets are considered as small solid spheres, and are driven by drag and gravity only, which are the most important driving mechanisms in the actual situation. We have explicitly

controlled the atomisation process, by injecting particles into the flow with initial properties according to a prescribed injection-pdf, and combined this with perfectly absorbing walls; the total number of particles in the domain is kept constant during the simulation. The rate of atomisation is assumed to be linear with the prescribed hydraulic roughness: both are maximum at the bottom wall and minimum at the top wall of the pipe, see fig. 4.1. The feedback force of the particles onto the gas-phase (two-way coupling) is implemented via the point-force method; inter-particle collisions are not considered. The mass loading (the total mass of the particles divided by the mass of the gas) is increased from about 0.06 to about 0.7 in order to study the changes in the secondary flow.

In general, the strength of a secondary flow is very small: on the order of a few percent of the axial velocity. As a consequence, it is very difficult to directly measure the vortical cells of a secondary flow. To our knowledge, only Darling and McManus (1968), Flores et al. (1995), and Daalmans (2005) present results of the directly measured secondary flow, and of these authors only Flores et al. performed two-phase experiments. Their flow conditions were in the stratified-annular flow-regime with a small amount of entrainment, and thus are best compared with the single-phase experiments of Darling and McManus in a pipe with variable wall-roughness. Other studies usually identify a secondary flow by the change in the mean axial-velocity profile, e.g. Dykhno et al. (1994) and Williams et al. (1996). However, the combination of a variable wall-roughness and a non-uniform dispersed-phase concentration can make the secondary flow fairly complex, and there is no longer a direct connection between the secondary flow pattern and the mean axial-velocity profile, as explained by Belt et al. (2004) and confirmed by our results containing both the mean axial-velocity profiles and the secondary flow patterns for the simulations.

According to Westende et al. (2007a) (chapter 3), the presence of a secondary flow can have strong effects on particle deposition. They show that the secondary flow can reduce the gravitational settling, and locally enhance the deposition. However, they have used one-way coupling, and here we have implemented two-way coupling; the spatial distribution of the particles in the cross-section of the pipe and the secondary-flow pattern mutually affect each other, and thus also the particle deposition behaviour.

All the simulations were done for an air-water system in a horizontal pipe with a diameter $D = 5$ cm. In every computation, the superficial gas-velocity, u_{sg} , was set to about 20 m/s, corresponding to a superficial gas-Reynolds number $Re_{sg} \approx 67,000$; the density is $\rho_g = 1.2$ kg/m³, and the kinematic viscosity is $\nu_g = 1.5 \cdot 10^{-5}$ m²/s. The direction of the gravity is in negative ℓ -direction, perpendicular to the mean gas-flow for all simulations, with $|\vec{g}| = 9.8$ m/s², see fig. 4.2. The particles, with a density $\rho_p = 1000$ kg/m³, are injected according to a prescribed injection-PDF deduced from experiments performed with a PDA in the center of the pipe of a vertical annular air-water flow. In this way, we have injected particles with diameters ranging from 1 μ m to 700 μ m.

4.3 Simulations

In the 3D-simulation we use an Eulerian-Lagrangian LES with the standard point-particle approach, see also Westende et al. (2007a) (chapter 3). In fig. 4.2, the computational domain with the corresponding position and velocity coordinates for the axial, tangential, and radial directions is shown.

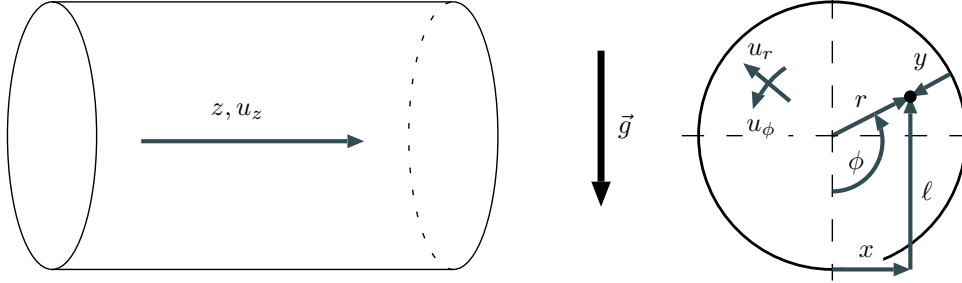


Figure 4.2: Computational domain, together with position and velocity coordinates. The gravity is directed downward.

The wall boundary-condition, i.e. the variation of wall-roughness, is implemented using the Schumann wall-function as described by Westende et al. (2007a) (chapter 3), with the hydraulic wall-roughness varying according to:

$$\frac{k_s}{D} = 0.015(\cos(\phi) + 1) \quad (4.1)$$

The particles are treated as point-particles and are tracked individually using non-linear drag and gravity, see Westende et al. (2007a) (chapter 3).

When a particle hits the wall it is removed from the flow, hence mimicking the deposition process. At the same moment, a new particle is injected into the flow according to an injection-pdf using a Monte-Carlo technique. In this way we maintain an equal number of particles inside the pipe. The injection-pdf represents the atomisation, and results partly from a fit to experimental data of a vertical upward air-water annular-dispersed pipe-flow, see chapter 3 and appendix B:

$$\text{PDF} = \text{PDF}_d \text{PDF}_u \text{PDF}_\phi \quad (4.2)$$

$$\text{PDF}_{d_p} = \begin{cases} 0.0204 \exp(-C_d d_p) & 1 \mu\text{m} < d_p < 700 \mu\text{m} \\ 0 & \text{else} \end{cases} \quad (4.3)$$

$$\text{PDF}_u = \begin{cases} 1.064 \exp(-C_u u_{\text{lat},p}^{1.2}) & 0 < u_{\text{lat},p} < 5 \text{ m/s} \\ 0 & \text{else} \end{cases} \quad (4.4)$$

$$\text{PDF}_\phi = \begin{cases} 0.5 \cos(\phi) & -\frac{\pi}{2} < \phi < \frac{\pi}{2} \\ 0 & \text{else} \end{cases} \quad (4.5)$$

$$C_d = 0.02 \mu\text{m}^{-1} \quad C_u = 1 \text{ (m/s)}^{-1.2}$$

where $u_{\text{lat},p}$ is the in-plane velocity of the particles, i.e. the projection of the particle velocity vector onto the pipe cross-section. The particles are injected with a random in-plane direction, such that the initial radial-velocity is negative. The average in-plane injection-velocity is $\langle u_{\text{lat},p} \rangle \approx 0.8 \text{ m/s}$, and the average radial-velocity of the injected particles is $\langle u_{r,p,\text{inj}} \rangle \approx$

-0.5 m/s. The initial axial-velocity is set to $\frac{1}{10}u_{sg}$.

The volume-mean diameter of the injected particles is $d_{30,inj} = 91.4 \mu\text{m}$, which, in a steady-state situation, is equal to the volume-mean diameter of the depositing particles, $d_{30,dep}$. The volume-mean diameter in the core of the flow results from the prescribed injection particle size-distribution, eq. 4.3, and the flow details, of which the latter may change with increasing mass-loading. Hence, the mass-loading may not be linear with the total number of particles in the core, N_p .

Both PDF_d and PDF_u are obtained from a fit to experimental data, while PDF_ϕ is an idealised representation of the variation in strength of the rate of atomisation along the pipe circumference. Using eq. 4.1, the atomisation-rate can be interpreted to scale linearly with the excess hydraulic-roughness beyond a critical value, $k_{s,crit} = 0.015D$, i.e. $\text{PDF}_\phi \propto \max(0, k_s - k_{s,crit})$. This follows the idea of, e.g., Dallman et al. (1979), that the rate of atomisation scales with the excess liquid-film flow-rate beyond a critical liquid-film flow-rate, assuming the hydraulic roughness scales linear with the liquid film-thickness. The choice of PDF_ϕ is rather arbitrary, however, the main issue here is to have maximum atomisation at the bottom of the pipe with a distribution of particle sizes and atomisation velocities that may be representative for an annular two-phase flow.

The feedback forcing of the particles is implemented similar as in chapter 3. The total pressure-gradient is increased with respect to an unladen case by an amount equal to the average dispersed-phase pressure-gradient, i.e. the average particle feedback-force per unit of volume, in order to maintain roughly the same mean axial-velocity.

According to Belt et al. (2005) the effect of the local feedback force of the particles is either (i) a roughness effect or (ii) a blockage effect. When the particles are close to the wall, they act as an added wall-roughness, increasing the near-wall Reynolds-stresses. On the other hand, the particles that are far from the wall will locally block the flow, and decrease the near-wall mean velocity-gradients and thus the Reynolds stresses.

The deposition rate, $R_{dep,N}$, is the number of particles that deposit at the wall per unit of area per unit of time, and can be described in terms of the free-flight model: a particle moving toward the wall, starts a free-flight at a distance to the wall y_{ff} , during which its radial-velocity remains unchanged. At $y = y_{ff}$ we have a distribution of particle radial-velocities, $u_{r,p,ff}$, and the deposition rate is given by:

$$R_{dep,N} = \int_0^\infty C u_{r,p,ff} du_{r,p,ff} \quad (4.6)$$

where C is the concentration of particles at $y = y_{ff}$ with a radial-velocity between $u_{r,p,ff}$ and $u_{r,p,ff} + du_{r,p,ff}$. Only particles with $u_{r,p,ff} > 0$ are able to deposit.

The deposition rate can be estimated using the deposition constant $k_{dep,N}$, and the total particle-concentration at $y = y_{ff}$, the free-flight concentration, C_{ff} :

$$R_{dep,N} = k_{dep,N} C_{ff} \quad (4.7)$$

$$C_{ff} = \int_{-\infty}^\infty C du_{r,p,ff} \quad (4.8)$$

It is convenient to distribute the particles at the free-flight position in separate classes, i , where each class is described by its particle size, d_i , and tangential position, ϕ_i . Then we have:

$$k_{\text{dep,N}} = \frac{R_{\text{dep,N}}}{C_{\text{ff}}} = \frac{\sum R_{\text{dep,N},i}}{\sum C_{\text{ff},i}} = \frac{\sum u_{r,\text{p,ff},i} C_{\text{ff},i}}{\sum C_{\text{ff},i}} \quad (4.9)$$

where $R_{\text{dep,N},i}$ and $C_{\text{ff},i}$ are the rate of deposition and the free-flight concentration of particle class i , respectively. The deposition constant is thus a concentration-weighted deposition-velocity. The variation of the deposition constant along the circumference is computed using a conditional summation in eq. 4.9, i.e. the deposition constant is calculated over all particle sizes for a given range of the tangential position: $(\phi, \phi + \delta\phi)$. Similarly, the variation of the deposition constant with particle size is computed over all tangential positions for a given range of the particle size: $(d_p, d_p + \delta d_p)$.

In the literature some models are given relating k_{dep} with the turbulence intensity of the continuous phase, and with the Stokes-number of the particle, St_p , see also chapters 3 and 3. In these models it is usually assumed that the particles are in approximate equilibrium with the turbulence of the gas phase, hence their radial-velocities are distributed similarly as the gas-phase velocity-fluctuations. Increasing the level of turbulence intensity, or decreasing St_p , in general will increase the deposition constant. For $\text{St}_p \gg 1$, the deposition velocity of the particles is expected to depend more on their injection-velocity. Also, in case of horizontal flows, the gravity becomes an important parameter for the deposition of the large particles, see, e.g. Pan and Hanratty (2002), and Westende et al. (2007a) (chapter 3). The latter also shows that the secondary flow can change the gravitational settling of the particles.

4.4 Results

Every 3D simulation is started with an initially homogeneously distributed poly-dispersion. The poly-dispersion consists of N_p particles, with $10^5 < N_p < 16 \cdot 10^5$; the size of each particle is determined using a Monte-Carlo technique and the injection-pdf, eq. 4.2. After 300,000 time steps ($t^+ > 100,000$) the flow was fully developed, and statistics were obtained from 50 uncorrelated fields. We have simulated five cases, of which the general results are shown in table 4.1. The results of table 4.1 show that for simulations F1-F3 the mass loading, the rate of deposition and the dispersed-phase pressure-gradient are roughly linear with N_p ; for simulations F4 and F5 it is no longer the case. This suggests that only for simulations F4 and F5 the feedback forcing by the particles plays a dominant role. As will be shown in the following sections, it seems that for simulation F3 the dispersed phase starts to become significant in affecting the gas-phase, which is consistent with previous results that for mass-loadings below about 0.1 the two-way coupling does not play a significant role, see Li et al. (2001).

For comparison, we also present some results of the experiments performed with our setup using PDA (see chapter 2 for a description of the setup), and some results of the experiments conducted by Dykhnov et al. (1994) in a similar setup using an isokinetic probe. The experimental works, of which general results are given in table 4.2, both concern horizontal annular flows. The experimental conditions of M1 and D1 are with a low amount of entrainment, and those of M2 and D2 are with a high amount of entrainment. In order to be able to perform

accurate PDA-measurements, our experiments, i.e. M1 and M2, are done with a superficial gas-velocity of 32 m/s, for which the amount of entrainment is large enough to ensure a high data-rate. However, to compute a gas-flow with such a high bulk Reynolds-number ($\text{Re}_{b,\text{exp}} \approx 100,000$) is still out of scope with our resources, and therefore we have chosen to simulate a gas-flow with a somewhat smaller bulk Reynolds-number ($\text{Re}_{b,\text{sim}} \approx 65,000$), equal to that used in the previous chapters. As a consequence we can only compare the experimental results and those of the simulations qualitatively.

	F1	F2	F3	F4	F5
$\langle u_{z,g} \rangle$ (m/s)	19.2	19.4	19.6	19.6	19.7
N_p	10^5	$2 \cdot 10^5$	$4 \cdot 10^5$	$8 \cdot 10^5$	$16 \cdot 10^5$
Mass loading	0.056	0.11	0.22	0.38	0.66
$R_{\text{dep},N}$ (10^6 1/m ² s)	5.73	11.3	21.6	31.9	52.3
d_{30} (μm)	85.9	85.9	85.0	80.9	77.4
$\frac{d}{dz} p_{\text{tot}}$ (Pa/m)	185	197	214	234	273
u_{∇} (m/s)	1.39	1.43	1.49	1.56	1.69
$\langle k_{\text{dep},N} \rangle$ (m/s)	0.18	0.18	0.17	0.14	0.12
$\frac{d}{dz} p_p$ (Pa/m)	11.2	21.9	40.1	56.9	92.1
a_p (m/s ²)	165	162	153	126	116

Table 4.1: General results for the simulations F1-F5. d_{30} is the volume-mean diameter of all the particles in the flow, u_{∇} is a friction velocity calculated using the pressure-gradient, and $a_p = \frac{d}{dz} p_p / \rho_p \alpha_p$ is an effective acceleration of the particles, see also chapter 3.

	M1	M2	D1	D2
source	current study		Dykhno et al. (1994)	
u_{sg} (m/s)	32	32	14.4	25.3
u_{sl} (cm/s)	1	8	1	4
D (m)	5	5	9.5	9.5
Mass loading	0.02	0.45	-	0.2
$\frac{d}{dz} p_{\text{tot}}$ (Pa/m)	376	784		
u_{∇} (m/s)	1.98	2.86		

Table 4.2: General results of flow rates of measurements of current study, and those of Dykhno et al. (1994). A description of the setup used in the current study can be found in chapter 2.

4.4.1 Mean gas-phase velocity

In fig. 4.3 the mean axial-velocity profiles are shown for simulations F1-F5. We observe that for simulation F1 and F2, with a mass loading of about 0.1 and below, the dispersion has a small effect in changing the mean axial-velocity profile; in the top region of the pipe it bulges slightly downward, and the position of maximum mean axial-velocity is shifted below the center, similar to what is observed in an unladen/one-way coupled situation, see chapter 3. In simulation F3, with a mass loading of 0.22, we observe that the maximum of the axial

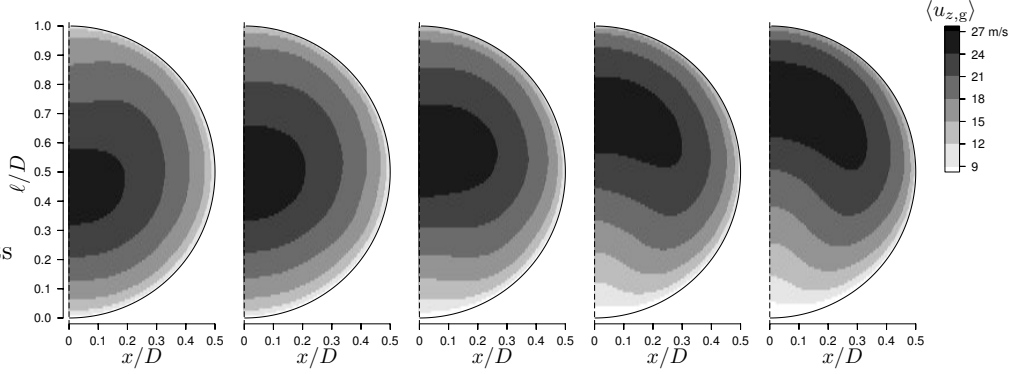


Figure 4.3: Axial velocity contour plot for F1-F5 (from left to right).

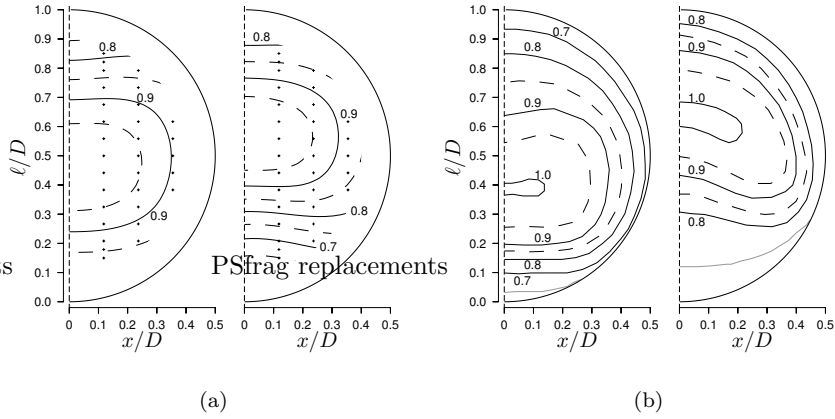


Figure 4.4: Axial velocity contour plot normalised with the maximum velocity for a) M1 and M2, and for b) D1 and D2. The symbols represent the measurement positions (80 per cross-section).

velocity is shifted slightly above the center of the pipe. Here we see both in the top and in the bottom region of the pipe a deflection of the mean axial-velocity contour toward the center. For mass loadings equal to or above 0.37, i.e. for simulations F4 and F5, the maximum of the axial-velocity is well above the center of the pipe. We see only in the bottom region of the pipe that there is a very strong deflection of the axial-velocity profile.

For comparison, we show in fig. 4.4 the results of the mean axial-velocity of the experimental work M1, M2, D1 and D2, see also table 4.2. The left graph of both fig. 4.4a and fig. 4.4b represent a flow condition with a low amount of entrainment, and the right graphs represent those with a high amount of entrainment. Similar to the simulations F1 and F2, we see for the flow conditions with a low amount of entrainment a downward shift of the position of maximum mean axial-velocity and a small deflection in the top region of the pipe. With a

high amount of entrainment the opposite is shown, and compares with simulations F4 and F5. The deflection of the velocity profiles measured in our setup with the PDA seems to be much smaller than measured by Dykhno et al. This may be caused by the film-extraction at about 1 pipe-diameter stream upward from the measurement position. If the extraction is not done completely iso-kinetic the gas flow has to adjust itself, and the secondary flow may be disrupted. Also, in case of a low amount of entrainment, e.g. M1, the driving force for the secondary flow, i.e. the variation in roughness of the wavy film, is removed by the extraction, and this may weaken the secondary flow.

In fig. 4.3 we observe deflection regions (concavities) in the iso-velocity contours. Assuming these are created by the secondary flow pattern, we intuitively expect a pair of vortical cells per deflection region, i.e. one pair for simulations F1, F2, F4 and F5, and two pairs for simulations F3. For simulations F1 and F2 the vortical cells have a flow downward through the center, for simulation F3 the vortical cells have a flow from the center toward the sides, and for simulations F4 and F5 two vortical cells with a flow upward through the center.

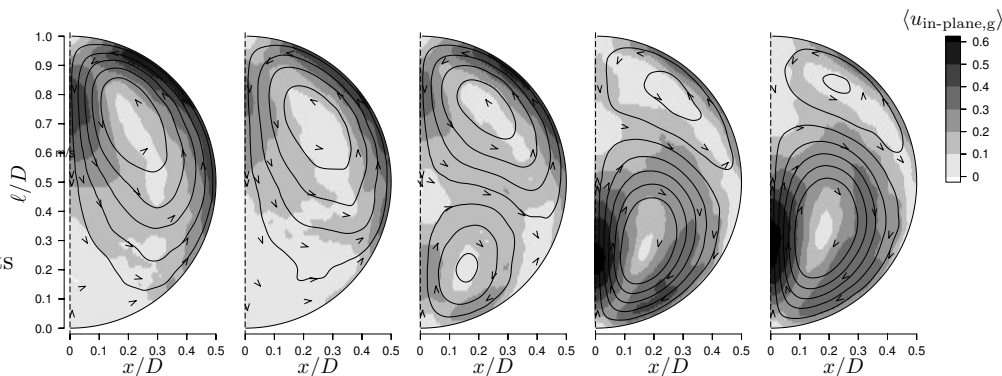


Figure 4.5: Mean in-plane velocity contour plot for F1-F5 (from left to right).

In fig. 4.5 the secondary-flow is shown for simulations F1-F5. For simulations F1 and F2 the secondary flow pattern is similar to that found in an unladen case with a similar wall-roughness variation, see Westende et al. (2007a). The maximum in-plane velocity is about 0.55 m/s at $\phi \approx 135^\circ$ at the wall-nearest grid-point. For F2 the dispersed phase seems to slow down the secondary flow slightly.

Increasing N_p , in simulation F3 we see a second vortical cell-pair with a roughly constant velocity of about 0.2 m/s appearing in the bottom region of the pipe. The value and position of the maximum in-plane velocity remains unchanged.

Increasing N_p further, the bottom cell grows in size and strength, but the top vortical cell-pair remains present. Even though there are twice as much particles in F5 than in F4, the strength of the secondary flow seems to be equal: for both simulations the maximum in-plane velocity is about 0.65 m/s at the vertical through the center at $\ell \approx 0.25D$. It is not clear whether the top vortical cell-pair is driven by the variation in wall-roughness in the top region of the pipe, or due to the shear with the vortical cells in the bottom region.

Although there exists in principle no direct connection between the mean axial-velocity profile and the secondary-flow pattern, when there exists both a variation in the wall-roughness and

a non-uniform particle distribution, see Belt et al. (2005), it seems that for an actual annular flow, represented by the idealised situations (F1-F5), we can use the axial-velocity profile to predict the direction of the secondary-flow. The vortical cells in the top region of simulations F4 and F5, however, are too weak to be identified by the axial-velocity profile. We observe that at the concave side of the deflections in the axial-velocity profile, the in-plane velocity shows a local maximum. For simulations F1-F3 this local maximum is not the absolute maximum, but for F4 and F5 it is.

4.4.2 Particle concentration

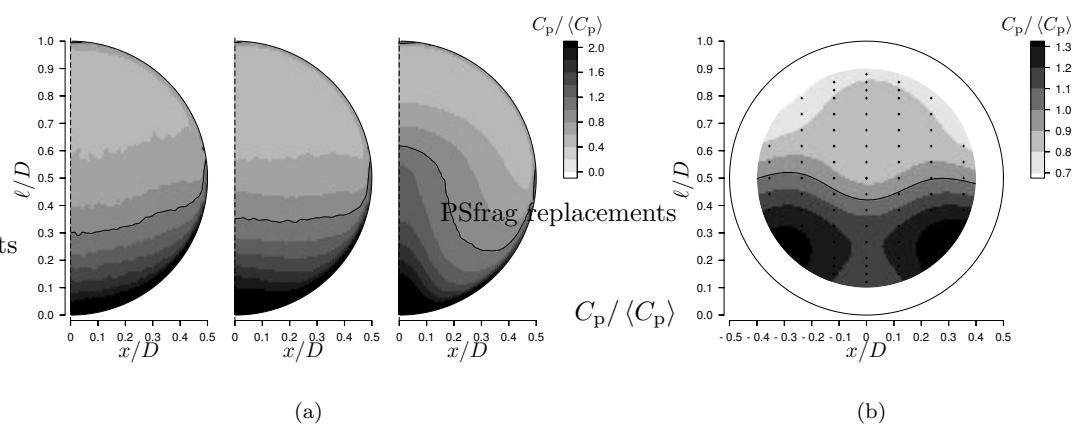


Figure 4.6: a) Concentration contour plot for a) F1, F3 and F5, and b) for M1, normalised with the mean concentration. The solid line represents the normalised iso-concentration plane with a value of 1.

In fig. 4.6a we show the concentration profile of the particles in the pipe cross-section for simulations F1, F3 and F5, and in fig. 4.6b we show the droplet concentration cross profile of M1; all profiles are normalised with the mean concentration.

For simulations F1-F3 the concentration profile is fairly stratified. The secondary flow of F1 and F2 pushes the iso-concentration profiles downward in the center of the pipe, and upward along the side walls. In simulation F3, the vortical cells in the bottom region of the pipe, push the particles upward, making the iso-concentration planes more straight than for simulations F1 and F2. The effect of the secondary flow on the concentration profile is rather mild, since at the location where the concentration is highest, i.e. in the bottom region, the strength of the secondary flow is rather small (F1 and F2), or the lower vortical-cells are too weak.

For simulations F4 and F5 the secondary flow is much stronger at the location of high particle concentration: the secondary-flow strength reaches a maximum value of about 0.6 m/s, corresponding to the free-fall velocity of a particle with a diameter of 140 μm . At the vertical through the center, the secondary flow transports particles upward from the bottom wall, a region of high particle concentration, to the center of the pipe. Simultaneously, it transports particles from the side walls, a region of lower particle concentration, to the bottom wall. As

a consequence the concentration profile bulges strongly upwards in the bottom region of the pipe. However, since the secondary flow loses its strength for $\ell \gtrsim 0.5D$, the particles are not transported completely to the top wall of the pipe.

The experimental results of the concentration profile of M1 should be compared with simulation F1, since both have a low mass-loading. At $\ell \approx 0.5D$, we observe a deflection of the iso-concentration plane downward in the center, whereas at the sides ($|x| \approx 0.3D$), these planes are deflected upward, similar as observed in simulation F1. For both M1 and F1 the concentration is maximum in the bottom region of the pipe, but for M1 we find a local minimum at $x \approx 0$ and $\ell \approx 0.1D$, which is absent in F1. The reason for this difference is yet unclear, but may be a result of corner-effects in the actual annular flow of M1, see fig. 4.1 ($\phi \approx \pm 45^\circ$). This can locally affect the atomisation of M1, which is not taken into account in the idealised injection of F1, which is monotonically distributed along the pipe circumference.

Effect of poly-dispersion

According to, e.g., Pan and Hanratty (2002) the particle concentration profile in the cross-section of a horizontal pipe flow is the result of a competition between gravitational settling and turbulent diffusion of the particles, and gives a classical Rouse-profile: the concentration decreases exponentially with increasing vertical distance to the bottom, and it is constant in a horizontal plane, i.e.:

$$C = C_{\ell=0} \exp\left(-\frac{u_{p,t}}{\mathcal{D}}\ell\right) \quad (4.10)$$

$$\mathcal{D} = \zeta \frac{1}{2} D u_\tau \quad (4.11)$$

where $u_{p,t}$ is the Stokesian terminal free-fall velocity of the particles, \mathcal{D} is the turbulent diffusivity, and ζ a constant with a value of about 0.04 to 0.08. Here, the effect of secondary flow is not taken into account. We expect the Rouse-profile to be most useful when the particles are in equilibrium with the gas-phase turbulence, i.e. when the behaviour of the particles is independent of their initial conditions. Since the overall volume-mean diameter is about 80 μm , see table 4.1, which is in the range of the intermediate particles that have much interaction with the gas phase ($50 \mu\text{m} \lesssim d_p \lesssim 100 \mu\text{m}$, see chapter 3), the equilibrium condition probably is roughly satisfied.

In a poly-dispersion the gravitational settling of the larger particles is stronger than that of the smaller particles, and the resulting ‘poly-dispersed’ Rouse-profile is a weighted sum of exponential functions with varying decay constants, and may not be exponential itself; the weight-factors are determined by the particle-size distribution describing the poly-dispersion. Also, the volume-mean diameter of the particles will decrease with the distance from the bottom.

In fig. 4.7 we show the profile of the particle concentration of simulations F1, F3 and F5, and the results of M1 (symbols). We also have plotted the result of a poly-dispersed Rouse-profile, using $u_\tau = 1.5 \text{ m/s}$ and $\zeta = 0.04$, according to a particle-size distribution given by eq. 4.3 (solid line). The dashed line in fig. 4.7 is an exponential decaying concentration-profile, representing a ‘mono-dispersed’ Rouse-profile with $d_p \approx 53 \mu\text{m}$, fitting the concentration profile of F3 for $0.05 \lesssim \ell/D \lesssim 0.45$ best. Here we note that the arithmetic-mean of F3 in the bottom region of the pipe is about 55 μm .

From fig. 4.7 we see that the poly-dispersed Rouse-profile fits the overall concentration profile

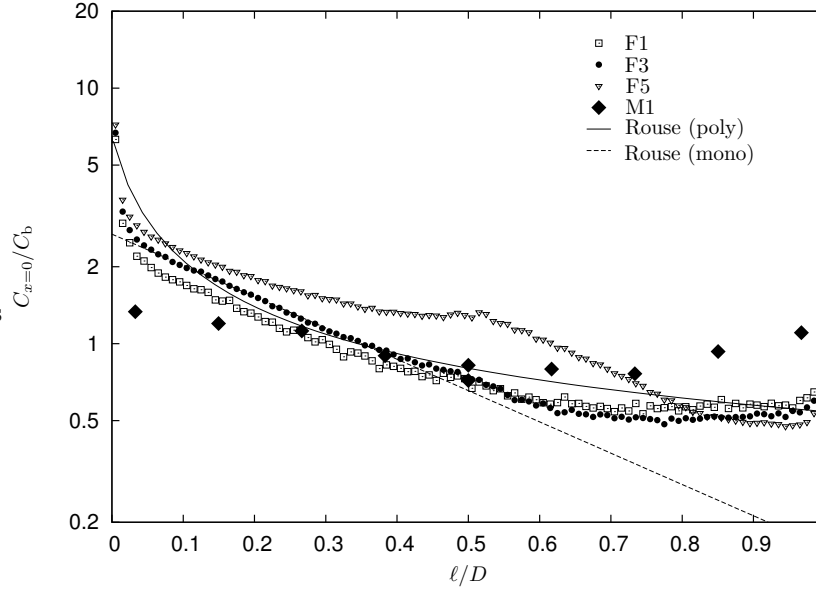


Figure 4.7: Normalised number concentration of simulations F1, F3 and F5, of experiment M1, and of a Rouse profile of a mono-dispersion and a poly-dispersion with a pdf given by eq. 4.3.

of simulations F1 and F3 better than the mono-dispersed Rouse-profile. However, for $\ell/D \lesssim 0.1$ the concentration profile fits the mono-dispersion best. For F5 the concentration profile seems to be constructed of two poly-dispersed Rouse-profiles: (i) one for the bottom region of the pipe, where the secondary flows is upward through the center, decreasing the free-fall velocity of the particles and hence flattening the concentration profile, see also eq. 4.10, and (ii) one for the top region of the pipe, where the opposite happens, and the concentration profile decreases stronger with increasing vertical distance to the bottom of the pipe. Here it is interesting to see that, even though there are also two vortical cells present in simulation F3, they are not strong enough to breakup the Rouse-profile into two parts, as observed in simulations F4 and F5. In the top of the pipe the concentration is rather uniform, and this is captured rather well by the poly-dispersed Rouse-profile.

In fig. 4.8 the volume-mean particle-diameter of simulations F1, F3 and F5 is shown (symbols), together with the result of a poly-dispersed Rouse-profile, using $u_\tau = 1.5$ m/s, $\varsigma = 0.04$, and eq. 4.3 (solid line). For all simulations we observe a difference in the volume-mean diameter of about a factor 2.5 between the bottom of the pipe and the top of the pipe. The prediction of the poly-dispersed Rouse-profile also shows a difference between the bottom and the top of the pipe, but the variation is too strong, i.e. the volume-mean diameter at the top of the pipe is about 4.5 times smaller than at the bottom of the pipe. Most likely, using the Rouse-profile, the gravitational settling is overestimated, affecting the large particles strongest. This is also clearly visible in fig. 4.7: for $\ell/D \lesssim 0.1$ the concentration in the bottom region predicted by the Rouse-profile increases stronger than seen in the simulations. The overestimation of the gravitational settling in the Rouse-profile may be caused by omitting the effect of the

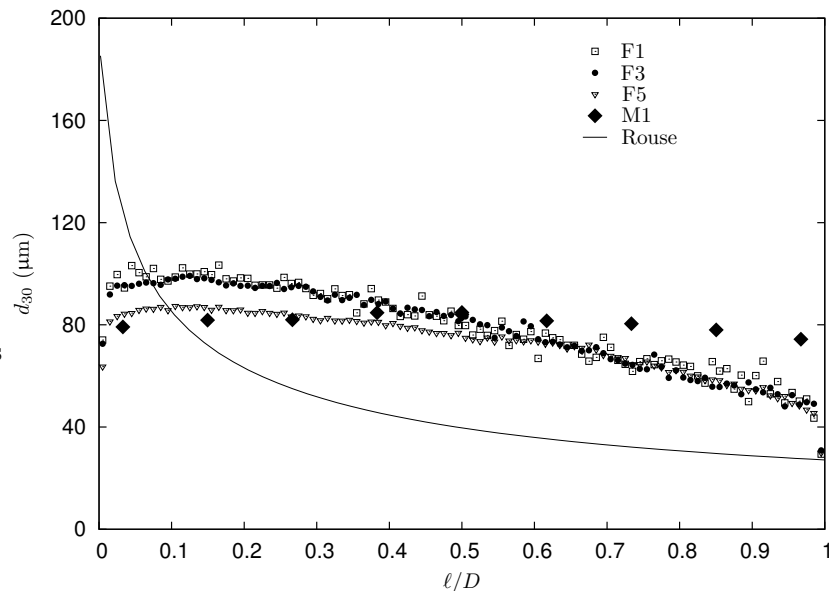


Figure 4.8: Volume-mean diameter of simulations F1, F3 and F5, of experiment M1, and of a Rouse profile of a poly-dispersion with a pdf given by eq. 4.3.

secondary flow. Also, as is shown by Westende et al. (2007a), the turbulence interaction may decrease the free-fall velocity of a particle as well, which is not taken into account in the model for the Rouse-profile. The change in the gravitational settling by the secondary flow is again clearly visible for F5: the variation in the volume-mean diameter with vertical distance to the bottom of the pipe is smallest.

4.4.3 Driving force of the secondary flow

According to Belt et al. (2004) the driving force of a secondary flow is the divergence of the Reynold-stress tensor. In general, the main contributor is the tangential derivative of the normal-stress in the tangential direction, $\tau_{\phi\phi}$, pushing the flow from regions with high $\tau_{\phi\phi}$ toward regions with low $\tau_{\phi\phi}$ along the wall.

From this it follows that a secondary flow ‘generated’ by enhanced wall-roughness at the bottom wall, i.e. $\tau_{\phi\phi, \text{bot}} > \tau_{\phi\phi, \text{top}}$, results in an upward flow along the pipe wall, see fig. 4.9a. Note that the variation of roughness can also be caused by the roughness effect of the particles close to the wall in combination with gravitational settling.

On the other hand, the particles that are further away from the wall, in the lower part of the pipe, block locally the mean flow, thus decrease the near-wall Reynolds-stresses. The blocking-effect in the lower part of the pipe does not significantly change the Reynolds-stresses in the top region of the pipe. In such a situation we have $\tau_{\phi\phi, \text{bot}} < \tau_{\phi\phi, \text{top}}$, and the resulting secondary-flow is in the opposite direction, see fig. 4.9b.

In fig. 4.10 we show the tangential normal Reynolds stress of simulations F1-F5.

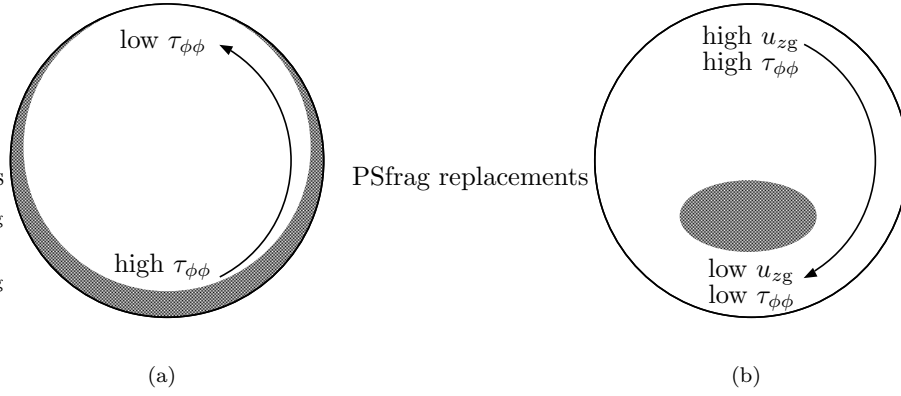


Figure 4.9: Schematic representation of the generation of a secondary-flow pattern a) by a variation in the roughness along the pipe circumference, and b) by the blockage effect. The non-uniform distribution of the feedback forcing results in a secondary-flow pattern.

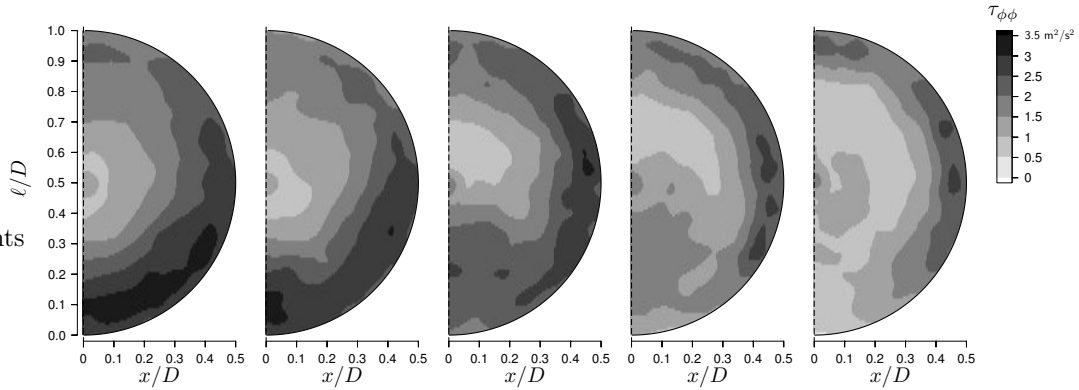


Figure 4.10: Normal Reynolds stress in tangential direction of simulations F1-F5 (from left to right).

For simulations F1 and F2 the influence of the dispersed phase on the gas phase is very small, and the profile of the normal Reynolds stress in tangential direction results from the variation of the wall-roughness. The driving force for the secondary flow is slightly smaller in simulation F2 than in simulation F1, and this is in agreement with the slightly weaker magnitude of the secondary-flow velocity, see fig. 4.5.

Increasing N_p , for simulation F3 the Reynolds stresses in the bottom region of the pipe become smaller than at the side walls: $\phi \approx \pm 90^\circ$, see fig. 4.10. As a result, the vortical cell-pair in the bottom region of the pipe flows in the opposite direction than in simulation F1 and F2. The Reynolds stress in the top region of the pipe is also smaller than at the side walls, and thus we also have a vortical cell-pair in the top region of the pipe.

When we increase N_p even more, the difference in the Reynolds stresses between the side walls

and the bottom region of the pipe become larger, i.e. the driving force of the lower vortical cell increases. The bottom vortical cells now are strong enough to transport a significant amount of particles in the bottom region of the pipe upward (see right graph of fig. 4.6a), and the blocking effect extends more toward the center. With the blocking effect extending to the center of the pipe, the maximum of the mean axial-velocity ‘shifts’ upward, resulting in a strong deflection in its profile at $\ell/D \approx 0.6$, see fig. 4.3. This is a typical sign when the secondary flow is generated by the blocking effect of the particles. Also, because of the upward shift of the maximum of the mean axial-velocity, we expect the Reynolds stresses in the bottom region to decrease and those at the top of the pipe to increase. This will increase the driving force of the secondary flow for the lower vortical cells, whereas it decreases for the top vortical cells. The upward transport of the particles thus seems to enhance the strength of the lower vortical cells.

From fig. 4.10 the magnitude of the driving force can be estimated: for simulation F1 we have $\left(\frac{\partial \tau_{\phi\phi}}{r \partial \phi}\right)_{r=R} \approx 25$ Pa/m, and for F5 we have $\left(\frac{\partial \tau_{\phi\phi}}{r \partial \phi}\right)_{r=R} \approx 74$ Pa/m. The effect of gravity onto the secondary flow is estimated with $C_p \frac{\pi}{6} d_{30}^3 g \approx 0.7$ Pa/m for F1, and 7.8 Pa/m for F5. In a similar way the direct effect of the injection of the particles onto the secondary flow can be estimated with $C_p C_D \frac{1}{2} \rho_g (u_{r,p,inj} - u_{sf})^2 \frac{\pi}{4} d_{30}^2 \approx 2.2$ Pa/m for F1, and 4.3 Pa/m for F5; C_D is the drag coefficient, and u_{sf} is the magnitude of the secondary flow. From this it follows that in both cases the modification of the distribution of the Reynolds stress determines the secondary flow.

Here we note that the blocking effect is a passive effect, and therefore can not lead to a reversal of the mean-axial flow direction. Also because $\tau_{\phi\phi}$ cannot change sign, the maximum difference in $\tau_{\phi\phi}$ between $\phi = 0$ and $\phi = \pm 90^\circ$ is determined by the maximum value of $\tau_{\phi\phi}$ at $\phi = \pm 90^\circ$, and not by its minimum value at $\phi = 0$, which is close to zero. Since $\frac{d}{dz} p_{tot}$ does not seem to change significantly with increasing N_p , the maximum value of $\tau_{\phi\phi}$ remains approximately equal, and the magnitude of the secondary-flow will not change much: for simulations F1-F5 the maximum strength of the secondary flow is about 0.5 m/s. Also, the blocking effect seems to saturate with increasing mass loading; this is shown by the effective acceleration of the particles, a_p , which is the dispersed-phase pressure-gradient per unit of mass-loading: a_p decreases with N_p , see table 4.1.

The blocking effect decreases with increasing distance to the bottom, because the particle concentration and the particle slip velocity decrease, i.e. the local dispersed-phase pressure-gradient decreases. In fig. 4.11 we see the cumulative dispersed-phase pressure-gradient with increasing distance to the bottom of the pipe. The dispersed-phase pressure-gradient in the lower half of the pipe ($\ell < 0.5D$), amounts up to about 85% of the total dispersed-phase pressure-gradient, and therefore the blocking effect remains in the lower half of the pipe. As a consequence, the driving force for the secondary flow is more focussed in the bottom region of the pipe: the Reynolds stresses decrease strongly in the bottom region, whereas they remain roughly unchanged at the top and the sides of the pipe. This may explain why the vortical cells do not reach the top of the pipe in simulations F4 and F5.

Along the wall, in the top region of the pipe, the distribution of the Reynolds stresses hardly changes. It thus seems that the variation of wall-roughness remains here the driving mechanism for the secondary flow, for all simulations. Since the blocking-effect as the driving force remains in the lower half of the pipe, the vortical cells in the top of the pipe will persist there. Note that for simulations F1 and F2 the blocking effect is very small, i.e. the dispersed-phase

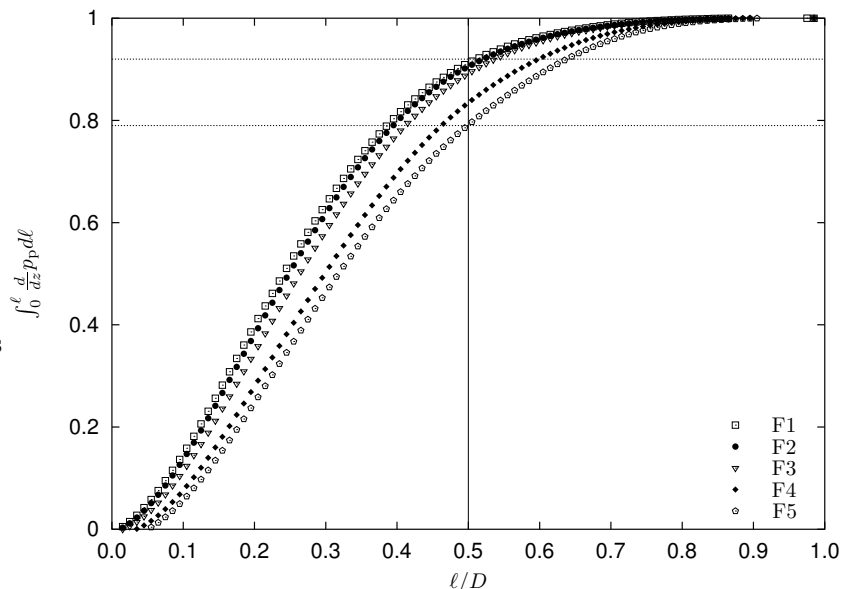


Figure 4.11: Cumulative blocking effect.

pressure-gradient is only about 10% of the total pressure-gradient. Therefore, only the top vortical cells are present, and extend throughout the whole cross-section.

4.4.4 Deposition

According to Westende et al. (2007a), the deposition constant varies along the pipe circumference. In the bottom region of the pipe the gravity and the turbulent diffusion are working in the same direction, whereas in the top region of the pipe they are opposing each other. They show that the secondary flow decreases the gravitational settling, flattening the deposition-constant profile along the pipe circumference, and increasing relatively the deposition constant at the top of the pipe. In fig. 4.12a we show $k_{\text{dep},N}$ as a function of ϕ for simulations F1-F5. For simulations F1 and F2 the number deposition-constant at the bottom of the pipe is an order of magnitude larger than that at the top of the pipe. The average value of the deposition constant is somewhat smaller than observed by Westende et al. (2007a), but this may be caused by the large number of very small particles present in the pipe: over 30% of all particles in the pipe have a diameter $d_p \lesssim 20 \mu\text{m}$, and these particles have a very small deposition constant.

For simulation F3-F5, the secondary flow counteracts the gravitational settling in the bottom region of the pipe for $|x| \lesssim 0.2 D$, and locally the deposition constant is reduced with increasing strength of the secondary flow. The maximum of the deposition constant at $\phi \approx 50^\circ$ can be linked with the streamlines of the secondary flow pattern, which are directed towards the wall at $\phi \approx 50^\circ$, see fig. 4.12b and fig. 4.5.

Besides a variation along the pipe circumference, the deposition constant also depends on the

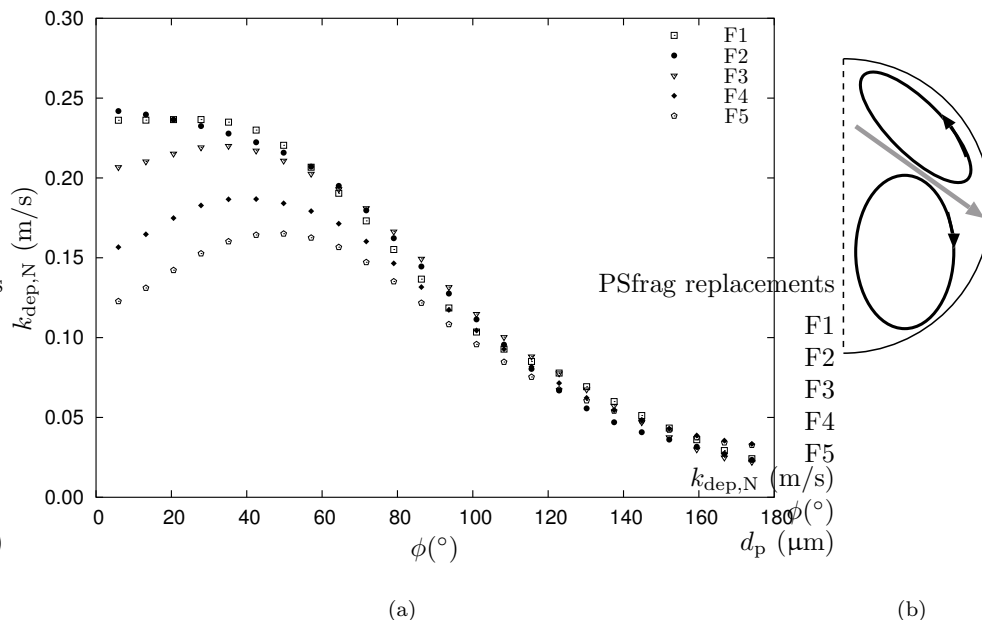


Figure 4.12: a) Deposition constant along circumference. b) Schematic representation on how the secondary-flow cells of F3-F5 can enhance the deposition at $\phi \approx 50^\circ$.

particle size. In fig. 4.13 we show the average deposition-constant, $\langle k_{\text{dep}} \rangle_\phi$, as a function of the particle size for simulations F1-F5, which all have a similar shape. For simulation F5, the gravitational settling is least important, and compares best with the results of Westende et al. (2008), showing the deposition constant of a poly-dispersion in a vertical flow.

For $d_p \lesssim 10 \mu\text{m}$ the deposition constant decreases with decreasing particle size, because they behave more tracerlike, and because we have implemented impermeability of the wall for the gas-phase, i.e. ideal tracers have a zero deposition velocity at the wall hence it is unlikely for them to deposit. Here we note that the concept of free-flight deposition is not valid for these smallest particles.

For particles with $20 \mu\text{m} \lesssim d_p \lesssim 100 \mu\text{m}$ the deposition constant decreases with increasing particle size, probably because their increased inertia results in a smaller interaction of the particles with the gas-phase turbulence, and deposition due to turbulent diffusion will decrease.

When the particles are larger than about $200 \mu\text{m}$ their deposition is expected to be dominated by the injection process, which is equal for all particles. Probably, after injection the in-plane velocity of the particles is reduced due to drag, affecting the largest particles least. Hence the deposition velocity of the largest particles will be largest, and thus the deposition constant increases again with increasing particle size.

Westende et al. (2008) (chapter 3) proposed to divide the particles in three size-classes: (i) ‘tracer’-particles, with $\text{St}_p \lesssim 1$, (ii) intermediate particles, with $1 < \text{St}_p \lesssim 10$, and (iii) large

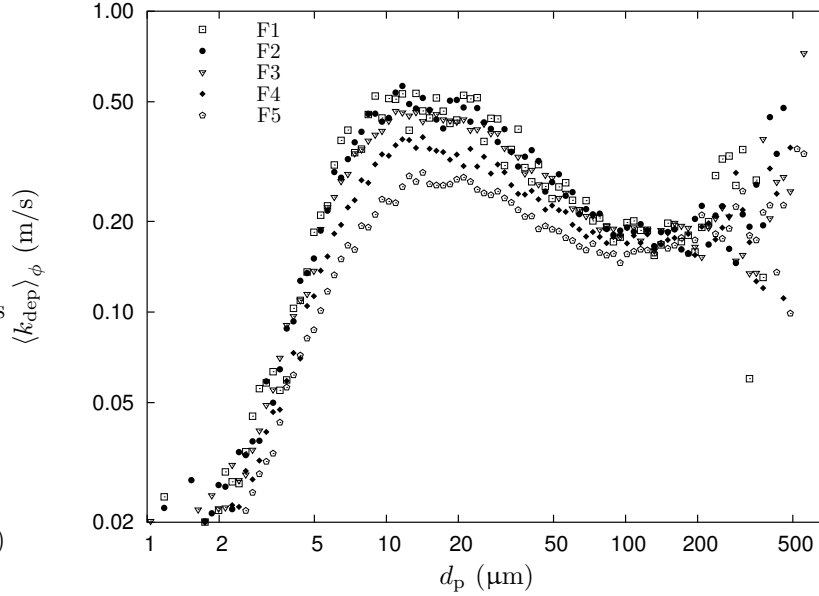


Figure 4.13: Deposition constant as a function of the particle diameter.

particles with $St_p > 10$, where the St_p is the particle Stokes number based on the Stokes particle-relaxation-time, and the time scale of the large-scale turbulence, which is given by $\mathcal{T} = 0.046D/u_{\nabla}$, according to Pan and Hanratty (2002). Using an effective friction-velocity, $u_{\nabla} = 1.5 \text{ m/s}$, particles with $d_p \lesssim 20 \mu\text{m}$ are considered to be tracers, particles with $20 \mu\text{m} \lesssim d_p \lesssim 100 \mu\text{m}$ are considered intermediate sized, and when we have $d_p \gtrsim 100 \mu\text{m}$ the particles are large. Westende et al. (2007b) (chapter 2) also implicitly used this division; they assumed droplets in the size-range of $10 \mu\text{m}$ to $20 \mu\text{m}$ to behave roughly tracerlike, making them suitable for estimating the mean axial gas-velocity in an annular-dispersed gas-liquid flow (their effective friction-velocity was about 2.5 m/s).

The sharp decrease of the deposition constant for $d_p \lesssim 10 \mu\text{m}$, corresponding to $St_p \approx 0.2$ and $\tau_p^+ \approx 50$, agrees rather well with the decrease in the deposition constant shown by Young and Leeming (1997) for $\tau_p^+ \lesssim 20$, i.e. they show the results of the experiments of several authors. They refer to this size-range as the diffusion-impaction regime, and explain its behaviour in terms of the free-flight model. However, according to them, for these particles the gas-phase radial-velocity fluctuations at the position where they would start their free-flight is too small to provide the particles with sufficient wallwards momentum. The reason for this has never been explained satisfactorily, and it remains questionable whether a free-flight model may be used for these small particles.

The decrease of the deposition constant with a factor of about 2 for the intermediate particles is also observed in the experiments of Liu and Argawal (1974), taken from Young and Leeming (1997); they refer to this size-range as the inertia-moderated regime. The magnitude of their deposition constant normalised with the friction-velocity is about 0.2, and agrees with our results of the intermediate particles.

According to Young and Leeming (1997) the maximum of the deposition constant at about $\tau_p^+ = 50$ is related to the maximum of the turbophoresis effect. In our simulations this corresponds to a particle size of about $d_p = 10\mu\text{m}$, and the secondary flow seems to have a large impact on the deposition constant for this size range. Possibly, this is a result of a crossing-trajectory effect, see Csanady (1963), because the secondary flow may uncorrelate the particle motion from the turbulence.

Since the deposition constant of the tracer-particles is very small, it is expected that their residence time is relatively large. In fig. 4.14 we show the average residence time of simulations F1-F5 as a function of the particle diameter. In this figure we have also plotted an estimate for the residence time using the deposition constant for simulation F3 (solid line), and the match with the result of the residence time of simulation F3 confirms the link between a small deposition constant and a large residence-time. Because the residence time of the tracer-particles is on average much larger, there are relatively many small droplets, and thus the volume-mean diameter of the particles in the core of the gas-flow, d_{30} , is smaller than the volume-mean diameter of the depositing particles, $d_{30,\text{dep}}$, which, in a steady state situation, is equal to the volume-mean diameter of the injected particles, $d_{30,\text{inj}} = 91.4\mu\text{m}$, see table 4.1.

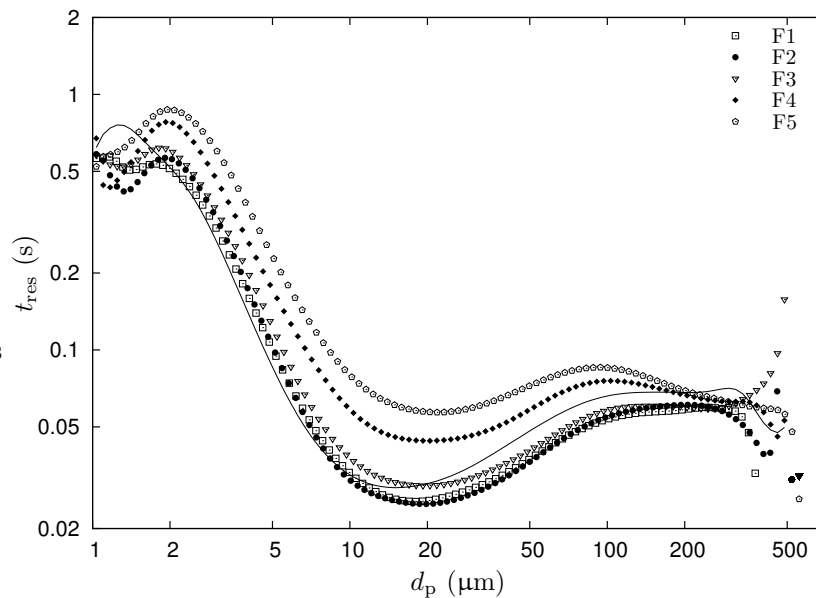


Figure 4.14: Residence time as a function of the particle size. The solid line represents $\langle t_{\text{res}} \rangle = D_h/4k_{\text{dep},N}$ for simulation F3, see Westende et al. (2008).

4.5 Conclusion

We have performed high Reynolds number Large-Eddy Simulations of a horizontal air flow of about 20 m/s in a pipe with $D = 5$ cm. Particles are injected into this flow with their initial conditions determined by a prescribed injection pdf, hence mimicking the atomisation process of droplets in an annular-dispersed gas-liquid flow. Wall-functions are implemented in order to imitate the circumferential variation in roughness of the wavy liquid-film due to the variation in liquid film thickness. Two-way coupling is also implemented using the point-force method to study the influence of the dispersed phase onto the gas phase with increasing mass-loading. Where possible, the results are compared with PDA-measurements of the core of a horizontal annular-dispersed air-water pipe-flow, with $u_{sg} = 32$ m/s, $u_{sl} = 1$ cm/s or 8 cm/s, and $D = 5$ cm.

For a low mass-loading ($\lesssim 0.1$) the dispersed phase has a negligible effect on the gas phase: the secondary flow, generated by the variation in wall-roughness is almost unchanged. This is in agreement with our PDA-measurements, and with the experiments performed by Dykhno et al. (1994) for air-water flows with a low amount of entrainment. Increasing the mass-loading, an extra vortical-cell pair is created in the bottom region of the pipe, counter-rotating with respect to the ‘original’ ones, which are ‘pushed’ to the top region of the pipe. The secondary flow in the bottom region of the pipe is generated by the blocking effect of the particles, and is more effective in transporting the particles upward. Thus the blocking-effect of the particles extends more toward the center of the pipe, enhancing the secondary flow. As a result the axial velocity profile also shows a strong deflection in the iso-axial-velocity contours, which is also observed in the experiments of Dykhno et al. (1994), and in our PDA-measurements for air-water flows with a high amount of entrainment. For high mass-loading, the blocking effect of the particles seems to saturate.

From the deposition behaviour of the particles, three particle size classes are distinguished: *(i)* tracer particles, $St_p \lesssim 1$, *(ii)* intermediate particles, $1 \lesssim St_p \lesssim 10$ and *(iii)* large particles, $10 \gtrsim St_p$. The variation of the deposition constant with particle size agrees rather well with the observations of Young and Leeming (1997), and of Westende et al. (2008). The secondary flow generated by the particles reduces the deposition constant at the bottom of the pipe.

5. The effect of secondary flow on a particle distribution

In horizontal annular dispersed pipe flow the liquid film at the bottom is thicker and rougher than at the top of the pipe. A turbulent pipe flow experiencing a variation of roughness along the pipe wall will show a secondary flow. Such secondary flow, consisting of two counter-rotating cells in the cross-section of the tube, can change the distribution of the droplets inside the pipe and their deposition at the wall. Here, we compare the behaviour of the droplets (dispersed phase) with and without secondary flow, using large-eddy simulations. It is shown that the presence of secondary flow increases the droplet concentration in the core of the pipe and the droplet deposition-rate at the top of the pipe.

This chapter has been published in *Int. J. Multiphase Flow* 33:67-85, 2007.

5.1 Introduction

In horizontal annular two-phase flow, the liquid-phase flows partly as a thin film along the tube wall and partly as entrained droplets in the turbulent gas core. Due to gravitational pull, the liquid film at the bottom part of the pipe usually is thicker than that at the top of the pipe. Similarly, the concentration of drops will be higher in the bottom region than in the top region of the pipe. This flow regime occurs often in transport pipes of gas and oil and in heat exchangers. An important parameter for this flow regime is the film flow-rate along the wall. When part of the pipe wall is not covered with a liquid film, corrosion of the wall can take place and heat exchange from the wall to the liquid is deteriorated, a so-called dry-out. The gravitational pull on the liquid film results in a constant drainage of liquid from the top of the pipe towards the bottom. In order to maintain a liquid film along the entire wall of the pipe, other mechanisms have to be present to transport the drained liquid back to the top of the pipe. A number of such mechanisms have been proposed over the years, see e.g. Mols (1999):

1. Surface tension: curvature differences in the liquid film along the circumference induce pressure gradients in the tangential direction, ‘pumping’ the liquid film upwards. This effect is only important for small-diameter pipes ($D < 5$ mm for air-water systems).
2. Secondary gas-flow: a mean flow in the cross-section of the pipe, usually manifested as multiple counter-rotating cells (see fig. 5.1c), is able to drag the liquid film upwards by

its tangential shear-force. Secondary flow can be induced by a varying wall-roughness, Darling and McManus (1968), by the non-uniformity of droplet concentration, Belt et al. (2005), or by the fact that the gas is flowing through an non-circular cross-section, Speziale (1982).

3. Entrainment/deposition: droplets, mostly atomised from the thick film at the bottom part of the pipe, can deposit downstream in the top region, where they contribute to the film.
4. Wave-spreading: large amplitude waves, being deformed by the non-uniform depth of the liquid film, tend to bend sideways and spread over the circumference.

The effects of secondary flow on the liquid film are quite controversial. Jayanti et al. (1990) simulated a secondary flow and found its tangential shear to be insufficient to sustain a liquid film at the top of the pipe wall. In a later paper (Jayanti and Hewitt (1996)), using isolated patches of wall-roughness, they even question the existence of secondary flow in annular flow. Measurements of Dykhno et al. (1994), Flores et al. (1995) and Williams et al. (1996), however, do show the existence of secondary flow. Lin et al. (1985) made a model including all four mechanisms mentioned above; they concluded that secondary flow and entrainment/deposition are the dominant mechanisms for the film distribution.

All the work mentioned above deals with the direct effect of the secondary flow on the liquid film. However, the secondary flow can also have an indirect effect on the liquid film by affecting the distribution of the droplets and their deposition at the wall. The objective of this paper is to study how the secondary flow, induced by a variable wall-roughness, influences the dispersed-phase distribution and the deposition-rate. The study was performed by doing numerical simulations both without secondary flow and with secondary flow created with a varying wall-roughness. In our computations, the processes that drive the dispersed phase are: gravitational settling, turbulence interactions and secondary flow, fig. 5.1. Gravity pulls the droplets down, thus increases the deposition at the bottom of the pipe and diminishes it at the top. The turbulence of the gas acting on the droplets, via the drag force, tends to push them towards zones of low turbulence intensity (i.e. the wall); a phenomenon known as turbophoresis, Young and Leeming (1997). Turbophoresis has no preferential deposition region and deposits the droplets uniformly along the wall, provided the turbulence intensity shows cylindrical symmetry.

The proposed effects of secondary flow are that the droplets are dragged along with its counter-rotating cells, transporting them to the top of the pipe, therefore increasing the droplet-concentration in the core and top regions of the pipe. The gravitational settling of the droplets along the wall is reduced by the secondary flow, but in the core of the pipe it is enhanced. Another possible deposition mechanism is the centrifugal effect of secondary flow: due to inertia the droplets tend to be swept outwards, depositing on the pipe wall. Similarly to turbophoresis, deposition by the centrifugal effect should occur everywhere along the circumference, but not necessarily with equal strength.

The paper is organised as follows. In section 5.2, we formulate the problem and detail the major mechanisms involved. The models used in the numerical simulation of the particle-laden turbulent pipe flow and for creating a secondary flow are described in section 5.3. The validation of these models is provided in appendix A. In section 5.4.1 the results of the

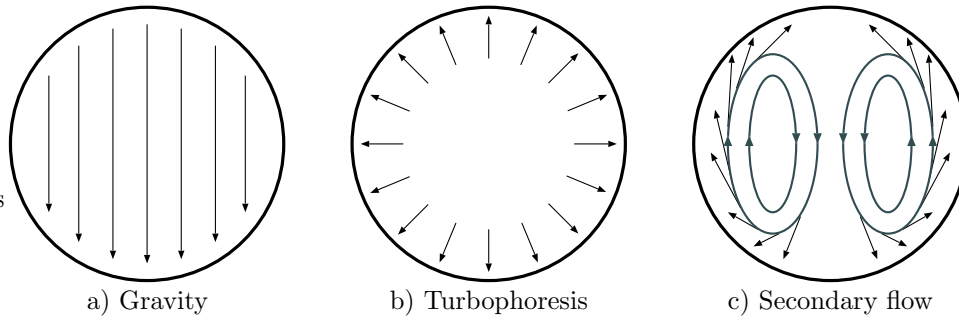


Figure 5.1: Deposition mechanisms in a horizontal annular dispersed pipe flow.

secondary flow are shown, and its effects on the dispersed phase are described in section 5.4.2. Finally, some concluding remarks are given in section 5.5.

5.2 Problem formulation

Instead of simulating the liquid film, in this paper we consider a simplified situation: the gas-liquid interface is represented by a circular wall with a varying roughness, inducing a secondary flow pattern. The droplets are considered as small solid spheres and are driven by drag and gravity only, which are the most important driving mechanisms in the actual situation. To focus on the effect of secondary flow on the particles, we also neglect the effect of the particles on the flow and inter-particle interactions (i.e. we consider one-way coupling). Since there does not exist any fundamental study on the effect of the secondary flow on a dispersion of droplets in a horizontal annular flow, we deliberately kept the situation as simple as possible, leaving out all forces acting on the particles except for drag and gravity, and leaving out two-way coupling and inter-particle collisions. In this way, the effect of secondary flow itself on a dispersion is isolated, allowing a better understanding of the physical mechanisms involved. Note that including two-way coupling might change the secondary flow pattern; Belt et al. (2004), Dykhno et al. (1994).

In a real annular flow, droplets continuously deposit onto and re-entrain from the liquid film. Once a droplet is created, we can calculate its path using the forces exerted on it. When the droplet hits the wall, it is removed from the flow. In steady state, the average rate of entrainment is equal to the average rate of deposition. The details of entrainment, however, are not known, and it is therefore not clear what boundary conditions would best represent an actual annular flow. Two extreme possibilities for the boundary conditions are: (i) absorbing wall, and (ii) specular-reflecting wall. The first would represent a perfect absorbing wall without any re-entrainment, whereas the second would represent a local equilibrium between deposition and re-entrainment. In the simulations we only considered a specular-reflecting wall; particles maintain their axial and tangential momentum but reverse their radial momentum, when bouncing at the wall. Each collision with the wall is treated as a deposition event. Since the number of particles remains constant, it is easier to obtain meaningful statistical results with a specular-reflecting wall than with an absorbing wall. Note, however, that the specular

reflecting wall is a rather simplistic model, and that the situation in an actual annular flow can be quite complex.

Due to turbulence-particle interactions (i.e. turbophoresis, Young and Leeming (1997)), the particles are driven to the wall and tend to cluster there. The particles that are clustered near the wall, while sliding down forced by gravity, hit the wall frequently, Westende et al. (2004), and thus are a dominant factor concerning deposition in the simulations. In an actual annular flow, however, this is not the case, since the near-wall droplets are removed when depositing at the wall. In section 5.4.2, we show how to identify these sliding particles amongst the depositing particles. Since the sliding particles clustered near the wall have little interaction with the gas-phase turbulence, they are referred to as passive particles, whereas the active particles still interact with the turbulence of the gas.

All the simulations are done for an air-water system in a horizontal pipe with a diameter $D = 5$ cm. In every computation, the superficial gas-velocity, u_{sg} , was set to about 20 m/s, corresponding to a superficial gas-Reynolds number $Re_{sg} \approx 65,000$ ($\rho_g = 1$ kg/m³ and $\nu_g = 1.5 \cdot 10^{-5}$ m²/s). The magnitude of the secondary flow velocity, u_{sf} , is roughly equal to 0.2 m/s. The diameter of the secondary flow cells, D_{sf} , is about $D/2$, resulting in an centrifugal acceleration of about 4 m/s², which is of the same order of magnitude as the gravitational acceleration. We did simulations with two different particle diameters: $d_p = 50$ μ m and $d_p = 100$ μ m, for which the terminal free-fall velocity, $u_{p,t}$, is 0.09 m/s and 0.35 m/s, respectively; i.e., in both cases the terminal free-fall velocity is of the same order of magnitude as the secondary-flow velocity.

5.3 Simulations

We use Eulerian-Lagrangian LES with the standard point-particle approach, e.g. Portela and Oliemans (2003).

For the continuous phase, the gas velocity, \vec{u}_g , is simulated using a large-eddy simulation (LES). The filtered continuity and Navier-Stokes equations, that are solved for the gas-phase, are,

$$\vec{\nabla} \cdot \vec{u}_g = 0 \quad (5.1)$$

$$\frac{\partial \vec{u}_g}{\partial t} + \left(\vec{u}_g \cdot \vec{\nabla} \right) \vec{u}_g = -\frac{1}{\rho_g} \vec{\nabla} p + \nu_g \nabla^2 \vec{u}_g + \vec{\nabla} \cdot \vec{T}_s \quad (5.2)$$

with ρ_g and ν_g being the density and the kinematic viscosity of the gas-phase. The influence of the subgrid motion on the resolved gas-velocity is represented by the extra stress-tensor, \vec{T}_s . The in-house code that is used for the calculations solves eq. (5.1) and (5.2) using a finite-volume single-phase solver with a predictor-corrector method. In the predictor part, a leap-frog method, explicit in the radial and axial directions and implicit in the tangential direction, is used for progress in time. In the corrector step, the continuity equation is enforced using the Poisson equation for incompressible flows. The time-step is determined with the Courant criterion. The stress-tensor, \vec{T}_s , is computed using the standard Smagorinski model, with the Smagorinski constant $C_s = 0.1$. Van Driest wall-damping is also applied, with $c_A^+ = 25$. Throughout this paper, the superscript ⁺ is used when a quantity is normalised with ρ_g , ν_g and the friction velocity, u_τ . More details about the single-phase solver can be found in

Eggels (1994).

A staggered-grid in cylindrical coordinates is used and periodic boundary conditions are applied in the axial direction. In fig. 5.2, the computational domain with the corresponding position and velocity coordinates for the axial, tangential, and radial directions is drawn. For all the simulations, the gridpoints are uniformly distributed in the tangential and axial directions, with $N_\phi = N_z = 192$. The length of the computational domain in the axial direction is $L_z = 5D$. In the radial direction the grid is stretched, using a hyperbolic-tangent function,

$$r_i = \frac{\tanh(c_{r1}i/c_{r2})}{2 \tanh(c_{r1})} D \quad 0 < i < N_r \quad (5.3)$$

using the following constants: $N_r = 32$, $c_{r1} = 2.45$ and $c_{r2} = 40$. This grid has a wall-nearest grid-point at a distance from the wall, $y \approx D/68$, a grid-spacing near the wall, $\Delta y_w \approx D/350$, and a grid-spacing in the center $\Delta y_c \approx D/32$. Note that because we are using wall-functions, the first grid-point near the wall is located in the logarithmic layer, and is at a larger distance from the wall than the near-wall grid spacing.

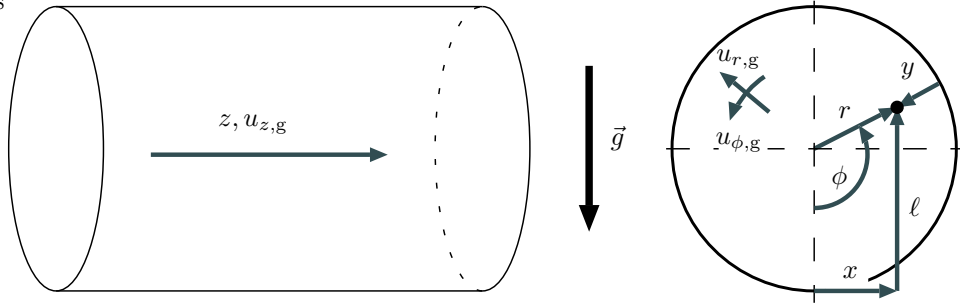


Figure 5.2: Computational domain, together with position and velocity coordinates.

In order to account for the wall-roughness, the Schumann wall-function is implemented for the near-wall region, $0 < y/D < 0.015$, Piomelli et al. (1989). The boundary conditions for the grid-cells near the wall (see fig. 5.3) are:

$$u_{r,g,N_r} = 0 \quad (5.4)$$

$$\tau_{r\phi,w} = -\rho_g \nu_g \frac{u_{\phi,g,N_r}}{y_{N_r}} \quad (5.5)$$

$$\tau_{rz,w} = -\rho_g u_\tau^2 \frac{u_{z,g,N_r}}{\langle u_{z,g,N_r} \rangle} \quad (5.6)$$

$$\langle u_{z,g,N_r} \rangle = \frac{u_\tau}{\kappa} \ln(y_{N_r}/k_{s,\text{eff}}) + 8.5 \quad (5.7)$$

$$k_{s,\text{eff}} = \max(k_s, k_{s,\text{min}}) \quad (5.8)$$

u_{r,g,N_r} , u_{ϕ,g,N_r} and u_{z,g,N_r} represent the instantaneous radial, tangential and axial velocities and $\langle u_{z,g,N_r} \rangle$ the average axial-velocity at the wall-nearest grid point. The two components

of the wall-shear are given by $\tau_{r\phi,\text{wall}}$ and $\tau_{rz,w}$. y_{N_r} is the distance to the wall for the wall-nearest grid-point, κ is the von Karman constant and $k_{s,\text{eff}}$ is the effective local wall-roughness. The effective local wall-roughness is equal to the actual local wall-roughness, k_s , but cannot be smaller than a minimum, $k_{s,\text{min}}$, thus forcing eq. 5.7 to match the smooth wall law of the wall for $k_s^+ \leq k_{s,\text{min}}^+ = \exp(3.5\kappa)$, Jimenez (2004).

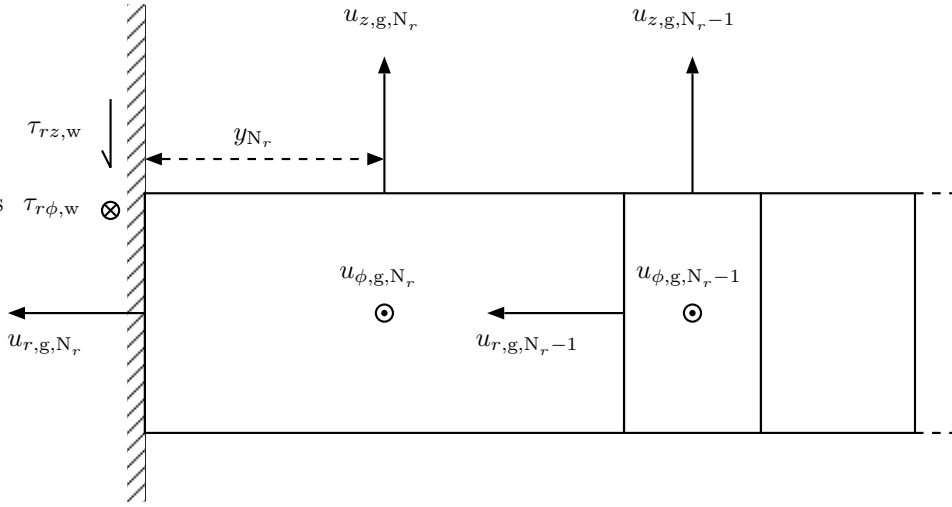


Figure 5.3: Wall-shear for wall-nearest grid-cell

The friction-velocity, u_τ , is calculated using the Fanning friction-factor, f , which is estimated with the Churchill relation, Churchill (1977).

$$u_\tau = u_{\text{sg}} \sqrt{f/2} \quad (5.9)$$

$$\frac{f}{2} = \sqrt[12]{\left(\frac{8}{\text{Re}_{\text{sg}}}\right)^{12} + \left(\left[2.457 \ln\left(\left(\frac{7}{\text{Re}_{\text{sg}}}\right)^{0.9} + 0.27 \frac{k_s}{D}\right)\right]^{16} + \left(\frac{37530}{\text{Re}_{\text{sg}}}\right)^{16}\right)^{-\frac{3}{2}}} \quad (5.10)$$

Re_{sg} is the Reynolds number based on u_{sg} and D . When the roughness is varied around the circumference, a local friction-factor is calculated for every tangential position, and the average of these local friction-factors is used in eq. (5.9). Three simulations were performed:

- F_{sm} : Uniform smooth-wall, $u_\tau = 0.99$ m/s, $\text{Re}_{\text{sg}} = 65,300$.
- F_{ro} : Uniform rough-wall, $k_s/D = 0.03$, $u_\tau = 1.58$ m/s, $\text{Re}_{\text{sg}} = 64,000$.
- F_{var} : Varying wall-roughness, $0 < k_s/D < 0.03$, $u_\tau = 1.34$ m/s, $\text{Re}_{\text{sg}} = 63,500$.

Simulations F_{sm} and F_{ro} are detailed and validated in appendix A, and simulation F_{var} is discussed in section 5.4.1.

The particles are treated as point-particles and are tracked individually using non-linear

drag and gravity. The drag coefficient used is

$$C_D = 24 \frac{\mu_g}{\rho_g |\vec{u}_g - \vec{u}_p| d_p} + 0.44 \quad (5.11)$$

which gives a good approximation of the standard drag curve, Govan (1989); with \vec{u}_p the instantaneous particle-velocity and d_p the particle-diameter. Using this drag coefficient, a terminal free-fall velocity in a stagnant medium, $u_{p,t}$, is calculated. In this paper, the particle-relaxation-time, τ_p , is defined as:

$$\tau_p = u_{p,t}/g \quad (5.12)$$

Similarly to the continuous-phase, periodic boundary conditions are also applied for the particles: when a particle leaves the domain, it is re-introduced with the same velocity at the opposite side. The particles progress in time is done with a second-order Adams-Bashforth method. According to Portela and Oliemans (2002), in our case the subgrid motion does not affect significantly the particle motion, since the time scales of the subgrid motion are much smaller than the particle-relaxation-time and the subgrid velocity fluctuations are much smaller than the grid-scale velocity fluctuations. Therefore, the influence of the subgrid-scales on the particle motion is neglected. Further details on the particle-tracking can be found in Portela and Oliemans (2003).

5.4 Results

5.4.1 Secondary flow

Darling and McManus (1968) measured secondary flow in a 10 cm diameter pipe with varying wall-roughness, using hot-wire anemometry. They used an air-flow at atmospheric conditions with superficial gas-velocity $u_{sg} = 13.4$ m/s, resulting in a Reynolds number of about 89,000. In their experiments, the bottom of the pipe had a hydraulic wall-roughness $k_s/D \approx 0.03$, decreasing gradually towards the top, where it becomes smooth. A secondary flow is then created such that a flow exists along the wall, from the rougher to the smoother region, and back through the center of the pipe, from the smooth wall to the rough wall, resulting in two big vortex-cells, as shown schematically in fig. 5.1c.

In the simulation F_{var} , the wall-roughness is varied around the circumference similarly to the experiments done by Darling and McManus, with

$$\frac{k_s}{D} = 0.015 (\cos(\phi) + 1) \quad (5.13)$$

Using this variation of roughness results in $u_\tau = 1.34$ m/s. In our simulations the wall-roughness is implemented using wall-functions, see appendix A for details.

In figure 5.4 the results of simulation F_{var} are shown, averaged in the axial direction and over 140 uncorrelated fields. Fig. 5.4a shows the mean axial-velocity, fig. 5.4b the magnitude of the secondary-flow velocity together with some streamlines, and fig. 5.4c the tangential-velocity fluctuation. Since the results are essentially symmetric with respect to the vertical axis, only half of the pipe is drawn.

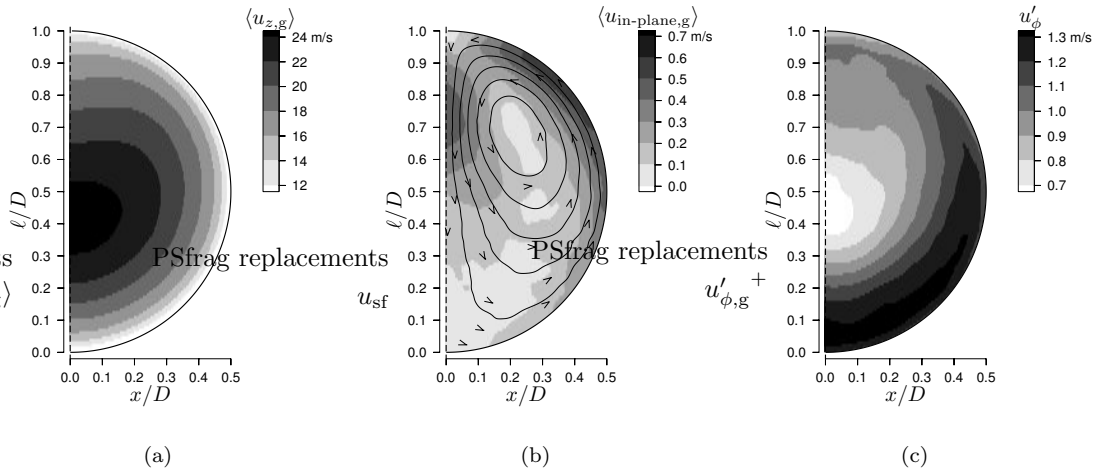


Figure 5.4: Contour plots of simulation F_{var} : (a) mean axial velocity, (b) secondary-flow strength with some streamlines, and (c) tangential-velocity fluctuation.

The maximum value of the mean axial-velocity is not in the center of the pipe, but is shifted towards the rough bottom. This is a result of the secondary flow (downwards through the center of the pipe), bringing axial-momentum from the center of the pipe to the bottom region. It thus seems as if the secondary flow ‘pushes’ the position of maximum axial-velocity downwards. In the literature, the presence and direction of secondary flow is usually shown via the mean axial-velocity profile. However, in general, there does not exist a one-to-one correspondence between the pattern of the secondary flow and the mean axial-velocity profile, Belt et al. (2005). In general, as shown, e.g., by Belt et al. (2004), the secondary flow is determined by the pattern of the Reynolds stresses in the cross-section of the pipe. In our case, the secondary flow consists of two symmetric cells with respect to the vertical axis, with a flow upward along the wall and downward through the center. At the bottom of the pipe the wall-shear and the Reynolds stresses are larger, fig 5.4c. As shown by Belt et al. (2004), the gradient in the tangential Reynolds-stress along the wall, shown in fig 5.4c, pushes the flow in the opposite direction (i.e., from the high towards the low values of $u'_{\phi,g}{}^+$), creating the secondary-flow pattern shown in fig. 5.4b.

According to Darling and McManus (1968), there is little or no Reynolds-number effect on the mean axial-velocity profile or the secondary-flow pattern, so their results can be compared with simulation F_{var} . The friction factor of F_{var} is only 4% larger than the value reported by Darling and McManus. This indicates that a circumferential-averaged friction factor seems to be a good way of determining the global friction factor; i.e. each roughness element contributes equally to the total wall-shear.

Darling and McManus found that the tangential component of the secondary flow reaches a maximum value of 7% of the local axial-velocity, at $\phi \approx 110^\circ$, very close to the wall ($y/D = 0.0065$). In the simulation F_{var} , the tangential component of the secondary flow reaches a

maximum value of 5.2% of the local axial-velocity, at $\phi \approx 130^\circ$, and also very close to the wall. Both the position and the magnitude of the maximum secondary-flow velocity of F_{var} are close to those of the experiments of Darling and McManus. Since it is very difficult to measure a small in-plane component of the gas-velocity very close to the wall, this might be a possible reason for the small differences. Another possible cause for the difference in the position and magnitude of the maximum secondary-flow velocity can be associated with the friction-velocity used in the simulations. In eq. 5.6 and eq. 5.7, we used the average friction-velocity instead of the local one. Implementing a local friction-velocity, will increase the wall-shear difference between the bottom and the top of the pipe, and therefore will generate a stronger secondary flow. However, the difference between the two implementations of the friction-factor (average or local) is small. Since we have not found detailed experiments that favor the use of a local friction-factor, we decided to use the average friction-factor in eq. 5.6 and eq. 5.7. Note that, even though the friction velocity is constant along the circumference, there exists a local variation of k_s , leading to a local variation of the wall-shear, which is the source of the secondary flow; in our case the friction velocity is a global effect associated with the pressure-gradient.

In fig. 5.5 we show the radial-velocity fluctuations on the vertical axis, for the simulation without secondary flow, F_{sm} , and the simulation with secondary flow, F_{var} . For both the simulations F_{sm} and F_{var} , there exists a minimum radial-Reynolds-stress in the center and near the wall, and maxima at $y/D \approx 0.1$. The effect of the wall-roughness is clearly visible from the magnitude of the radial-velocity fluctuation, and scales roughly with u_τ . For F_{var} the radial-velocity fluctuations are larger at the bottom where the wall-roughness is larger.

The strong gradients in the radial turbulence-intensity near the wall lead to the turbophoresis effect, Young and Leeming (1997). A balance of momentum in the radial direction shows that a gradient in the radial-velocity fluctuation of the particles results in a net force in the opposite direction. Since the velocity fluctuation of the particles is determined by the velocity fluctuation of the gas, the gradient in the radial turbulence-intensity pushes the particles towards the wall (turbophoresis). This effect is balanced by the diffusion associated with a gradient in the particle-concentration, and it leads to a high particle-concentration near the wall, Portela et al. (2002). In general, turbophoresis pushes particles towards regions of low turbulence-intensity (i.e. towards the walls), and when the particles reach the wall they cannot, on average, acquire enough energy to go back to a higher turbulence-intensity region, leading to a clustering of the particles near the wall.

For F_{var} the radial gradient of the radial-Reynolds-stress is larger at the bottom (largest wall-roughness), thus we expect turbophoresis to be stronger at the bottom than at the top. Also, at the bottom, gravity and turbophoresis are working in the same direction, while at the top they are counter-acting, making wall-clustering weaker at the top.

5.4.2 Particle-laden flow

We used spherical particles with a diameter of either 50 μm or 100 μm and a density of 1000 kg/m^3 , simulating water drops in air. The size is chosen such that the free-fall velocity of the particles in air is of the same order of magnitude of the secondary-flow velocity in the simulation F_{var} ($u_{\text{p,t},50\mu\text{m}} = 0.090$ m/s, $u_{\text{p,t},100\mu\text{m}} = 0.348$ m/s and $u_{\text{sf}} \approx 0.2$ m/s, fig. 5.4b). The gravitational acceleration is set to 9.81 m/s^2 . At the start of the computation 800,000

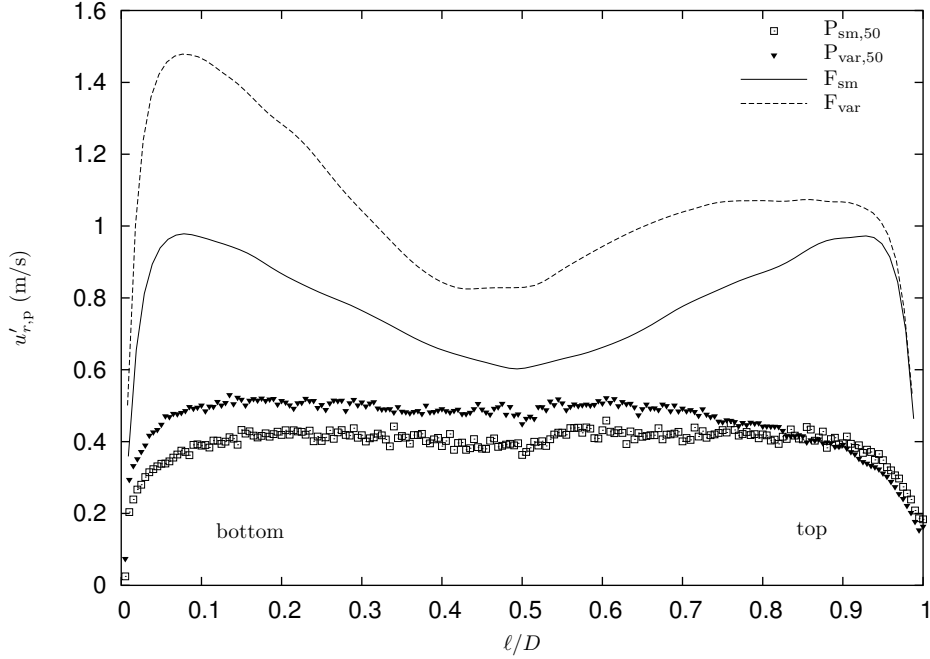


Figure 5.5: Radial-velocity fluctuations at the vertical axis, for the simulations with and without secondary flow. The lines (F_{sm} and F_{var}) represent the values for the gas-phase and the symbols ($P_{sm,50}$ and $P_{var,50}$) the values for the $50 \mu\text{m}$ particles (the particles are discussed in section 5.4.2).

particles were homogeneously distributed in the pipe (corresponding to a mean concentration of $1.63 \cdot 10^9 \text{ m}^{-3}$), with zero slip-velocity. Four cases were considered:

- $P_{sm,50}$: $50 \mu\text{m}$ particles in a flow field with a smooth wall (F_{sm})
- $P_{var,50}$: $50 \mu\text{m}$ particles in a flow field with a varying wall-roughness (F_{var})
- $P_{sm,100}$: $100 \mu\text{m}$ particles in a flow field with a smooth wall (F_{sm})
- $P_{var,100}$: $100 \mu\text{m}$ particles in a flow field with a varying wall-roughness (F_{var})

Fig. 5.6 and fig. 5.7 show some snapshots of the particle-distribution of the simulations $P_{sm,50}$ and $P_{var,50}$, respectively, for three instants in time: $t = 0$, $t = 0.5D/u_{p,t,50\mu\text{m}}$ and $t = D/u_{p,t,50\mu\text{m}}$. $D/u_{p,t,50\mu\text{m}}$ is roughly the time that would take for all the particles to deposit, if they would be moving in a stagnant medium. Both fig. 5.6 and fig. 5.7 show the rapid particle-depletion of the core region and the strong particle-accumulation at the wall. However, the particle concentration in the center of the pipe is larger for simulation $P_{var,50}$ than for simulation $P_{sm,50}$. Especially at the top region of the pipe, the secondary flow tends to mix the particles back into the core. The snapshots of the simulations $P_{sm,100}$ and $P_{var,100}$ are not shown here, since they show roughly the same trends.

Since in our simulations we are using a specular-reflecting wall, the particles do not actually deposit, but they bounce at the wall. When a particle hits the wall and bounces, this is

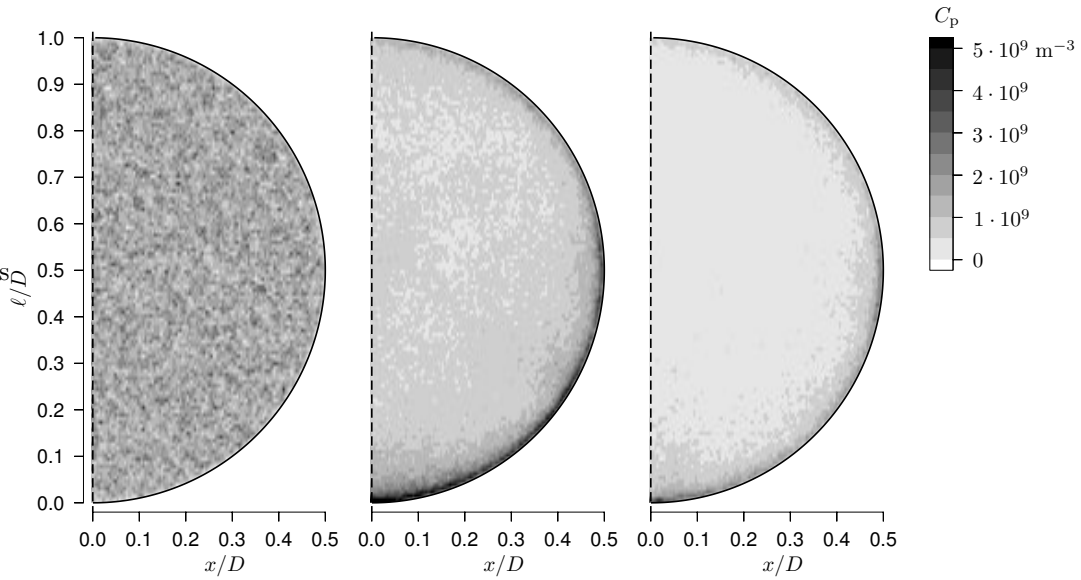


Figure 5.6: Snapshots of particle-distribution in the pipe, for simulation $P_{sm,50}$, at three instants in time: $t = 0$, $t = 0.5D/u_{p,t,50\mu m}$ and $t = D/u_{p,t,50\mu m}$.

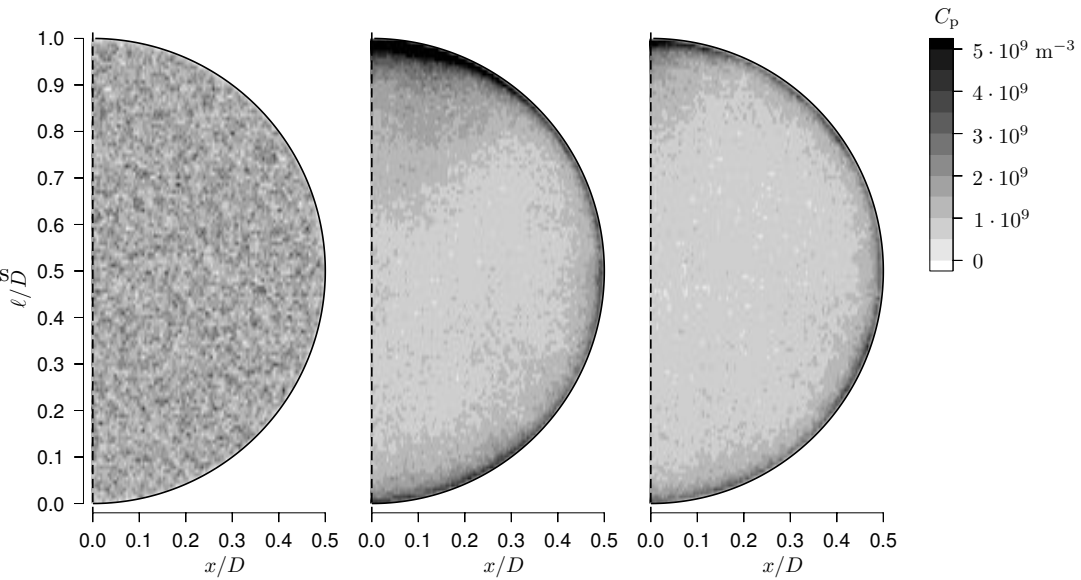


Figure 5.7: Snapshots of particle-distribution in the pipe, for simulation $P_{var,50}$, at three instants in time: $t = 0$, $t = 0.5D/u_{p,t,50\mu m}$ and $t = D/u_{p,t,50\mu m}$.

treated as a single deposition-event. The results of the simulations show that the deposition-events can be divided into two different classes: (i) with active particles, and (ii) with passive particles. The active particles are distributed throughout the pipe-volume and are in approximate equilibrium with the turbulence of the gas-phase. In contrast, the passive particles are concentrated in an ‘accumulation region’ close to the wall, due to turbophoresis, and they do not ‘feel’ the turbulence.

The results of the radial velocity of the particles, shown in fig. 5.8, suggest that the accumulation-region can be defined as $y < D/200$. The active particles must have large radial-velocities, in order to be able to escape the accumulation-region after bouncing with the wall. On the other hand, the passive particles have small radial-velocities and cannot escape the accumulation-region after bouncing with the wall (in essence, turbophoresis keeps them near the wall). In fig. 5.8 we show the distribution of the positive radial-velocity of all the particles (both passive and active), for $P_{sm,50}$ at $t = 0.5D/u_{p,t,50\mu m}$, separated into three different regions: the accumulation-region ($y < D/200$), the ‘mid’-region ($D/200 < y < D/100$) and the core-region ($y > D/100$). The radial-velocity distribution for the accumulation-region shows

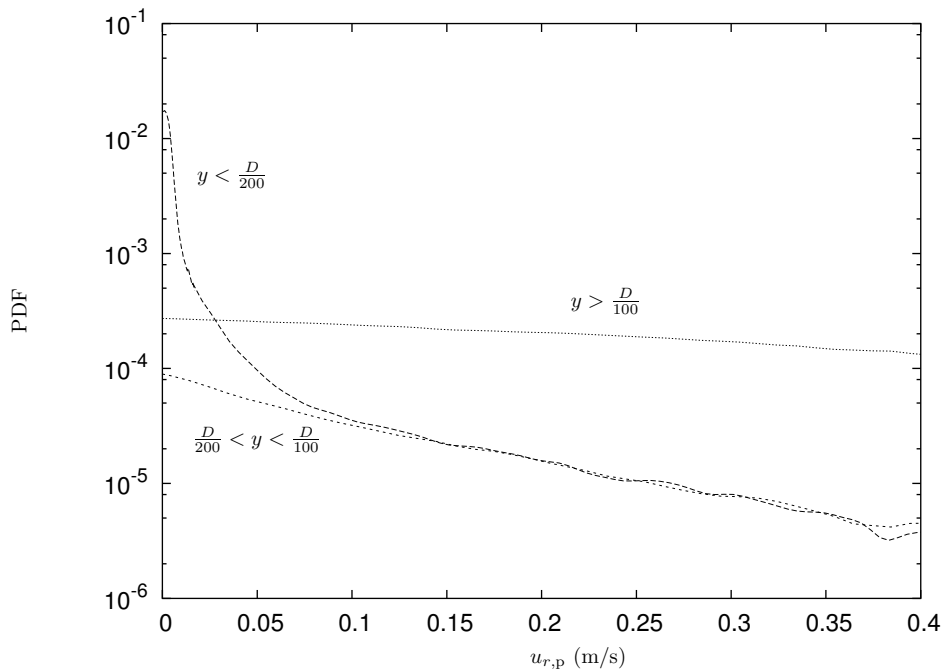


Figure 5.8: Distribution of the positive radial-velocity of the particles in the accumulation-region ($y < D/200$), the ‘mid’-region ($D/200 < y < D/100$), and the core-region ($y > D/100$), for $P_{sm,50}$ at $t = 0.5D/u_{p,t,50\mu m}$.

a pronounced peak at small radial-velocities, which is absent in the mid and core regions. For radial-velocities larger than about 0.1 m/s, the distribution for the accumulation-region and the mid-region are similar. This indicates that the passive particles, with small radial-velocities, are located in the accumulation-region. Therefore, we define the deposition-events

by passive particles as those for which the impact-velocity is below a threshold-velocity, $u_{r,p,dep,min} = 0.1$ m/s.

During the simulation, particles originally in the active class become trapped near the wall, and then belong to the passive class; turbophoresis may be the major contributor to this process. Since the passive particles are not expected to be representative for the dispersed phase of an actual annular flow, we are interested in the active particles only. The concentration of the active particles, C , decreases during the simulation, therefore, so does their rate of deposition at the wall, R_{dep} . However, a quasi-steady situation is reached, in the sense that the deposition constant, $k_{dep} = R_{dep}/C$, does not change in time and the rate of deposition becomes proportional to the concentration of active particles, leading to an exponential-decay in the number of active particles. From fig. 5.9, we see that for $t \gtrsim 0.25D/u_{p,t}$ there exists a large interval of time during which this quasi-steady situation is occurring. Further results on snapshots are presented for a particular time during this interval ($t = 0.5D/u_{p,t}$) where the quasi-steady situation is already well-established and the concentration of active particles is still high.

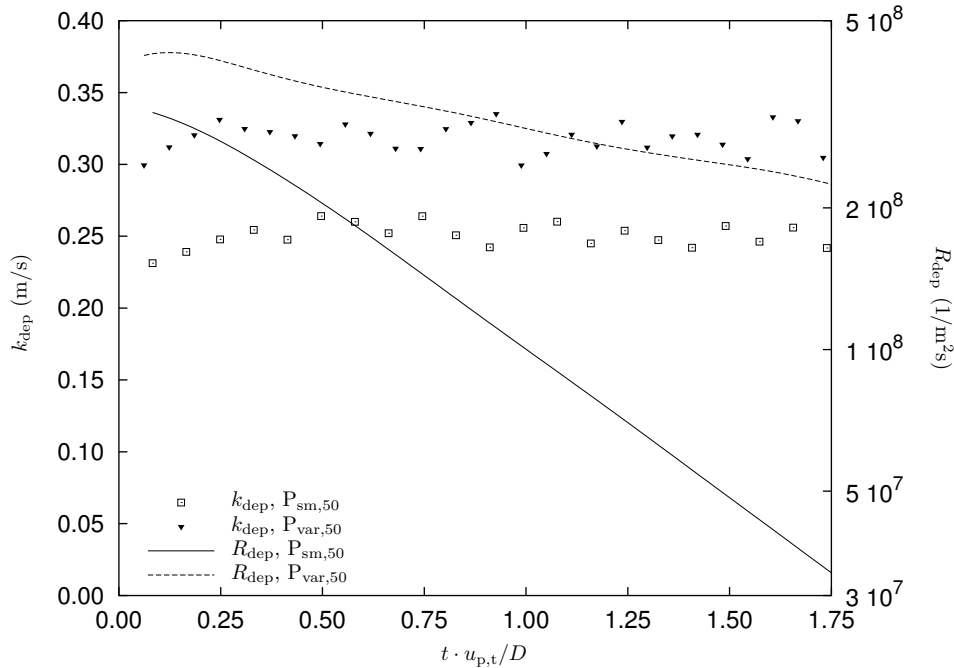


Figure 5.9: Evolution in time of the deposition-constant and the rate of deposition at the wall, for $P_{sm,50}$ and $P_{var,50}$ (average values over the wall).

Figure 5.10 shows the concentration profile of the active particles on the vertical axis, $x = 0$ (lines), and near the wall, $y = 0.05D$ (symbols), for $P_{sm,50}$ and $P_{var,50}$, at $t = 0.5D/u_{p,t}$. For $P_{sm,50}$, the concentration in the center of the pipe, $0.2 < \ell/D < 0.8$, decreases roughly exponentially with the vertical distance to the bottom, due to gravitational settling; i.e., a

classical Rouse profile is found: $C \propto C_b \exp(-\beta\ell)$ with $\beta = 0.7$ as a fit parameter. Turbophoresis plays a dominant role near the wall, $y < 0.1D$, and causes the strong increase of concentration in this region; the concentration near the wall (symbols) is in general larger than the bulk concentration. We observe the particle-concentration in a horizontal plane, i.e. at a given value of ℓ , to be fairly constant in the center of the pipe, corresponding to a Rouse-profile.

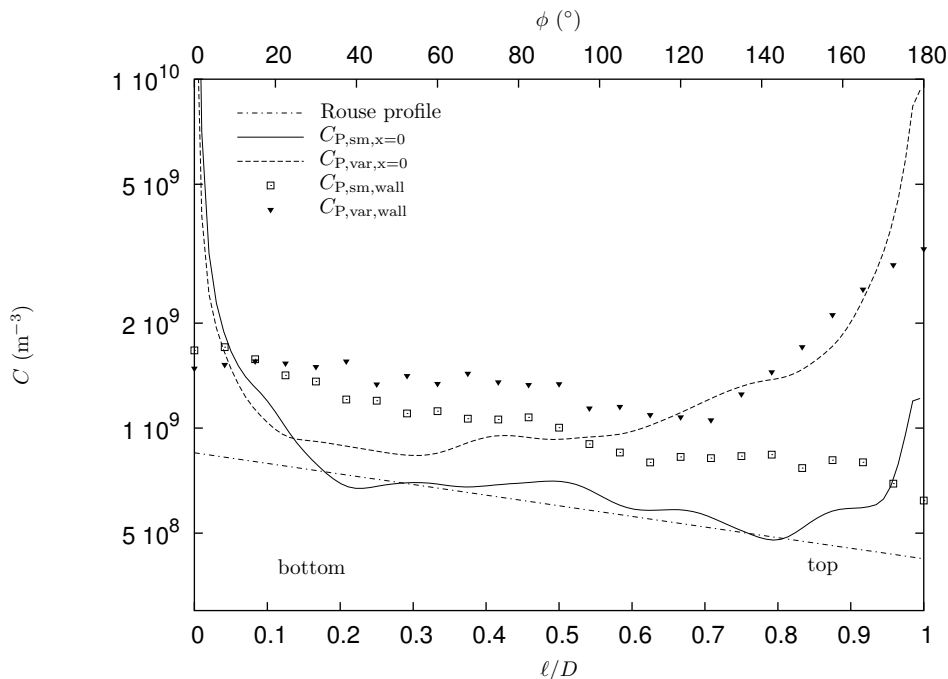


Figure 5.10: Concentration profile of the active particles along the vertical axis, $x = 0$ (lines), as a function of the vertical distance to the bottom wall, ℓ (bottom axis), for $P_{sm,50}$ and $P_{var,50}$, at $t = 0.5D/u_{p,t,50\mu m}$. The dash-dotted line is a fit of a Rouse-profile to $P_{sm,50}$. The concentration near the wall, $y = 0.05D$ (symbols), is plotted as a function of the angle, ϕ (top axis). Since the results of $P_{sm,50}$ and $P_{var,50}$ are shown as a snapshot, the exact value of the concentration of the different simulations should not be compared directly.

The concentration of the active particles for simulation $P_{var,50}$ is larger than for $P_{sm,50}$, this difference becoming more pronounced with time, as can be seen in fig. 5.6 and fig. 5.7. A possible cause is that secondary flow is able to increase the velocity with which the particles impact at the wall, thus making the transition of a particle from the active to the passive class more difficult, so the concentration of active particles remains higher. Also, the secondary flow tends to ‘mix’ the particles more efficiently from the near-wall region into the core of the pipe, therefore increasing the number of active particles in the core of the pipe for $P_{var,50}$. The combination of a large concentration of active particles at the top-wall, and an effective transport of particles from the top-wall to the bottom wall through the center, by secondary flow, tends to increase the concentration at the top-half of the pipe, resulting in a plume-like

concentration-pattern in the top region of the pipe, fig. 5.7. This mixing-effect destroys the Rouse-profile for simulation $P_{\text{var},50}$; the particle-concentration profile is more uniform, and even slightly increasing with ℓ in the center of the pipe, fig. 5.10. The near-wall concentration of $P_{\text{var},50}$, however, shows a remarkable inflection at $\phi = 130^\circ$. The position of the inflection appears to be linked with the maximum magnitude of the secondary-flow velocity, and the sweeping of the particles by the centrifugal effects of the secondary-flow cells (fig. 5.4b). The turbophoresis effect is present as well, shown by the strong increase in the concentration near the wall.

The concentration profile of the active particles in the pipe, especially the near-wall concentration, has a strong impact on the deposition-rate along the wall. In figure 5.11 we plot the local rate-of-deposition of the active particles, for $P_{\text{sm},50}$ and $P_{\text{var},50}$, at $t = 0.5D/u_{p,t}$. The deposition-rate of simulation $P_{\text{sm},50}$ is larger at the bottom-wall than at the top-wall, mainly due to the differences in particle-concentration. Since the average concentration for $P_{\text{var},50}$ is larger than for $P_{\text{sm},50}$, the average particle-deposition-rate is larger as well. For $P_{\text{var},50}$, the deposition-rate along the circumference, going from the bottom to the top of the tube, shows a smaller decrease than for $P_{\text{sm},50}$. In simulation $P_{\text{var},50}$, for $\phi \gtrsim 130^\circ$ the deposition-rate shows an abrupt increase, similarly to the near-wall concentration.

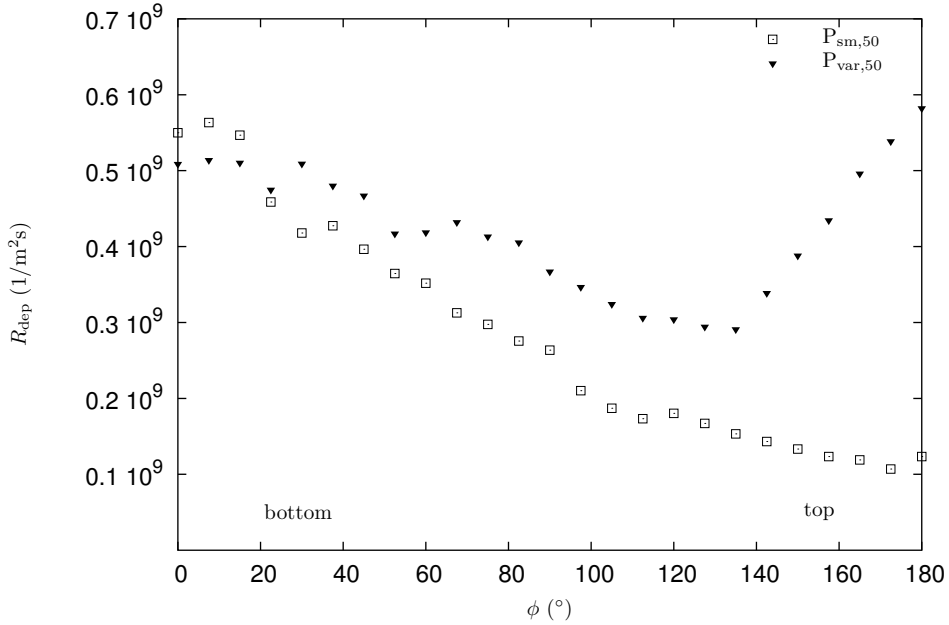


Figure 5.11: Local rate-of-deposition, R_{dep} , of the active particles, for simulations $P_{\text{sm},50}$ and $P_{\text{var},50}$, at $t = 0.5D/u_{p,t}$.

Free-Flight Model

Besides the concentration of the active particles, the deposition ‘constant’ is also an important factor in the rate of deposition, $R_{\text{dep}} = k_{\text{dep}}C$. Due to the circumferential variation of the radial-component of gravity, the deposition ‘constant’ varies as well. We consider here that k_{dep} depends only on the turbulence and gravity, and use the free-flight model of Pan and Hanratty (2002) to understand the variation of k_{dep} along the circumference. Note that, even though the turbophoresis effect is present in our simulations, their model does not explicitly use this mechanism, but it uses the average effect of the turbulence.

First, we discuss briefly their model, in which secondary flow is not considered, and compare it with the simulations. The parameters of their model can be estimated using submodels for C_D (eq. 5.11) and for σ_p , or can be viewed as tuning parameters for a parameter-fit of the results of the simulation to the model. The parameters of the model of Pan and Hanratty obtained by the parameter-fit are indicated with the superscript *.

In the model of Pan and Hanratty, it is assumed that all depositing particles start a free-flight to the wall from outside the viscous wall-layer. The radial-velocity distribution of the particles at the position where free-flight begins is assumed Gaussian, with a mean value equal to the terminal free-fall velocity projected onto the wall-normal, and a standard deviation σ_p ; i.e., the PDF of the radial-velocity of the particles is assumed equal to:

$$\text{PDF}(u_{r,p}) \propto \exp\left(-\frac{1}{2}(u_{r,p} - u_{p,t} \cos(\phi))^2 / \sigma_p^2\right) \quad (5.14)$$

The local deposition-constant then becomes:

$$k_{\text{dep}}(\alpha) = \int_0^\infty u_{r,p} \text{PDF}(u_{r,p}) du_{r,p} = \frac{\sigma_p}{\sqrt{2\pi}} [\exp(-\alpha^2) + \sqrt{\pi}\alpha (1 + \text{erf}(\alpha))] \quad (5.15)$$

$$\alpha = \frac{u_{p,t} \cos(\phi)}{\sqrt{2}\sigma_p} \quad (5.16)$$

The variation of k_{dep} along the pipe circumference is thus determined only by the ratio of the terminal free-fall-velocity and the velocity fluctuations of the particles (given by σ_p); this is shown in fig. 5.12. For $u_{p,t}/\sigma_p \gtrsim 3$, the deposition is dominated by gravity, $\langle k_{\text{dep}} \rangle_\phi = u_{p,t}/\pi$. For $u_{p,t}/\sigma_p \lesssim 0.1$, the deposition is dominated by the turbulence, $\langle k_{\text{dep}} \rangle_\phi = \sigma_p/\sqrt{2\pi}$. For $0.1 \lesssim u_{p,t}/\sigma_p \lesssim 3.0$, there exists a competition between turbulence-deposition and gravitational-deposition.

Pan and Hanratty also assumed that the turbulence-intensity of the particles is equal throughout the whole pipe and that the dispersed phase is in equilibrium with the continuous phase, they assumed:

$$\sigma_p^2 = \left(\frac{1}{1 + 0.7\tau_p/\mathcal{T}} \right) (0.9u_\tau)^2 \quad (5.17)$$

$$\mathcal{T} = 0.046D/u_\tau \quad (5.18)$$

where \mathcal{T} is the Lagrangian time-constant characterising the gas-phase turbulence.

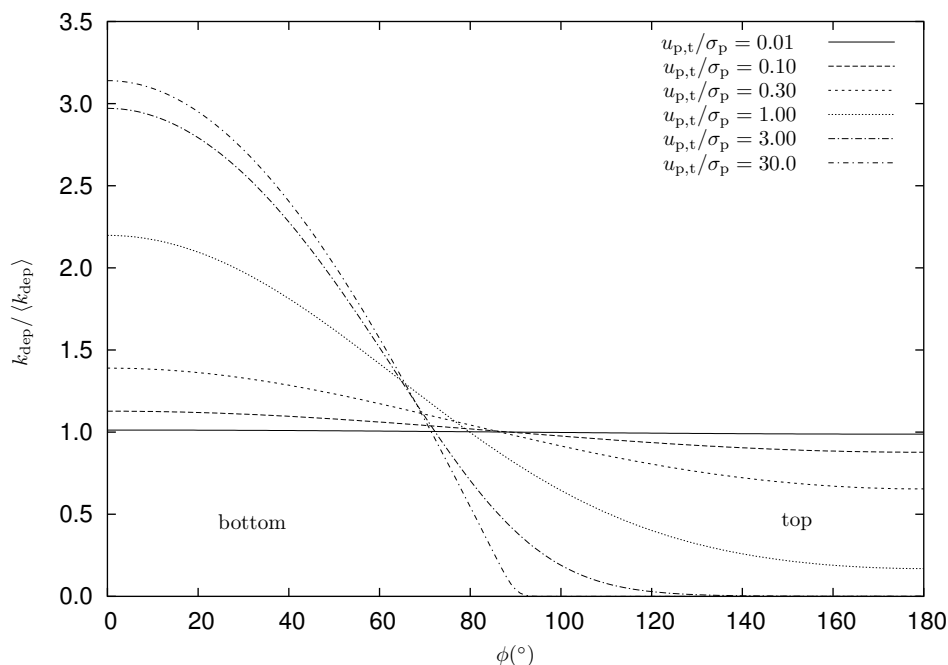


Figure 5.12: Variation of the deposition ‘constant’ along the pipe circumference in a horizontal pipe, normalised with the mean deposition-constant, $\langle k_{\text{dep}} \rangle$, according to Pan and Hanratty (2002).

Effect of Secondary Flow

We adopt the same approach and assume a single value for the gas-phase turbulence intensity for the whole flow field (i.e. we do not take into account the velocity-fluctuation change along the circumference due to the variation in wall-roughness).

Using the results of our simulation, the evaluation of $k_{\text{dep}} = R_{\text{dep}}/C$ can be done using the rate of deposition at the wall and the concentration. The deposition rate of the active particles at a given time is computed by averaging over a time-span of 10^{-2} s. The threshold velocity, $u_{r,p,\text{dep},\text{min}} = 0.1$ m/s, is used to distinguish the active from the passive depositing particles.

The concentration that we use for computing k_{dep} is the free-flight concentration, C_{ff} , taken at the position where the active particles start their free-flight, y_{ff} . Note that, even though for all the deposition events the radial-velocity is positive, for the computation of the free-flight concentration, we use particles with both positive and negative radial-velocities.

In the central region of the pipe, the magnitude of the radial-velocity fluctuation of the active particles is roughly uniform. Near the wall, the gradient in the radial-velocity fluctuation of the continuous-phase is very steep, leading to a steep decrease in the radial-velocity fluctuation of the active particles. From fig. 5.5, it appears that for $P_{\text{sm},50}$ the near-wall decrease in the radial-velocity fluctuation of the active particles starts at $y/D = 0.05$ ($y^+ = 165$), which coincides, roughly, with the position of the maximum radial-velocity fluctuation of the continuous-

phase. Here, we define the wall-distance where the free-flight starts as $y_{\text{ff}}/D = 0.05$, since the gradient in the radial-velocity fluctuation of the continuous-phase becomes very large closer to the wall, and the particles are not in equilibrium with the turbulence anymore (free-flight). The free-flight concentration thus becomes: $C_{\text{ff}} = C_{y/D=0.05}$. Since the near-wall decrease in the radial-velocity fluctuation of the active particles starts also at approximately the same location for $P_{\text{var},50}$, $P_{\text{sm},100}$ and $P_{\text{var},100}$, we use the same definition for y_{ff} and C_{ff} for all the simulations.

For $P_{\text{sm},50}$, we estimate the radial-velocity fluctuation of the active particles, σ_p^* , using fig. 5.5 and taking the average value for $y/D > 0.1$. We determine the mean deposition-constant, $\langle k_{\text{dep}}^* \rangle$, using fig. 5.9 and taking the average value for $0.3D/u_\tau \lesssim t \lesssim 1.2D/u_\tau$. Then, the k_{dep} -curve (eq. 5.15) is fitted to the local deposition-constant, normalised with the mean deposition-constant, and the tuning parameter $u_{p,t}^*/\sigma_p^*$ is adjusted in order to get the ‘best-fit’ (least squares). The result is shown in fig. 5.13. With the estimate of σ_p^* and $u_{p,t}^*/\sigma_p^*$, we determine the free-fall velocity, $u_{p,t}^*$. Note that, contrary to $u_{p,t}$, $u_{p,t}^*$ is not a property of the particles; it is a best-fit tuning-parameter for the model of Pan and Hanratty. For the other simulations we used a similar procedure. The results of the fit are given in table 5.1.

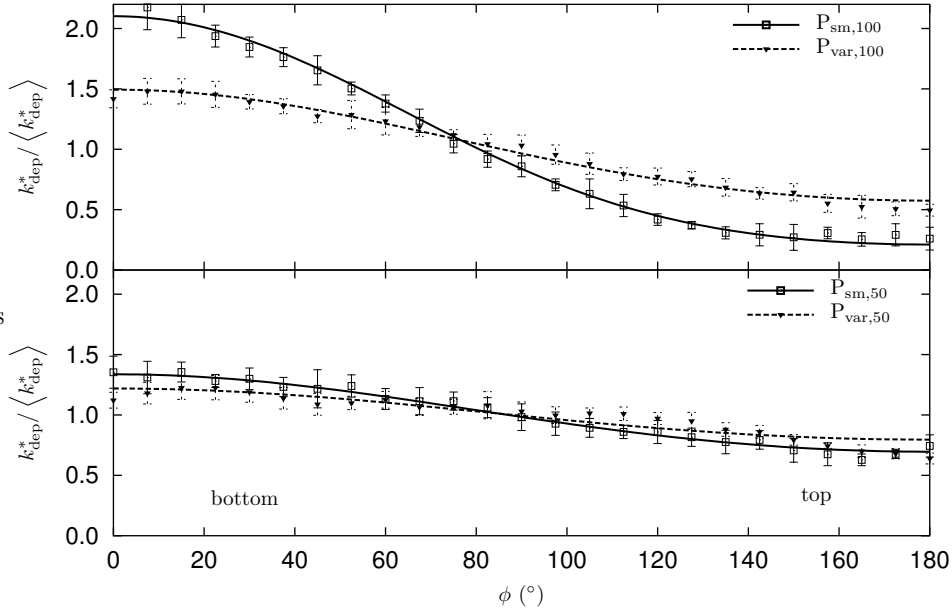


Figure 5.13: Local deposition-constant normalised with the mean deposition-constant for simulations $P_{\text{sm},50}$, $P_{\text{var},50}$, $P_{\text{sm},100}$ and $P_{\text{var},100}$, using the fit parameters from table 5.1. The averaging over multiple uncorrelated fields provides the mean (symbols) and the standard deviation (“error-bars”) of the local deposition-constant.

From fig. 5.13 we observe that the fitted deposition constant, k_{dep}^* , becomes more uniform

	Model				Fit			
	$u_{p,t}$ (m/s)	σ_p (m/s)	$u_{p,t}/\sigma_p$	$\langle k_{\text{dep}} \rangle$ (m/s)	$\langle k_{\text{dep}}^* \rangle$ (m/s)	$u_{p,t}^*/\sigma_p^*$	σ_p^* (m/s)	$u_{p,t}^*$ (m/s)
P _{sm,50}	0.09	0.46	0.20	0.19	0.25	0.26	0.41	0.11
P _{var,50}	0.09	0.55	0.16	0.22	0.32	0.17	0.48	0.08
P _{sm,100}	0.35	0.26	1.34	0.15	0.19	0.90	0.24	0.22
P _{var,100}	0.35	0.31	1.14	0.16	0.20	0.38	0.28	0.11

Table 5.1: General results for all the simulations. Columns 2 to 5 are calculated using the model of Pan and Hanratty (2002). Column 6 to 9 are parameter-fits of the results of the simulations to the model.

(smaller $u_{p,t}^*/\sigma_p^*$) when secondary-flow is present. Since k_{dep}^* is already quite uniform for P_{sm,50}, the effect is less pronounced for the simulations with the 50 μm particles. It should be noted that for $u_{p,t}^*/\sigma_p^* > 3$ or $u_{p,t}^*/\sigma_p^* < 0.1$ the fit of eq. 5.15 becomes more difficult, since the shape of the curve hardly changes with $u_{p,t}/\sigma_p$; see fig. 5.12.

From table 5.1, we see that the model of Pan and Hanratty underestimates the deposition-constant for all the simulations; the largest discrepancy being with the 50 μm particles. Still, their model is able to give a reasonable prediction of the deposition-constant, and correctly predicts that the 50 μm particles have a larger deposition-constant than the 100 μm particles. Probably, the most important cause for the difference in $\langle k_{\text{dep}} \rangle$ between the model and the fit of the simulations is the determination of the free-flight concentration. Taking a start-position of free-flight, y_{ff} , too far away from the wall, results in a too small free-flight concentration, C_{ff} , since concentration decreases with distance from the wall. Hence the deposition constant will be overestimated. It thus seems that y_{ff} should be smaller than $0.05D$, since this will increase C_{ff} , and thus decrease $\langle k_{\text{dep}}^* \rangle$. The difficulty in evaluating C_{ff} is a general problem of free-flight models. In the literature, the wall-distance where free-flight starts (stopping distance), usually is defined as, Friedlander and Johnstone (1957):

$$y_{\text{ff}} = u_{r,p,\text{ff}}\tau_p \quad (5.19)$$

where $u_{r,p,\text{ff}}$ is a characteristic velocity of the particles moving towards the wall. The average positive-radial-velocity in P_{sm,50} is equal to 0.5 m/s. Using this value for $u_{r,p,\text{ff}}$ would result in $y_{\text{ff}}/D = 0.09$; i.e., y_{ff} would be larger than the value we used, leading to an even larger value of $\langle k_{\text{dep}}^* \rangle$

From fig. 5.5, we see that the magnitude of the radial-velocity fluctuation of the particles is fairly constant in the central region of the pipe; it only decreases near the wall. In the central region of the pipe, the radial-velocity fluctuation of the particles is in approximate equilibrium with the turbulence intensity of the gas-phase, as assumed in the model of Pan and Hanratty. However, the model of Pan and Hanratty (eq. 5.17) overpredicts the radial-velocity fluctuation of the particles by about 10% for all the simulations. The overprediction of σ_p has two effects (see eq. 5.15): (i) by itself leads to an overall increase in k_{dep} , and (ii) combined with $u_{p,t}$ promotes a change in α , leading to a change in the variation of k_{dep} along the wall.

Nevertheless, the model of Pan and Hanratty predicts correctly the enhanced deposition at

the bottom due to the gravity, and shows that this effect is stronger for the larger particles. Moreover, the variation of the deposition-rate along the wall can be well-fitted with the model. However, the fitting-parameter $u_{p,t}^*/\sigma_p^*$ differs from the value of $u_{p,t}/\sigma_p$. For the 50 μm particles $u_{p,t}^*/\sigma_p^*$ is higher than $u_{p,t}/\sigma_p$, whereas for the 100 μm particles it is lower. The value of $u_{p,t}^*$ obtained from the fitting of the model to the results of the simulations is quite different from $u_{p,t}$, which is the terminal free-fall velocity of the particles in a stagnant medium. It is well known that the fall velocity of particles in a turbulent medium differs from the free-fall velocity in a stagnant medium (e.g. Davila and Hunt (2001)). Therefore, the model could be improved by considering the effect of the turbulence on the free-fall velocity of the particles.

The simulations with secondary flow have a variable wall-roughness and thus the turbulence intensity is larger. Due to the larger turbulence intensity, the radial-velocity fluctuation of the particles and the deposition-constant are larger. Also, with the increased turbulence intensity the gravitational contribution to the deposition becomes less dominant, resulting in a more uniform deposition along the wall. The model of Pan and Hanratty is able to predict the effects due to the larger turbulence intensity. For both the 50 μm and the 100 μm particles, the radial-velocity fluctuation of the particles is about 20% larger for the simulations with a variable wall-roughness than for the simulations with a smooth wall, and this is well predicted by the model; i.e., for both particle-diameters, σ_p and σ_p^* are about 20% larger with secondary flow. Therefore, the presence of secondary flow by itself does not seem to have a large influence on the radial-velocity fluctuation of the particles. The increase in the radial-velocity fluctuation of the particles appears to be mostly due to the increase in the turbulence intensity associated with the wall-roughness present in the secondary flow simulations. The more uniform deposition along the wall promoted by a larger turbulence intensity is also taken into account by the model of Pan and Hanratty, through the decrease in $u_{p,t}^*/\sigma_p^*$ promoted by the increase in σ_p^* .

However, the value of $u_{p,t}^*/\sigma_p^*$ that follows from the fit of the simulations is much smaller than the value that results from the increase in σ_p^* . Apparently, the secondary flow promotes a decrease in the terminal free-fall velocity of the particles, $u_{p,t}^*$, along the wall, and this decrease leads to a much smaller value of $u_{p,t}^*/\sigma_p^*$. Especially for the 100 μm particles, the effect of the secondary flow on the terminal free-fall velocity is quite dramatic: the value of $u_{p,t}^*$ with secondary flow is half the value of $u_{p,t}^*$ without it. A smaller terminal free-fall velocity results in a weaker gravitational settling, keeping the particles in the core of the pipe for a longer time, which leads to a larger particle-concentration, fig. 5.10, and a larger rate of deposition, fig. 5.11. Also, with a weaker gravitational settling the deposition becomes more uniform along the wall, fig. 5.13. Clearly, an important improvement in the model of Pan and Hanratty would be to include the effect of the secondary flow on the fall-velocity of the particles.

Also the inclusion of circumferential variation of the gas-phase turbulence and the effects of turbophoresis may improve the model to describe the simulations. It should be noted that in an actual annular flow the effect of turbophoresis might be less strong than in the present simulations. In our simulations the particles remain entrained by the turbulence. In an actual annular flow the particles (droplets) deposit in the film and are ejected with a velocity that is not necessarily related with the local turbulence. Therefore, the turbulence has a smaller role in determining the near-wall behaviour of the particles, which might lead to a weakening

of the turbophoresis effect. A possible way of including this effect is to use more realistic boundary conditions.

5.5 Conclusion

In this paper, a horizontal annular dispersed pipe flow is simulated using LES, with air and water being the gas and liquid phases. The turbulent gas-core is solved with an in-house code, using a bulk velocity of 20 m/s and a pipe diameter of 5 cm. The thin liquid-film is modeled as a cylindrical wall with a varying wall-roughness; the bottom-wall being rough, $k_s/D = 0.03$, and the top-wall of the pipe being smooth, $k_s/D = 0$. The dispersed phase is simulated using a monodispersion of solid spheres, with a diameter of either 50 μm or 100 μm , driven by drag and gravity. Besides simulations with a varying wall-roughness, we also perform simulations with uniform roughness and with a smooth wall.

In modeling wall-roughness in turbulent single phase pipe flow, it is shown that the Schumann wall-function can be used: the law of the wall is well-resolved and there is good agreement with experiments from the literature. When the roughness is varied around the pipe wall, the pressure drop is well-predicted by averaging the friction-factor over the wall, so that every roughness-element contributes equally to the total wall-shear; also, the secondary-flow pattern agrees well with the measurements from Darling and McManus (1968).

In horizontal particle-laden pipe flows the particles are pushed towards the wall by the turbophoresis and towards the bottom by the gravity. This leads to a quick depletion of particles (droplets) in the core of the pipe. Our results indicate that the secondary flow induced by the variable film-thickness can have a large effect on the particle distribution and their deposition at the wall. The major global effect of the secondary flow is to bring the particles from the wall region to the core of the pipe, and, in particular, to the top part of the pipe. This increase in the particle-concentration in the core and top of the pipe leads to an overall increase in the rate of the deposition of the particles, which also becomes more uniform over the wall-circumference, with the rate of deposition at the top becoming of the same order of magnitude as the rate of deposition at the bottom. Besides this major global effect on the particle-concentration, the secondary flow induced by the variable wall-roughness can also promote changes in the deposition mechanisms themselves:

- (i) Along the wall the secondary flow and gravitational settling act in opposite direction, therefore the presence of secondary flow reduces the relative importance of the settling with respect to the turbulence, making the deposition rate more uniform.
- (ii) The wall-roughness leads to an increase in the overall turbulence intensity, increasing the overall deposition rate (due to an increase in the turbophoresis effect).
- (iii) Due to the centrifugal effect of the secondary flow, the particles tend to be swept towards the wall, which can lead to a local increase in the rate of deposition in regions where the secondary flow velocity is larger.

All these changes in the deposition mechanisms are present and can play a significant role. However, our results indicate that the major effect of the secondary flow is through its influence on the redistribution of the particle-concentration.

The model of Pan and Hanratty (2002), based on the free-flight concept was used to fit the results of the deposition ‘constant’. To compute the deposition ‘constant’, the concentration at the position where the free-flight starts is needed, and this can bring some uncertainty. Nevertheless, the model of Pan and Hanratty is able to predict the increase in the particle radial-velocity fluctuation and the higher and more uniform deposition-constant. Our results indicate that the effects of the secondary flow on the deposition rate could be incorporated into a simple model within the framework already developed by Pan and Hanratty. However, the model of Pan and Hanratty does not take into account the influence of both the turbulence and the secondary flow on the fall-velocity of the particles, and a significant improvement would be to include these effects.

6. Conclusions and recommendations

6.1 Conclusions

In this thesis experimental and computational results are presented related to an annular-dispersed gas-liquid pipe-flow; both horizontal and vertical upward flows have been studied. The aim of the thesis is to study the interactions between the dispersed-phase and the gas-phase, and to see to what extent the dispersed-phase is responsible for the liquid-loading problem. The studied interactions involve the dispersed-phase pressure-gradient, the effect of secondary-flow on the deposition, and the effect of the dispersed-phase on the secondary flow.

Measurements of droplet size and droplet velocity in the core of a vertical upward annular-dispersed air-water pipe-flow using Phase Doppler Anemometry (PDA) have been performed. When decreasing the gas flow-rate below the gas Froude number $Fr_g \approx 1$ the flow regime has changed to churn-annular flow, and down-flow occurs. With churn-annular flow conditions all droplets still move upward, cocurrent with the gas flow, and thus it is implausible that the dispersed-phase is directly responsible for the occurrence of liquid loading, as is implicitly suggested by Turner et al. (1969).

Using the droplets in the size-range $10 \mu\text{m} < d_p < 20 \mu\text{m}$, the gas-phase mean velocity and velocity fluctuation profiles have been estimated. For an upward cocurrent annular flow these profiles are similar to those of a single-phase pipe-flow with an uniform wall-roughness. In contrast, in a churn-annular pipe-flow these profiles seem to be more uniform over the cross-section. For all flow conditions the gas-phase velocity-fluctuations scale roughly with the friction velocity.

Due to the continuous acceleration of the droplets in combination with a spread in their residence time, the droplets show a large spread in the axial velocity. Except for the smallest droplets ($d_p \lesssim 20 \mu\text{m}$), the resulting droplet velocity fluctuations are hardly depending on the gas-phase turbulence.

For both the churn-annular flows and the cocurrent annular flows the drop-size distribution has an exponential decreasing tail, and a fall-off at the smallest drop-sizes. Breakup and coalescence seem not to be dominant processes in the core of the flow for the flow conditions we measured, and thus the drop-size distributions are determined by the atomisation process. When breakup and coalescence is not occurring in the core of an annular flow, the mean droplet size is not expected to vary. This is observed both in the vertical and in the

horizontal flows.

For annular dispersed two-phase flows the droplets are continuously refreshed by the deposition-reentrainment process. Directly after the creation of a droplet, its axial velocity is much smaller than that of the mean gas flow, and consequently the droplet is accelerated strongly. In general, this acceleration is much larger than the axial component of the gravitational acceleration, and therefore, when focussing solely on the axial momentum for a given droplet, the pipe-inclination is not a relevant parameter, see chapters 2 to 4.

However, in the full picture the in-plane component of the gravity is responsible for the settling of the droplets towards the bottom of the pipe, and thus the inclination of the pipe does play a role. Also, the in-plane component of the gravity causes a circumferential variation of the film-thickness, and, most likely, therefore also a circumferential variation in the rate of atomisation.

From the above it can be concluded that, from the point of view of the dispersed-phase, the most interesting pipe orientations are vertical upward with minimum gravitational settling, and horizontal with maximum gravitational settling.

The axial acceleration of the droplets, created from the gas-liquid interface contributes to the total pressure-gradient, and it depends on the drop size. Both very small droplets ($d_p \lesssim 20 \mu\text{m}$) and very large droplets ($d_p \gtrsim 100 \mu\text{m}$) contribute little to the pressure gradient, since their effective acceleration in between atomisation and deposition, and their contribution to the holdup are close to zero, see chapters 2 and 3. The intermediate droplet size-range dominate the dispersed-phase pressure-gradient, and for these drop-sizes a good estimate for their contribution to the pressure-gradient is given with the model of Lopes and Dukler (1986) together with the assumption of Fore and Dukler (1995a), i.e. assuming that the arithmetic-mean droplet-velocity in the center of the pipe is roughly equal to the deposition-velocity of the droplets. Droplets are considered intermediate-sized when their relaxation time is larger than the time scale of the large-scale turbulence, but smaller than their residence time. Since in an actual annular flow, the intermediate-sized droplets make up for the largest part of the holdup, this assumption results in a good estimate of the dispersed-phase pressure-gradient.

A horizontal annular-dispersed pipe-flow has been simulated by a particle-laden gas-flow through a pipe with a circumferential variation of the wall-roughness, which generates a secondary flow (manifested as two counter-rotating vortical cells flowing up along the side-walls and down through the center of the pipe), see chapter 5. This secondary flow is able to bring droplets from the wall region to the core of the pipe. By increasing the overall droplet-concentration in the core and at the top of the pipe, the rate of deposition increases as well. Also, since the secondary flow and the gravitational settling of the droplets act in opposite direction, the effective settling is reduced along the wall. Since then also the relative importance of the gravitational settling with respect to the turbulence is reduced, the profile of the rate of deposition along the circumference is flattened.

When employing two-way coupling in the simulations, the dispersed-phase can modify the secondary flow when the loading is sufficiently large. Simulations are performed in which particles are injected with a low initial axial velocity from the bottom wall of the pipe into the turbulent gas-core, see chapter 4. With a dispersed-phase mass-loading above 0.2 a second

vortical cell-pair is created in the bottom region of the pipe, below the first vortical cell-pair, originating from the circumferential variation in wall-roughness. The second vortical cell-pair is driven by the blocking-effect of the dispersed-phase, and rotates in opposite direction with respect to the first one, i.e. flowing down along the side walls and up through the center of the pipe. The second vortical cell-pair is more effective in transporting the particles from the bottom region to the core region of the pipe, increasing the dispersed-phase concentration in the center of the pipe; it also reduces strongly the deposition constant in the bottom of the pipe.

By increasing the concentration in the core of the pipe, a secondary flow is expected to decrease the liquid film thickness. Also, since a secondary flow decreases the relative deposition constant at the bottom of the pipe, see chapters 4 and 5, it is thus expected that the secondary flow decreases the non-uniformity of the liquid film thickness as well. To what extent these effects are significant contributions depends on the ratio of the deposition flux and the drainage of the liquid film from the top to the bottom of the pipe along the circumference. When the inclination from the horizontal is increased, the flow becomes more axisymmetric and thus the secondary flow will decrease.

6.2 Recommendations

In order to simulate an actual annular dispersed pipe-flow as accurate as possible, we have introduced a poly-dispersion that is injected from the pipe wall into the gas flow. However the used injection-pdf is a fit to a measured droplet diameter and velocity pdf in the centerline of an annular-dispersed pipe-flow, and may not be an accurate representation of the atomisation-process. A next step may be to improve this injection-pdf, for which more accurate and detailed studies of the atomisation process are needed. A good approach would be to study a gas-liquid flow over a flat plate using a high-speed camera and 3D-PDA. In this way an accurate atomisation-pdf, describing the diameter, and the three velocity-components of the droplets, can be constructed that can be used as an input for the simulations.

Furthermore, in order to simulate a high Reynolds-number flow with moderate resources, i.e. making the computations not too cost-expensive or time-consuming, wall-functions are very usefull for the short term, i.e. prescribing the wall shear using a model (in our case the model is constructed using the mean velocity and a local roughness). Not only do they prevent the need for high resolution near the wall, they also can provide fairly good results in a straight-forward way when the pipe-wall is not smooth or even when the wall-roughness is non-constant. However, the biggest disadvantage of wall-functions is that the available models are applicable for some specific problems only, and they neglect the near-wall processes. Accurate dedicated measurements can help to finetune these models to include the effects of, e.g., particle-loading (see chapter 3) and non-constant wall-roughness (see chapter 5). (i.e., when keeping constant the mean velocity, how is the wall-shear at a given location affected by the presence of a dispersed-phase or by the change in wall-roughness at another location?).

It is also not yet clear to what extent the droplet deposition is a significant contribution to the liquid film-thickness. In order to shed more light on this topic, an estimate of the drainage of the liquid film from the top to the bottom of the pipe should be made. This in

turn can than be compared with the droplet deposition along the wall. In this way, by modifying the circumferential variation of the droplet deposition, the effect of the secondary-flow on the film-thickness distribution can be made more clear, and hence also its effect on the liquid-loading phenomenon.

A. Wall functions

In this appendix we validate the LES computations with wall-functions and verify the adequacy of the grid that we used. Also, we show that with a simple modification the Schumann wall-function for smooth walls can be used to simulate rough walls.

In order to validate the LES computations with wall-functions, a comparison is made with the experiments of Laufer (1954), Perry and Joubert (1963) and Zagarola and Smits (1998), for smooth walls. An averaging over the axial and tangential directions, and over multiple uncorrelated velocity fields (more than 100) was performed for simulations F_{sm} and F_{ro} . In fig. A.1, the average axial-velocity is plotted as a function of the distance to the wall, in wall-units. Figure A.2 shows the streamwise-velocity fluctuations and fig. A.3 the radial-velocity fluctuations. Some flow properties for the different LES computations and the experimental data from literature are given in table A.1.

	u_{sg} (m/s)	Re_{sg}	Re_{τ}	f
Laufer	2.4	38800	2060	0.0056
Perry	-	75000	-	-
Zagarola	8.4	56677	2860	0.0051
F_{sm}	19.60	65300	3300	0.0051
F_{ro}	19.21	64000	5274	0.0135

Table A.1: Results for the continuous-phase of the simulations F_{sm} and F_{ro} , and the experiments of Laufer (1954), Perry and Joubert (1963), Zagarola and Smits (1998) and Darling and McManus (1968). All the experiments used air and smooth walls.

Simulation F_{sm} agrees well with the mean axial-velocity profiles of Perry et al. and of Zagarola, but the measured data of Laufer are approximately 5% larger. For both F_{sm} and F_{ro} the logarithmic profile is nicely resolved and matches the law of the wall for a smooth and rough wall (dash-dotted). The axial-velocity fluctuations of F_{sm} and F_{ro} are in between the measurements of Laufer and Perry, but closer to the experiments of Laufer. Note that the maximum in the axial-velocity fluctuations is not resolved in our simulations, since the first grid point is located at $y^+ = 24$ for F_{sm} , and at $y^+ = 39$ for F_{ro} .

The radial turbulence-intensity in the center of the pipe, agrees well with the measurements of both Laufer, and Perry and Joubert. We can conclude that the radial turbulence intensity is resolved with wall-functions, showing minima near the wall and in the center, and a maximum at $y/D \approx 0.07$ ($y^+ \approx 300$).

When implementing the Schumann wall-function (eq. 5.4-5.8, see, e.g., Piomelli et al. (1989)),

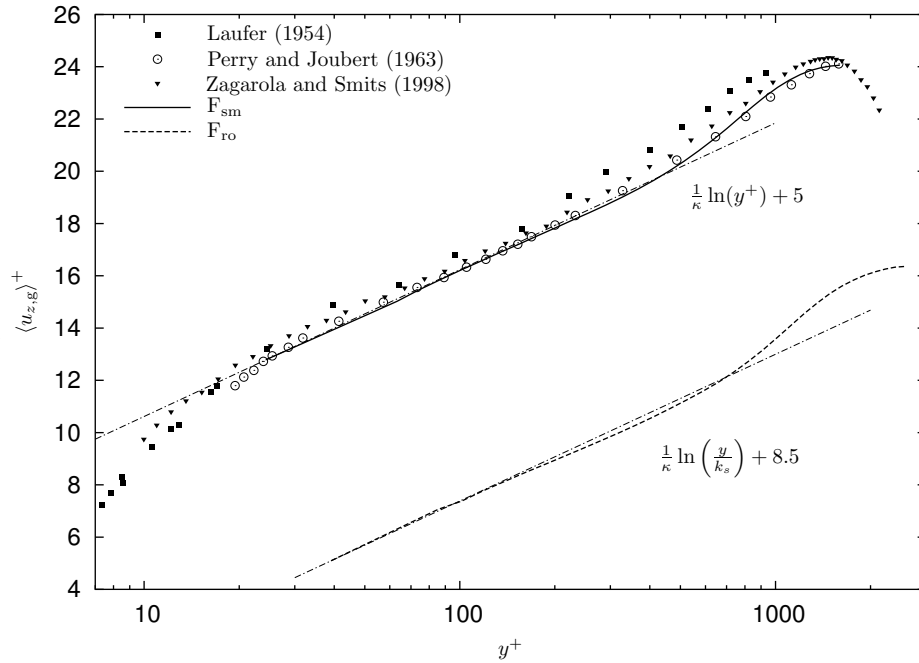


Figure A.1: Mean axial-velocity profile.

it is implicitly assumed that the instantaneous wall-shear-stress is proportional to the axial-velocity at the wall-nearest cell. Also, the near-wall turbulence structures (e.g. streaks) and events (e.g. bursts) are not resolved. Therefore, LES is not expected to give exact results for the two wall-nearest gridpoints for first-order statistics. Nevertheless, comparing the friction coefficient of F_{sm} with Blasius' relation, results in a mismatch of only 3.4%.

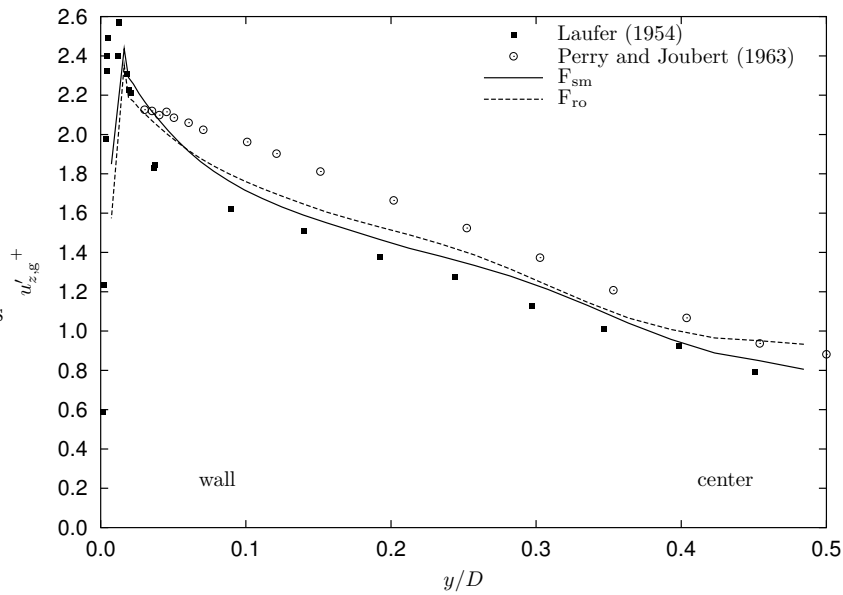


Figure A.2: Axial-velocity fluctuations of the experiments of Perry and Joubert (1963), Laufer (1954), and simulations F_{sm} and F_{ro} .

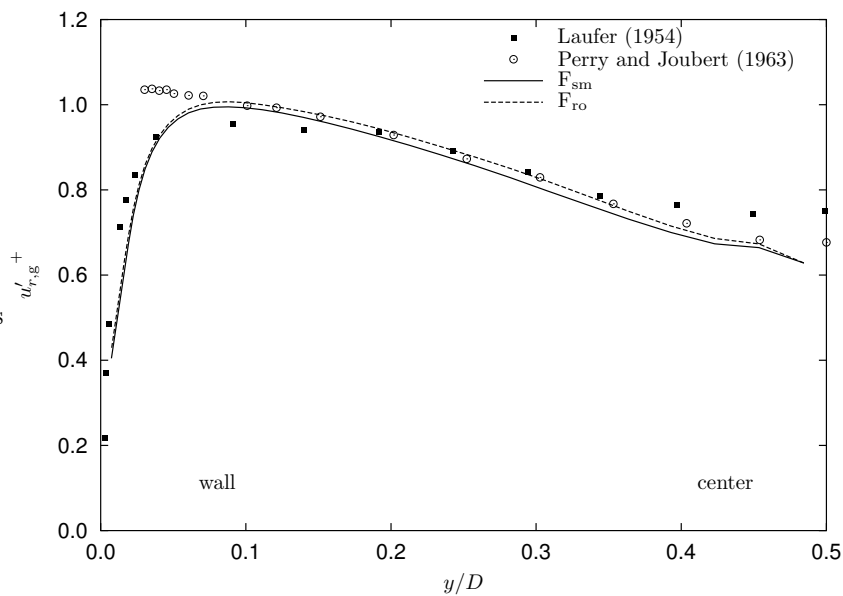


Figure A.3: Radial-velocity fluctuations of the experiments of Perry and Joubert (1963), Laufer (1954), and simulations F_{sm} and F_{ro} .

B. Injection PDF

In order to make the injection-pdf, we have visually fitted the joint-pdf of the drop size and the droplet lateral-velocity from an experiment in the center of a vertical upward air-water annular-dispersed pipe-flow, see Westende et al. (2007b). The superficial gas-velocity was $u_{sg} = 21$ m/s, the superficial liquid-velocity $u_{sl} = 2$ cm/s, and the pipe-diameter $D = 50$ mm. The injection-pdf is given as the product of two distributions: one for the drop size (PDF_d, eq. 3.26), and the other for the droplet lateral-velocity (PDF_u, eq. 3.27). In this way the particle size and its injection velocity are independent. This corresponds to an atomisation process in which ligaments are created from the gas-liquid interface with some initial lateral-velocity, and that these ligaments break up into smaller droplets with an equal initial lateral-velocity. In such a process, the initial lateral-velocity of a droplet probably depends on the size of the ligament from which it is created, and not so much on its own size. Here we note that for a droplet diameter larger than about 60 μm the measured mean lateral-velocity remains independent of the drop size and has a value of about 0.18 m/s.

In fig. B.1 we show the measured drop-size distribution, and in fig. B.2 we show the droplet lateral-velocity distribution (right graph), together with their fitted distributions, PDF_d and PDF_u, respectively.

Here we note that by using experimental centerline PDA-data to construct the injection-pdf, we have assumed that all particles have moved ballistically, hence this may not be directly linked to an atomisation process of a true annular flow. Also, with the experimental data only one component of the in-plane velocity is given, resulting in an overestimation of the low atomisation-velocities. The latter effect can result in a decrease of the mean injection velocity of about $1 - \frac{1}{\pi} \int_0^\pi \sin(\phi) d\phi = 0.35$, i.e. about 35%.

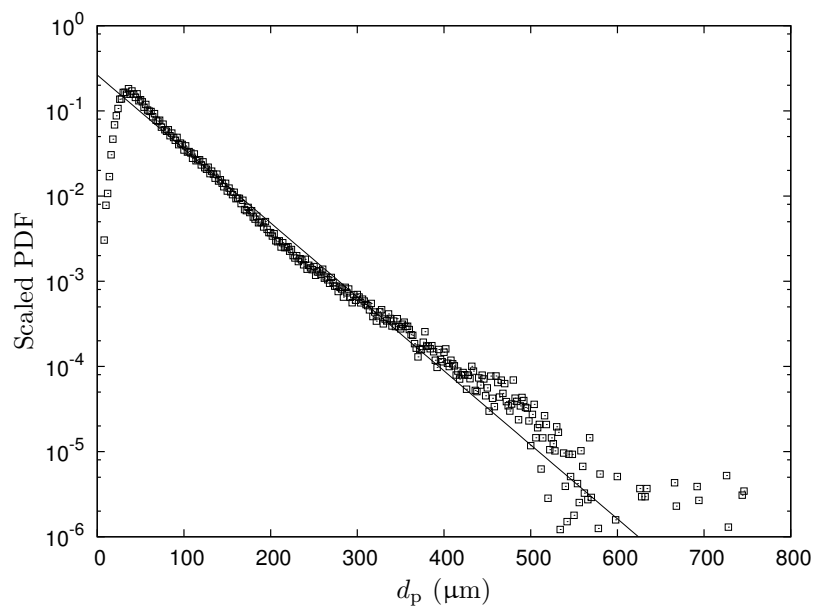


Figure B.1: Scaled drop size distribution. The symbols represent the results of the experiments and the solid lines are the fitted distributions.

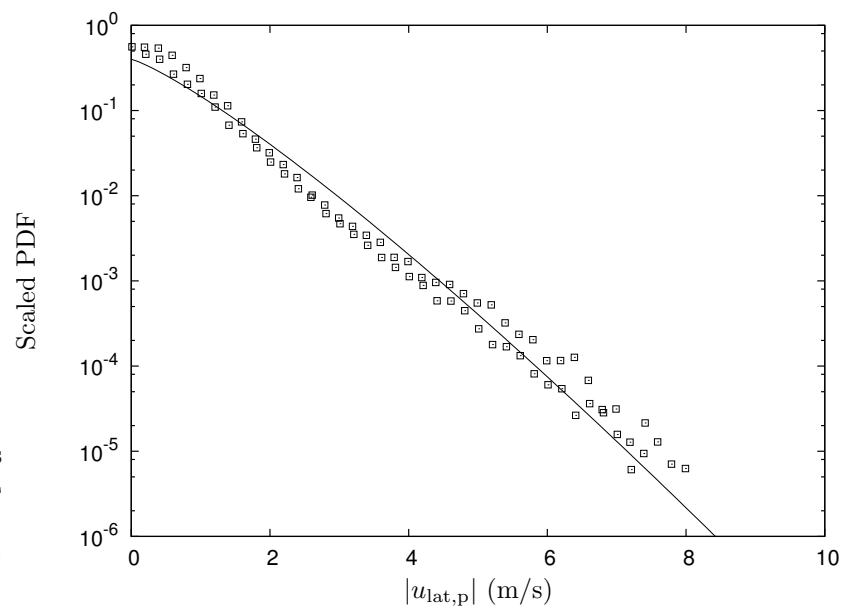


Figure B.2: Scaled lateral-velocity distribution. The symbols represent the results of the experiments and the solid lines are the fitted distributions.

Bibliography

- Al-Sarkhi, A. Hanratty, T.J., 2002. Effect of pipe diameter on the drop size in a horizontal annular gas-liquid flow. *Int. J. Multiphase Flow*, 28, 1617–1629.
- Albrecht, H.-E., Borys, M., Damaschke, N., Tropea, C., 2003. *Laser Doppler and Phase Doppler Measurement Techniques*. Springer-Verlag Berlin Heidelberg.
- Azzopardi, B. J., 1997. Drops in annular two-phase flow. *Int. J. Multiphase Flow*, 23, Suppl., 1–53.
- Azzopardi, B.J., 1979. Measurement of drop sizes. *Int. J. Heat Mass Transfer*, 22, 1245–1279.
- Azzopardi, B.J., 1999. Turbulence modification in annular gas/liquid flow. *Int. J. Multiphase Flow*, 25, 945–955.
- Azzopardi, B.J., Freeman, G., Whalley, P.B., 1978. Drop sizes in annular two-phase flow. ASME Winter Annual Meeting, Topics in Two-phase Flow and Heat Transfer, pages 165–173.
- Azzopardi, B.J. Hewitt, G.F., 1997. Maximum drop sizes in gas-liquid flows. *Multiph. Sci. Technol.*, 9, 109–204.
- Azzopardi, B.J., Pierarcey, A., Jepson, D.M., 1991. Drop size measurements for annular two-phase flow in a 20 mm diameter vertical tube. *Exp. Fluids*, 11, 191–197.
- Azzopardi, B.J. Teixeira, J.C.F., 1994. Detailed measurements of vertical annular two-phase flow - part i: Drop velocities and sizes. *J. Fluids Engng.*, 116, 792–795.
- Azzopardi, B.J. Whalley, P.B., 1980. Artificial waves in annular two-phase flow. ASME Winter Annual Meeting, Chicago, USA.
- Belt, R.J. On the liquid film in inclined annular flow. PhD thesis, Multi Scale Physics, Delft University of Technology, 2007.
- Belt, R.J., Westende, J.M.C. van 't, Portela, L.M., Mudde, R.F., Oliemans, R.V.A., 2004. Particle-driven secondary flow in turbulent horizontal pipe flow. 3rd Int. Symp. on Two-Phase Modelling and Exp., Pisa, Italy. ISBN 88-467-1075-4.
- Belt, R.J., Westende, J.M.C. van 't, Portela, L.M., Mudde, R.F., Oliemans, R.V.A., 2005. Direct numerical simulation of particle-driven secondary flow in turbulent horizontal pipe flows. 11th Workshop on Two-Phase Flow Predictions, Merseburg, Germany. ISBN 3-86010-767-4.
- Belt, R.J., Westende, J.M.C. van 't, Portela, L.M., Mudde, R.F., Prasser, H.M., Oliemans, R.V.A., 2007. Interfacial waves and shear-stress in vertical upward annular pipe flow. *Int. Conf. Multiphase Flow*, Leipzig, Germany.

- Bijlard, M.J., Portela, L.M., Oliemans, R.V.A., 2002. Effect of the particle-induced turbulence-modification on two-equation models for particle-laden wall-bounded turbulent flows. Rodi, W., Fueyo, N. (eds.) *Engineering Turbulence Modelling and Experiments* 5, pages 949–958.
- Boelens, A.M.P. Portela, L.M., 2006. Dns study of local-equilibrium models in dilute particle-laden turbulent pipe flow. *proceedings of Euromech Colloquium* 477.
- Burton, M. Eaton, J.K., 2005. Fully resolved simulations of particle-turbulence interaction. *J. Fluid Mech.*, 545, 67–111.
- Churchill, S.W., 1977. Friction factor equation spans all fluid flow regimes. *Chem. Eng.*, 84(24), 91–92.
- Cousins, L.B. Hewitt, G.F., 1968. Liquid phase mass transfer in annular two-phase flow: droplet deposition and liquid entrainment. UKAEA Report, AERE-R5657.
- Crowe, C.T., 2000. On models for turbulence modulation in fluid-particle flows. *Int. J. Multiphase Flow*, 26, 719–727.
- Csanady, G.T., 1963. Turbulent diffusion of heavy particles in the atmosphere. *J. Atmos. Sci.*, 20(3), 210–208.
- Daalmans, A.C.L.M., 2005. Laser-doppler anemometry measurements of particle-driven secondary flow in turbulent horizontal pipe flow. Master's thesis, Multi Scale Physics, Delft University of Technology.
- Dallman, J.C., Jones, B.G., Hanratty, T.J., 1979. Interpretation of entrainment measurements in annular gas-liquid flows. *Two-Phase Momentum, Heat and Mass Transfer*, 2, 681–693.
- Darling, R.S. McManus, H.N., 1968. Flow patterns in circular ducts with circumferential variation of roughness: a two-phase analog. *Dev. Mech.*, 5, 153–170.
- Davila, J. Hunt, J.C.R., 2001. Settling of small particles near vortices and in turbulence. *J. Fluid Mech.*, 440, 117–145.
- Durst, F. Zare, M., 1975. Laser-doppler measurements in two phase flows. *Proc. of the LDA Symp.*, pages 403–429, Copenhagen, Denmark.
- Dykhno, L.A., Williams, L.R., Hanratty, T.J., 1994. Maps of mean gas velocity for stratified flows with and without atomization. *Int. J. Multiphase Flow*, 20, 691–702.
- Eggels, J.G.M. Direct and large-eddy simulation of turbulent flow in a cylindrical pipe geometry. PhD thesis, Laboratory for Aero & Hydrodynamics, Delft University of Technology, 1994.
- Elghobashi, S., 1994. On predicting particle-laden turbulent flows. *Appl. Sci. Res.*, 52, 309–329.
- Elghobashi, S. Truesdell, G.C., 1993. On the two-way interaction between homogeneous turbulence and dispersed solid particles i: turbulence modification. *Phys. Fluids A*, 5(7), 1790–1801.
- Flores, A.G., Crowe, K.E., Griffith, P., 1995. Gas-phase secondary flow in horizontal, stratified and annular two-phase flow. *Int. J. Multiphase Flow*, 21(2), 207–221.
- Fore, L. B. Dukler, A. E., 1995a. Droplet deposition and momentum transfer in annular flow. *AICHE J.*, 41(9), 2040–2047.

- Fore, L.B. Dukler, A.E., 1995b. The distribution of drop size and velocity in gas-liquid annular flow. *Int. J. Multiphase Flow*, 21, 137–149.
- Fore, L.B., Ibrahim, B.B., Beus, S.G., 2002. Visual measurements of droplets size in gas-liquid annular flow. *Int. J. Multiphase Flow*, 28, 1895–1910.
- Friedlander, S.K. Johnstone, H.F., 1957. Deposition of suspended particles from turbulent gas streams. *Ind. Eng. Chem.*, 49(7), 1151–1156.
- Gibbons, D.B., Azzopardi, B.J., Bott, T.R., 1983. Laser tomography investigation of the entrained liquid in annular two-phase flow. *Int. Conf. Physical Modelling of Multiphase Flow*, pages 327–336.
- Gibbons, D.B., Azzopardi, B.J., Bott, T.R., 1985. Determination of the rate of entrainment in annular two-phase flow. *2nd Int. Conf. on Multiphase Flow*, London, UK.
- Gore, R.A. Crowe, C.T., 1989. Effect of particle size on modulating turbulent intensity. *Int. J. Multiphase Flow*, 15(2), 279–285.
- Govan, A.H., 1989. A simple equation for the diffusion coefficient of large particles in a turbulent gas flow. *Int. J. Multiphase Flow*, 15(2), 287–294.
- Hay, K. J., Liu, Z. C., Hanratty, T. J., 1996. Relation of deposition to drop size when the rate law is nonlinear. *Int. J. Multiphase Flow*, 22(5), 829–848.
- Hay, K.J., Liu, Z.-C., Hanratty, T.J., 1998. A backlighting technique for particle size measurements in two-phase flows. *Exp. Fluids*, 25, 226–232.
- Hetsroni, G., 1989. Particles-turbulence interaction. *Int. J. Multiphase Flow*, 15, 735–746.
- Hewitt, G.F. Whalley, P.B., 1980. Advanced optical instrumentation methods. *Int. J. Multiphase Flow*, 6, 139–156.
- Hinze, J.O., 1955. Fundamentals of the hydrodynamic mechanism of splitting in dispersion processes. *AIChE J.*, 1(3), 289–295.
- Huber, N. Sommerfeld, M., 1998. Modelling and numerical calculation of dilute-phase pneumatic conveying in pipe systems. *Powder Tech.*, 99, 90–101.
- Hurlburt, E.T. Hanratty, T.J., 2002. Measurement of drop size in horizontal annular flow with the immersion method. *Exp. Fluids*, 32, 692–699.
- Jayanti, S. Hewitt, G.F., 1996. Response of turbulent flow to abrupt changes in surface roughness and its relevance in horizontal annular flow. *Appl. Math. Model.*, 20, 244–251.
- Jayanti, S., Wilkes, S., Clarke, N.S., Hewitt, G.F., 1990. The prediction of turbulent flows over roughened surfaces and its application to interpretation of mechanism of horizontal annular flow. *Proc. R. Soc. Lond. A*, 431, 71–88.
- Jepson, D.M., Azzopardi, B.J., Whalley, P.B., 1989. The effect of gas properties on drops in annular flow. *Int. J. Multiphase Flow*, 15, 327–339.
- Jimenez, J., 2003. Computing high-reynolds-number turbulence: will simulations ever replace experiments? *J. Turbulence*, 4(22), 1–14.
- Jimenez, J., 2004. Turbulent flows over rough walls. *Ann. Rev. Fluid Mech.*, 36, 173–196.

- Kemp, H.K., 2004. Droplet size and velocity measurements in annular flow using phase-doppler anemometry. Master's thesis, Multi Scale Physics, Delft University of Technology.
- Kocamustafaogullari, G., Smits, S.R., Razi, J., 1994. Maximum and mean droplet sizes in annular two-phase flow. *Int. J. Heat Mass Transfer*, 37, 955–965.
- Laufer, J., 1954. The structure of turbulence in fully developed pipe flow. NACA Rep. 1174, pages 417–434.
- Lee, M.M., Hanratty, T.J., Adrian, R.J., 1989. The interpretation of droplet deposition measurements with a diffusion model. *Int. J. Multiphase Flow*, 15(3), 459–469.
- Li, Y., McLaughlin, J.B., Kontomaris, K., Portela, L., 2001. Numerical simulation of particle-laden turbulent channel flow. *Phys. Fluids*, 13, 2957–2967.
- Lin, T.F., Jones, O.C., Lahey, R.T., Block, R.T., Murase, M., 1985. Film thickness distribution for gas-liquid annular flow in a horizontal pipe. *Physicochem. Hydrodyn.*, 6, 179–195.
- Lopes, J. C. B. Dukler, A. E., 1986. Droplet entrainment in vertical annular flow and its contribution to momentum transfer. *AIChE J.*, 32(9), 1500–1515.
- Bertodano, M.A. Lopez de, Assad, A., Beus, S.G., 2001. Experiments for entrainment rate of droplets in the annular regime. *Int. J. Multiphase Flow*, 27, 685–699.
- Marchioli, C., Giusti, A., Salvetti, M.V., Soldati, A., 2003. Direct numerical simulation of particle wall transfer and deposition in upward turbulent pipe flow. *Int. J. Multiphase Flow*, 29, 1017–1038.
- Marchioli, C., Picciotto, M., Soldati, A., 2007. Influence of gravity and lift on particle velocity statistics and transfer rates in turbulent vertical channel flow. *Int. J. Multiphase Flow*, 33, 227–251.
- Marmottant, P. Villermaux, E., 2004. On spray formation. *J. Fluid Mech.*, 498, 73–111.
- McLaughlin, J.B., 1989. Aerosol particle deposition in numerically simulated channel flow. *Phys. Fluids A*, 1(7), 1211–1224.
- Mito, Y. Hanratty, T.J., 2006. Effect of feedback and inter-particle collisions in an idealized gas-liquid annular flow. *Int. J. Multiphase Flow*, 32, 692–716.
- Mols, B. Particle dispersion and deposition in horizontal turbulent channel and tube flows. PhD thesis, Laboratory for Aero & Hydrodynamics, Delft University of Technology, 1999.
- Mugele, R.A. Evans, H.D., 1951. Droplet size distribution in sprays. *Ind. Eng. Chem.*, 43(6), 1317–1324.
- Okada, O., Fujimatsu, T., Fujita, H., Nakjima, Y., 1995. Measurement of droplet size distribution in an annular mist flow in a vertical pipe by immersion liquid method. *Proc. 2nd Int. Conf. on Multiphase Flow*, volume 1, pages IP2/11–IP2/18, Kyoto, Japan.
- Oki, K., Akehata, T., Shirai, T., 1975. A new method for evaluating the size of moving particles with a fibre optic probe. *Powder Tech.*, 11, 51.
- Oudeman, P., 1989. Improved prediction of wet-gas-well performance (spe 19103). SPE Gas Technology Symposium, Dallas, USA.

- Pan, L. Hanratty, T.J., 2002. Correlation of entrainment for annular flow in horizontal pipes. *Int. J. Multiphase Flow*, 28, 385–408.
- Pan, Y. Banerjee, S., 1996. Numerical simulation of particle interactions with wall turbulence. *Phys. Fluids*, 8 (10), 2733–2755.
- Pan, Y. Banerjee, S., 1997. Numerical investigation of the effects of large particles on wall-turbulence. *Phys. Fluids*, 9(12), 3786–3807.
- Peng, C.-A., Jurman, L.A., McCreedy, M.J., 1991. Formation of solitary waves on gas-sheared liquid layers. *Int. J. Multiphase Flow*, 17(6), 767–782.
- Perry, A.E. Joubert, P.N., 1963. Rough-wall boundary layers in adverse pressure gradients. *J. Fluid Mech.*, 17, 193–211.
- Piomelli, U., Ferziger, J., Moin, P., Kim, J., 1989. New approximate boundary conditions for large eddy simulations of wall-bounded flows. *Phys. Fluids A*, 1(6), 1061–1068.
- Pogson, J.T., Roberts, J.H., Waibler, P.J., 1970. Influence of hydrodynamic interactions between particles on the turbulent flow in a suspension. *J. Heat Transfer*, 92, 651–658.
- Portela, L.M., Cota, P., Oliemans, R.V.A., 2002. Numerical study of the near wall behaviour of particles in turbulent pipe flows. *Powder Tech.*, 125, 149–157.
- Portela, L.M. Oliemans, R.V.A., 2001. Direct and large-eddy simulation of particle-laden flows using the point-particle approach. *Direct and Large-Eddy Simulation IV*, pages 453–460, Enschede, Holland.
- Portela, L.M. Oliemans, R.V.A., 2002. Subgrid particle-fluid coupling evaluation in large-eddy simulations of particle-laden flows. *Proc. ASME IMECE*.
- Portela, L.M. Oliemans, R.V.A., 2003. Eulerian-lagrangian dns/les of particle-turbulence interactions in wall-bounded flows. *Int. J. Numer. Meth. Fluids*, 43, 1045–1065.
- Portela, L.M. Oliemans, R.V.A., 2006. Possibilities and limitations of computer simulations of industrial turbulent dispersed multiphase flows. *Flow Turbulence Combust*, 77, 381–403.
- Quandt, E.R., 1965. Measurements of some basic parameters in two-phase annular flow. *AIChE J.*, 11, 311–318.
- Rani, S.L., Winkler, C.M., Vanka, S.P., 2004. Numerical simulations of turbulence modulation by dense particles in a fully developed pipe flow. *Powder Tech.*, 141, 80–99.
- Ribeiro, A.M., Bott, T.R., Jepson, D.M., 1995. Drop size and entrainment measurements in horizontal flow. *Int. Conf. on Two-phase Flow Modelling and Experimentation*, Rome, Italy.
- Ritter, R.C., Zinner, N.R., Sterling, A.M., 1974. Analysis of drop intervals in jets modelling obstructions of the urinary tract. *Phys. Med. Biol.*, 19, 161.
- Rouson, D.W.I. Eaton, J.K., 2001. On the preferential concentration of solid particles in turbulent channel flow. *J. Fluid Mech.*, 428, 149–169.
- Russell, T.W.F. Lamb, D.E., 1974. Flow mechanism of two-phase annular flow. *Can. J. Chem. Engng.*, 43, 237–245.

- Schadel, S. A., Leman, G. W., Binder, J. L., Hanratty, T. J., 1990. Rates of atomization and deposition in vertical annular flow. *Int. J. Multiphase Flow*, 16(3), 363–374.
- Schlichting, H., 1979. *Boundary-layer theory*. McGraw-Hill series in mech. eng., 7th ed.
- Segura, J.C. Predictive capabilities of particle-laden large eddy simulation. PhD thesis, TSD-156, Stanford University, CA, 2004.
- Segoguchi, K. Takeishi, M., 1989. Interfacial structures in upward huge wave flow and annular flow regimes. *Int. J. Multiphase Flow*, 15(3), 295–305.
- Semiat, R. Dukler, A.E., 1981. Simultaneous measurement of size and velocity of bubbles or drops: a new optical technique. *AIChE J.*, 27(1), 148–159.
- Simmons, M. J. H. Hanratty, T. J., 2001. Droplet size measurements in horizontal annular gas-liquid flow. *Int. J. Multiphase Flow*, 27, 861–883.
- Simmons, M. J. H., Ziadi, S. H., Azzopardi, B. J., 2000. Comparison on laser-based drop-size measurement techniques and their application to dispersed liquid-liquid pipe flow. *Opt. Eng.*, 39(2), 505–509.
- Sommerfeld, M., 1992. Modelling of particle-wall collisions in confined gas-particle flows. *Int. J. Multiphase Flow*, 18, 905–926.
- Sommerfeld, M., 2001. Validation of a stochastic lagrangian modelling approach for inter-particle collisions in homogeneous isotropic turbulence. *Int. J. Multiphase Flow*, 27, 1829–1858.
- Speziale, C.G., 1982. On turbulent secondary flows in pipes of non-circular cross-section. *Int. J. Eng. Sci.*, 20, 863–872.
- Squires, K.D. Eaton, J.K., 1990. Particle response and turbulence modification in isotropic turbulence. *Phys. Fluids A*, 2(7), 1191–1203.
- Squires, K.D. Eaton, J.K., 1991. Preferential concentration of particles by turbulence. *Phys. Fluids A*, 3, 1169–1178.
- Swithenbank, J., Beer, J.M., Taylor, D.S., Abbot, D., McCreath, G.C., 1976. A laser diagnostic for the measurement of droplet and particle size distributions. *Prog. Astronaut. Aeronaut.*, 1, 421–447.
- Taitel, Y., 1977. Flow patterns transition in rough pipes. *Int. J. Multiphase Flow*, 3, 597–601.
- Taitel, Y., Barnea, D., Dukler, A.E., 1980. Modelling flow pattern transitions for steady upward gas-liquid flow in vertical tubes. *AIChE J.*, 26(3), 345–354.
- Tayali, N.E. Bates, C.J., 1990. Particle sizing techniques in multiphase flows: a review. *Flow Meas. Instrum.*, 1, 77–105.
- Tayali, N.E., Bates, C.J., Yeoman, M.L., 1990. Drop size and velocity measurements in vertical developing annular two-phase flow. *Proc. 3rd Int. Conf. on Laser Anemometry Advances and Applications*, pages 431–440, Berlin, Germany.
- Teixeira, J.C.F., Azzopardi, B.J., Bott, T.R., 1988. The effects of inserts on drop size in vertical annular flow. *2nd UK National Heat Transfer Conf.*, Strathclyde, UK.

- Thoroddsen, S. Takehara, K., 2000. The coalescence cascade of a drop. *Phys. Fluids*, 12, 1265–1267.
- Truesdell, G.C. Elghobashi, S., 1994. On the two-way interaction between homogeneous turbulence and dispersed solid particles ii: particle dispersion. *Phys. Fluids*, 6(3), 1405–1407.
- Turner, R.G., Hubbard, M.G., Dukler, A.E., 1969. Analysis and prediction of minimum flow rate for the continuous removal of liquid from gas wells. *Journal of Petroleum Technology*, pages 1475–1482.
- Ueda, T., 1979. Entrainment rate and size of entrained droplets in annular two-phase flow. *Bull. JSME*, 22, 1258–1265.
- Uijtewaal, W.S.J. Oliemans, R.V.A., 1996. Particle dispersion and deposition in direct numerical and large eddy simulations of vertical pipe flows. *Phys. Fluids*, 8, 2590–2604.
- Wallis, G.B., 1969. *One Dimensional Two-Phase Flow*. McGraw-Hill.
- Westende, J.M.C. van 't, Belt, R.J., Portela, L.M., Mudde, R.F., Oliemans, R.V.A., 2004. Interaction of particles with secondary flow in high reynolds number horizontal pipe flow. 3rd Int. Symp. on Two-Phase Modelling and Exp., Pisa, Italy. ISBN 88-467-1075-4.
- Westende, J.M.C. van 't, Belt, R.J., Portela, L.M., Mudde, R.F., Oliemans, R.V.A., 2005. Droplet characterisation in upward annular dispersed pipe flow. 11th Workshop on Two-Phase Flow Predictions, Merseburg, Germany. ISBN 3-86010-767-4.
- Westende, J.M.C. van 't, Belt, R.J., Portela, L.M., Mudde, R.F., Oliemans, R.V.A., 2007a. Effect of secondary flow on droplet distribution and deposition in horizontal annular pipe flow. *Int. J. Multiphase Flow*, 33, 67–85.
- Westende, J.M.C. van 't, Belt, R.J., Portela, L.M., Mudde, R.F., Oliemans, R.V.A., 2008. A numerical study of the pressure-gradient in a poly-dispersed high reynolds number flow with a large mass loading. to be published in *AICHE J*.
- Westende, J.M.C. van 't, Kemp, H.K., Belt, R.J., Portela, L.M., Mudde, R.F., Oliemans, R.V.A., 2007b. On the role of droplets in cocurrent annular and churn-annular pipe flow. *Int. J. Multiphase Flow*, 33, 595–615.
- Whalley, P.B., Azzopardi, B.J., Pshyk, L., Hewitt, G.F., 1977. Axial view photograph of waves in annular two-phase flow. UKAEA Report, AERE-R8787.
- Wigley, G., 1977. The sizing of large droplets by laser anemometry. UKAEA Report, AERE-R8771.
- Wilkes, N.S., Azzopardi, B.J., Thompson, C.P., 1983. Wave coalescence and entrainment in vertical annular two-phase flow. *Int. J. Multiphase Flow*, 9, 383–398.
- Williams, L.R., Dykhno, L.A., Hanratty, T.J., 1996. Droplet flux contributions and entrainment in horizontal gas-liquid flows. *Int. J. Multiphase Flow*, 22(1), 1–18.
- Yamamoto, Y., Potthoff, M., Tanaka, T., Kajishima, T., Tsuji, Y., 2001. Large-eddy simulation of turbulent gas-particle flow in a vertical channel: effect of considering inter-particle collisions. *J. Fluid Mech.*, 442, 303–334.
- Young, J. Leeming, A., 1997. A theory of particle deposition in turbulent pipe flow. *J. Fluid Mech.*, 340, 129–159.

-
- Zabaras, G., Dukler, A. E., Moalem-Maron, D., 1986. Vertical upward cocurrent gas-liquid annular flow. *AIChE J.*, 32(5), 829–743.
- Zagarola, M.V. Smits, A.J., 1998. Mean-flow scaling of turbulent pipe flow. *J. Fluid Mech.*, 373, 33–79.
- Zaidi, S. H., Altunbas, A., Azzopardi, B. J., 1998. A comparative study of phase doppler and laser diffraction techniques to investigate drop sizes in annular two-phase flow. *Chem. Eng. J.*, 71, 135–143.
- Zhang, Zh. Ziada, S., 2000. Pda measurements of droplet size and mass flux in the three-dimensional atomisation region of water jet in air cross-flow. *Exp. Fluids*, 28, 29–35.

Acknowledgement

Een promotie doe je niet alleen. Ik ben dan ook dankbaar dat veel mensen mij gesteund hebben bij het bereiken van dit resultaat.

Ten eerste wil ik Rene Oliemans en Rob Mudde bedanken voor de grote vrijheid die ze mij gegeven hebben om dit onderzoek te verrichten.

Luis, I enjoyed very much the numerous discussions we had related to the processes that occur in the flow. You really were a great help, and always had an open door for me. Besides a devoted supervisor, I gained a good friend in you. Hopefully our paths will keep crossing.

Verder wil ik de leden van de STW gebruikerscommissie bedanken voor de tijd die zij in dit project gestopt hebben, en voor hun bijdragen tijdens de voortgangspresentaties.

De experimentele opstelling waar ik veel tijd mee heb doorgebracht: het Grote Rode Frame, die eindeloos is aangepast aan mijn wensen, heeft alleen tot stand kunnen komen dankzij JaapvR, JaapK, JaapB, Jan, Ab en Wouter. Bedankt voor jullie inzet, kundigheid en goede ideeën. Ook het afstudeerproject van Hille heeft mij erg geholpen om kennis van en vertrouwen in de PDA te krijgen.

In de vijf jaren die ik op het Lab heb doorgebracht heb ik veel kamergenoten versleten: W140: Joost, Valerie; W250: Eelco, Maarten, Christoph, Ziad, Michael, Axel, Oscar, Andrea; W220: Wouter, Hugo, Marco, Annekatrien, Ozgur, Maria (MAOM: the goodbye party still touches me), and W020: Roel. Ik heb in alle kamers een gezellige tijd gehad, en aan iedereen goede herinneringen. Especially, I enjoyed the LAN-games on the lab with Usama, Anton, Jose, Robin, Sam, and Roel: there is nothing better than virtually slaughtering your PhD-colleagues.

Van alle PhD-collega's springen er drie in het bijzonder uit: Maarten: voor vragen omtrent turbulentie kon ik altijd bij jou terecht; Roel: wellicht heeft het 'wandklimmen' in onze gezamenlijke experimentele opstelling ons de nodige helicopter-view gegeven; en Wouter: je bent nooit te oud voor een Xbox.

Daarnaast wil ik mijn ouders, familie en vrienden bedanken voor hun continue steun. Jullie boden altijd een luisterend oor op de momenten waarop ik het nodig had.

Tot slot ben ik nog wel de meeste dank verschuldigd aan mijn vrouw, Sandra. Ongeveer vijf jaar lang heb jij echt alle details aangehoord van mijn onderzoek, en bleef je geïnteresseerd.

De meest cruciale momenten hebben wij samen beleefd, en ik ben blij dat je al deze tijd zoveel geduld met mij hebt gehad.

List of publications

Belt, R.J., van 't Westende, J.M.C., Portela, L.M., Mudde, R.F., Oliemans, R.V.A., 2004. Particle-driven secondary flow in turbulent horizontal pipe flow. 3rd Int. Symp. on Two-Phase Modelling and Exp., Pisa, Italy. ISBN 88-467-1075-4.

Westende, J.M.C. van 't, Belt, R.J., Portela, L.M., Mudde, R.F., Oliemans, R.V.A., 2004. Interaction of particles with secondary flow in high Reynolds number horizontal pipe flow. 3rd Int. Symp. on Two-Phase Modelling and Exp., Pisa, Italy. ISBN 88-467-1075-4.

Belt, R.J., van 't Westende, J.M.C., Portela, L.M., Mudde, R.F., Oliemans, R.V.A., 2005. Direct numerical simulation of particle-driven secondary flow in turbulent horizontal pipe flows. 11th Workshop on Two-Phase Flow Predictions, Merseburg, Germany. ISBN 3-86010-767-4.

Westende, J.M.C. van 't, Belt, R.J., Portela, L.M., Mudde, R.F., Oliemans, R.V.A., 2005. Droplet characterisation in upward annular dispersed pipe flow. 11th Workshop on Two-Phase Flow Predictions, Merseburg, Germany. ISBN 3-86010-767-4.

Westende, J.M.C. van 't, Belt, R.J., Portela, L.M., Mudde, R.F., Oliemans, R.V.A., 2007a. Effect of secondary flow on droplet distribution and deposition in horizontal annular pipe flow. *Int. J. Multiphase Flow*, 33, 67-85.

Westende, J.M.C. van 't, Belt, R.J., Portela, L.M., Mudde, R.F., Oliemans, R.V.A., 2007b. On the role of droplets in cocurrent annular and churn-annular pipe flow. *Int. J. Multiphase Flow*, 33, 595-615.

Belt, R.J., van 't Westende, J.M.C., Portela, L.M., Mudde, R.F., Prasser, H.M., Oliemans, R.V.A., 2007. Interfacial waves and shear-stress in vertical upward annular pipe flow. *Int. Conf. Multiphase Flow*, Leipzig, Germany. Papernumber S5_Thu_B.51.

About the author

Jozef Marinus Cyril van 't Westende is 29 november 1976 geboren te Fijnaart en Heijningen, Nederland. In 1995 behaalde hij zijn VWO-diploma aan het Norbertus College te Roosendaal. Hierna is hij de studie Technische Natuurkunde begonnen aan de Technische Universiteit Delft. In 2001 studeerde hij af bij de vakgroep Nanofysica, faculteit Technische Natuurwetenschappen. Vanaf 2002 is hij een promotie onderzoek begonnen bij het Kramers Laboratorium voor Fysische Technologie, Technische Universiteit Delft.

Sinds maart 2007 is hij werkzaam als onderzoeker/adviseur bij de groep Industrial Flow Technology, van WL|Delft Hydraulics.